Department of Mechanical Engineering
University of Wisconsin--Milwaukee
Milwaukee, Wisconsin 53201

NAG3-546

IMPROVEMENT OF THE SECOND- AND THIRD-MOMENT MODELING OF TURBULENCE

January 1986

by

R. S. Amano
Principal Investigator

and

P. Goel
Research Assistant

Semi-Annual Progress Report on

"A STUDY OF REYNOLDS-STRESS CLOSURE MODEL"

The report documents research completed during the period of July 15 through January 15, 1986 under NASA-Lewis Research Grant No. NAG 3-546.

TF/86/1

94E/2623E

ABSTRACT

This report contains four parts of the Reynolds-stress closure modeling: 1) improvement of the k and ϵ equations, 2) development of the third-moment transport equation, 3) formulation of the diffusion coefficient of the momentum equation by using the algebraic-stress model of turbulence, and 4) the application of the Reynolds-stress model to a heat exchanger problem. It has been demonstrated that the third-moment transport model improved the prediction of the triple-velocity products in the recirculating and reattaching flow regions in comparison with the existing algebraic models for the triple-velocity products. Then, optimum values for empirical coefficients are obtained for the prediction of the backward-facing step flows. Furthermore, a functional expression is derived for the coefficient of the momentum diffusion by employing the algebraic-stress model. Finally, the second-moment closure is applied to a heat transfer problem. The computations for the flow in a corrugated-wall channel show that the second-moment closure improves the prediction of the heat transfer rates by 30% over the $k - \epsilon$ model. In this way, the application of the Reynolds stress model to heat transfer problems is demonstrated to be promising.

PREFACE

This report outlines the progress of the research conducted from July 1985 to January 1986. During this period, the third-moment closure model was studied as well as refining the second-moment closure. The development of transport equations for the third-moments of turbulence velocity fluctuation has been pursued since it was observed, in the last research project period, that none of the existing algebraic third-moment models can predict the levels of the triple velocity products correctly for the backward-facing step flows. The predictions by the algebraic models were particularly poor in the recirculating flow regions.

In this report it is shown that the currently developed transport equations of the third-moments improve the prediction of the triple-velocity products of turbulence fluctuations in comparison with the algebraic third-moment models.

In carrying out this project the authors are grateful for the assistance of Messrs. A. Bagherlee, R. Smith, T. Hiess, and V. Kodali who performed a large amount of programming and computations.

TABLE OF CONTENTS

NOMENCLATURE

a	channel step height
a_{ij}	anisotropy
b	channel width
$C_1, C_2, C_p, C_k, C_p, C_p, C_{w1}, C_{w2}, C_\varepsilon, C_{\varepsilon 1}, C_{\varepsilon 2}, C_{\phi 1}, C_{\phi 2}, C_{\phi 3}$	constants used in turbulence model
C_{ij}	coefficients for near-wall Reynolds stresses
D	diameter of the disk
D_{ij}	diffusion rate of the Reynolds stresses
D_T	diameter of the tube
f	average skin friction factor
f_w	function for wall correction
G	generation rate of turbulence kinetic energy, k
G_{ij}	generation rate of Reynolds stresses
h	local heat transfer coefficient
H	step height
H_{ij}	secondary generation rate of Reynolds stresses
k	turbulence kinetic energy ($=\overline{u_i^2}$)
L_{fin}	length of fin
Nu	Nusselt number based on 2b
$\overline{Nu}$	averaged Nusselt number
p	pressure fluctuation
P	mean pressure
$\dot{q}_w$	wall heat flux
r	radial coordinate

Re	Reynolds number based on 2b
T	temperature
T_b	bulk temperature
T_w	wall temperature
u	fluctuating velocity in x direction
U	mean velocity
U_{IN}	inlet stream velocity
U_m	averaged mean velocity
v	fluctuating velocity in y or r direction
V	mean velocity in y or r direction
w	fluctuating velocity in z or θ direction
x, y, z	Cartesian coordinates
y^+	dimensionless distance from wall to the first numerical node-point, ($= k^{1/2}y/\nu$)
a_1, a_2, a_3, a_4	constants used in Eq. (19)
Γ	thermal diffusivity
δ_{ij}	Kronecker delta
ε	energy dissipation rate
θ	coordinate in azimuth direction
μ	dynamic viscosity
ν	kinematic viscosity
ρ	density
σ	Prandtl number
Φ_{ij}	pressure-strain correlation

Subscripts

i, j, k, ℓ, m	tensor notations

1. INTRODUCTION

In computations of turbulent separated shear flows, it has become more common to use the second-order closure of turbulence. While modern computational techniques enable us to successfully predict most of the simple turbulent shear flows, it is still difficult to accurately predict the separated and reattaching shear flow particularly when it is accompanied by a flow recirculation. This is partly because the computation should be performed with an elliptic approach which requires large amounts of computer time and storage, and partly because a turbulence model that can predict such complex turbulent flows (including flow reattachment, flow recirculation and a recovering boundary layer) has not yet been completely developed for universal usage.

A large number of experimental studies on this subject have been reported in the last two decades. The Reynolds stresses in the reattachment zone were obtained by Etheridge and Kemp[1], Kim et al.[2], Smyth[3], Eaton and Johnston[4], etc. Commonly it has been shown that the turbulence energy level reaches a peak value approximately one step height upstream of the reattachment point, then decays rapidly in the streamwise direction toward the wall, although it decays relatively slowly along the wall in the wall vicinity region. This feature is in contrast with free shear flows which are not constrained by the solid wall. It is also noted that the recirculating zone affects the reattaching shear layer resulting in higher turbulence energy levels near the reattachment zone.

Although the measurements of nigher-order turbulence moments are scarce in literature, a few third-moment data are available. The triple-velocity products were measured by Chandrsuda and Bradshaw[5] by using a hot-wire

anemometer for a channel with a larger channel width of 3.5 step heights. Driver and Seegmiller[6] used a channel with a width of 9 step heights wherein the boundary layer thickness just above the step was about 1.5 step heights having an inviscid core region outside the separating layer. They measured the secondand third-moments of turbulence velocity fluctuations with a two-component LDV by varying the pressure gradient in the inviscid core region.

Through this NASA project, the authors have investigated the features of the second- and third-moments in the reattaching and recirculating flow regions. First, the existing model of the Reynolds-stress transport equations was modified and adjusted for the elliptic flows.[7] The computations were made for several different cases of flow and geometry, and the results were compared with the $k - \varepsilon$ model and the algebraic-stress model of Rodi.[8] Although the model used by Amano and Goel[7] was the hybrid model of the Boussinesq viscosity and the Reynolds-stress equations, the prediction of the normal and shear stresses was improved in the reattaching and the recovering region behind a step.

Meanwhile, it was observed that the triple-velocity products decay rapidly in the reattaching region which creates steep changes in the diffusion rates of the Reynolds stresses. In the last two reports,[9-10] most of the existing third-moment models were tested to determine whether they could be employed for the prediction of such reattaching shear layers or not. As a result, it was recommended that a transport model for the third-moment should be evolved since none of the algebraic models for the third-moments gives sufficiently high levels in a complex turbulent flow although the models are satisfactory for parabolic thin shear flows.

In this report, the work performed is summarized in the following steps:

1. Incorporation of the non-isotropic treatment for the diffusion rates of the k and ϵ equations.
2. Determination of the empirical coefficients of the above mentioned diffusion rates.
3. Development of the transport equations for the third-moments of turbulence.
4. Testing the third-moment model for the reattaching shear flows in order to determine the coefficients which appear in the third-moment transport equations.
5. Formulation of the correlation function used in the diffusion rates of the momentum equations.
6. Application of the second-moment closure to a heat transfer problem.

In the above procedure, step 5 was achieved by using the algebraic-stress model because of its simple formulation of the Reynolds stresses. In order to eliminate the complexity due to the wall flows, this test was limited to only wakes which were created behind steps. In step 6, a periodically corrugated wall channel was considered. This is the basic study of a compact heat exchanger.

2. THE SECOND-MOMENT CLOSURE MODEL

2.1 Preliminary Remarks

Both the turbulence energy, k, and the energy dissipation rate, ε, are always used to define the time scale, k/ε, and the length scale, $k^{3/2}/\varepsilon$. Therefore, if the k- and ε-equations are not functioning with the stress equations in the same order of treatment, the modeling is not considered to be complete, and thus the overall results will not be improved. To deal with the higher order forms of these equations, the original (unclosed) forms need to be employed to define the turbulence energy and the energy dissipation rate and then some empirical correlations have to be reevaluated for the flows considered in the present study.

The generation and dissipation rates of the k-equation do not require any empirical coefficient. On the other hand, the generation and dissipation rates of the ε-equation have empirical coefficients which have been used by a large number of researchers for more than a decade Therefore, the key terms which may improve the model are the diffusion rates of the k- and ε-equations that need revising for the second-moment closure.

In the second-moment closure, the conventional Boussinesq viscosity (diffusivity) model should be replaced by the second-moment expression. In this process, the empirical coefficient for the diffusion rates of the k- and ε-equations must be determined. However, these coefficients have not yet been evaluated for universal usage. The determination of the values for these diffusion coefficients is attempted in this section for the better prediction of the reattaching and recirculating flows.

2.2 Improvement of k, ε and the Reynolds-Stress Equations

The transport equation which describes the Reynolds-stress variation in an elliptic flow field is derived as

$$U_\ell \frac{\partial \overline{u_i u_j}}{\partial x_\ell} = -(\underbrace{\overline{u_j u_\ell} \frac{\partial U_i}{\partial x_\ell} + \overline{u_i u_\ell} \frac{\partial U_j}{\partial x_\ell}}_{\text{(i)}}) + \underbrace{\overline{\frac{p}{\rho}\left(\frac{\partial u_i}{\partial x_j} + \frac{\partial u_j}{\partial x_i}\right)}}_{\text{(ii)}} \tag{1}$$

$$+ \underbrace{\frac{\partial}{\partial x_\ell}\left[\nu \frac{\partial \overline{u_i u_j}}{\partial x_\ell} - \overline{\frac{p}{\rho}(\delta_{j\ell} u_i + \delta_{i\ell} u_j)} - \overline{u_i u_j u_\ell}\right]}_{\text{(iii)}} - \underbrace{2\nu \overline{\frac{\partial u_i}{\partial x_\ell} \frac{\partial u_j}{\partial x_\ell}}}_{\text{(iv)}}$$

from which the turbulence kinetic energy is also derived. The definition of the turbulence kinetic energy is

$$k \equiv \overline{u_i^2}/2 \tag{2}$$

There are two ways to obtain k; one is to solve Eq. (1) for $\overline{u^2}$, $\overline{v^2}$, and $\overline{w^2}$ and substitute the results into Eq. (2), and the other way is to formulate the transport equation for k itself. When the problem is in a two-dimensional plane coordinate system, the number of equations which need to be solved is the same either way. Here the transport equation for k is converted into the second-moment closure rather than solving all three normal components of the Reynolds stress and summing them to obtain k. This is because the k-equation is widely used as an indicator of turbulence levels. Thus, the k-equation cannot be omitted when one is solving the two-equation model or the algebraic-stress model.

Upon contracting Eq. (1) by setting j equal to i and dividing by 2, it yields the k-equation as follows:

$$U_\ell \frac{\partial k}{\partial x_\ell} = - \overline{u_i u_\ell} \frac{\partial U_i}{\partial x_\ell} - \frac{\partial}{\partial x_\ell} \left(\nu \frac{\partial k}{\partial x_\ell} - \overline{\frac{p}{\rho} u_\ell} - \frac{\overline{u_i^2 u_\ell}}{2} \right) - \nu \overline{\frac{\partial u_i}{\partial x_\ell} \frac{\partial u_i}{\partial x_\ell}} \qquad (3)$$

(i) (ii) (iii)

Terms (i) and (iii) on the right-hand side of Eq. (3) represent the generation and the dissipation rates, respectively. The dissipation can be determined by solving the ε-equation. Term (ii), the diffusion rate, may be replaced by the following form,

$$(ii) = \frac{\partial}{\partial x_\ell} \left(C_k \frac{k}{\varepsilon} \overline{u_i u_\ell} \frac{\partial k}{\partial x_i} \right) \qquad (4)$$

where it is assumed that the second term in the parenthesis is negligibly small in comparison with the third one in (ii) in a large-scale turbulence. This assumption is supported by Irwin's measurements of self-preserving wall jets.[11] The first term in (ii) is kept in the computation in order to account for the viscous effect near the wall.

To obtain the Reynolds stresses, Eq. (1) was closed as follows:

$$U_\ell \frac{\partial \overline{u_i u_j}}{\partial x_\ell} = - \left(\overline{u_j u_\ell} \frac{\partial U_i}{\partial x_\ell} + \overline{u_i u_\ell} \frac{\partial U_j}{\partial x_\ell} \right) + \phi_{ij} + D_{ij} - \frac{2}{3} \delta_{ij} \varepsilon \qquad (5)$$

where the pressure-strain correlation, ϕ_{ij}, is divided into three parts: the Rotta term[12], the rapid term[13] and the viscous term.[14] These are combined and given as follows:

$$\phi_{ij} = - C_{\phi 1} \frac{\varepsilon}{k} \left(\overline{u_i u_j} - \frac{2}{3} \delta_{ij} k \right) - C_{\phi 2} \left(G_{ij} - \frac{2}{3} \delta_{ij} G \right) + C_{\phi 3} \left(H_{ij} - \frac{2}{3} \delta_{ij} G \right) \qquad (6)$$

where

$$G = -\overline{u_i u_j}\,\frac{\partial U_i}{\partial x_j}$$

$$G_{ij} = -\left(\overline{u_i u_k}\,\frac{\partial U_j}{\partial x_k} + \overline{u_j u_k}\,\frac{\partial U_i}{\partial x_k}\right)$$

$$H_{ij} = -\left(\overline{u_i u_k}\,\frac{\partial U_k}{\partial x_j} + \overline{u_j u_k}\,\frac{\partial U_k}{\partial x_i}\right) \qquad (7)$$

$$C_{\phi 1} = 1.5 - 0.125\, f_w$$

$$C_{\phi 2} = 0.4 - 0.015\, f_w$$

$$C_{\phi 3} = 0.015\, f_w$$

and where f_w is a function that controls the strength of the wall correction. Here it is taken to be proportional to the length scale, $k^{3/2}/\varepsilon$.

The diffusion rate, D_{ij}, is conventionally approximated as

$$D_{ij} = \frac{\partial}{\partial x_\ell}\left(C_D\,\frac{k}{\varepsilon}\,\overline{u_\ell u_m}\,\frac{\partial \overline{u_i u_j}}{\partial x_m}\right) \qquad (8)$$

for the computation of $\overline{u_i u_j}$ which is a rather rough approximation because the diffusion rate contains the triple-velocity products. A more extensive model for the triple-velocity products $\overline{u_i u_j u_k}$ is given in the next chapter.

The energy dissipation rate equation is given as

$$U_\ell \frac{\partial \varepsilon}{\partial x_\ell} = -\frac{\varepsilon}{k}\left(C_{\varepsilon 1}\,\overline{u_i u_\ell}\,\frac{\partial U_i}{\partial x_\ell} + C_{\varepsilon 2}\,\nu\,\overline{\frac{\partial u_i}{\partial x_\ell}\frac{\partial u_i}{\partial x_\ell}}\right) \qquad (9)$$

(i) (ii)

$$-\frac{\partial}{\partial x_\ell}\left(\nu\, u_\ell\,\overline{\frac{\partial u_i}{\partial x_\ell}\frac{\partial u_i}{\partial x_\ell}} + 2\,\frac{\nu}{\rho}\,\overline{\frac{\partial p}{\partial x_j}\frac{\partial u_\ell}{\partial x_j}} - \nu\,\frac{\partial \varepsilon}{\partial x_\ell}\right)$$

(iii) (iv) (v)

where $C_{\varepsilon 1} = 1.45$ and $C_{\varepsilon 2} = 1.92$ which have been used to date by a number of researchers as was discussed in section 2.1. The generation (i) and the destruction (ii) terms are evaluated using a direct approach. The diffusion rate is modified in a similar form as Eq. (4):

$$(iii) + (iv) + (v) = \frac{\partial}{\partial x_\ell}\left(C_\varepsilon \frac{k}{\varepsilon}\,\overline{u_i u_\ell}\,\frac{\partial \varepsilon}{\partial x_i}\right) \qquad (10)$$

The coefficients C_k and C_ε were recommended to be 0.31 and 0.15, respectively, by Pope and Whitelaw.[15] Since these values are appropriate only for simple free shear flows, more extensive tests for these coefficients are made for the computations of reattaching shear flows. The optimum values for these coefficients are recommended in the following subsection.

2.3 Computed Results and Discussion

The flow region considered is given in Fig. 1. At the inlet of the flow field the prescribed values are given to all variables; they are basically taken from the experimental data with which the results are compared. Along the top portion and the outflow section of the computational domain, the continuative boundary condition is applied.

At the wall boundaries, the "wall law" is used to specify mean velocities, turbulence kinetic energy, and the Reynolds stresses. On determining proportional constants between k and $\overline{u_i u_j}$ in the wall-vicinity region, we obtained the following relations for $\overline{u_i u_j}$:

$$\overline{u_i u_j} = C_{ij}\, k - (1-\delta_{ij})\, \frac{y}{\rho}\, \frac{dP}{dx} \qquad (11)$$

where x and y are streamwise and transverse coordinates, respectively. The coefficients C_{ij} used here are taken from Ref. 9.

$$C_{11} = 1.21,\ C_{22} = 0.24,\ C_{12} = 0.24. \qquad (12)$$

The dissipation rates along the wall are obtained under the "local equilibrium condition"; that is, the length scale near the wall is proportional to the distance from the wall.

The solution domain consists of a 60Hx5H area with 52x52 grid points. The grid expands at rates of 3% and 2% in x and y directions, respectively. This system was selected after a number of grid tests to produce the optimum grid-independent condition for the computation of mean velocities and the second-moments of the turbulent velocity fluctuations.

Figures 2 through 6 show the computed results of mean velocity and the Reynolds stresses at several streamwise locations behind the step. By using the present model for $Re_H = 32{,}000$, the dimensionless distance, y^+, from the solid wall to the first numerical node-point varies from 16 to 37. Here Re_H denotes the Reynolds number based on the step height H. The typical CPU time consumed for one computation took approximately 30 minutes on a UNIVAC 1100 with about 300 iterations. It is also found that the CPU time depends slightly on the values of the coefficients C_k and C_ε in Eqs. (4) and

(10). Namely, the computations with $C_k = 0.31$ and $C_\epsilon = 0.15$ took about 16% more CPU time and 50 additional iterations than in the cases of $C_k = 0.1$ and $C_\epsilon = 0.3$.

As shown in Figs. 2-6, the profiles of the Reynolds stresses computed with the coefficients $C_k = 0.31$ and $C_\epsilon = 0.15$, which are presently recommended for free shear layers, are about 20% to 30% lower than the experimental data of Driver and Seegmiller[6] for the normal stresses, and 14% lower for the shear stresses. As a result, the levels of the mean velocities in the shear layer region are 20% higher than the experimental data due to a reduction in turbulent diffusion rates.

In order to improve the prediction of these turbulence stresses in the reattaching shear layer, a number of parametric tests have been performed for different values of the diffusion coefficients. It was discerned that the smaller values for C_k and larger values for C_ϵ gave better results in comparison with measured data. This is because the larger values of C_k cause the diffusion of turbulence energy to increase, thus resulting in lower levels of the Reynolds stresses. Similarly, the smaller values of C_ϵ, in turn, increase the dissipation rate of the turbulence energy which results in a reduction in the turbulence energy.

In the present flow field an extra effect is created by the recirculating flow which occurs below the reattaching shear layer. The recirculating flow at the corner of the step and the bottom wall enhances the level of turbulence energy in the separated flow resulting in much higher energy at the reattaching region, and this energy is transported downstream.

After performing parametric tests it was found that the combination of $C_k = 0.1$ and $C_\epsilon = 0.3$ gave the best results for both the mean velocity and the Reynolds stresses. It is also observed in Figs. 2-6 that even the

Boussinesq model* gives better results than the Reynolds-stress model with $C_k = 0.31$ and $C_\varepsilon = 0.15$. The improvement made by the Reynolds-stress model with the new coefficients $C_k = 0.1$ and $C_\varepsilon = 0.3$ is primarily attributed to the inclusion of the second-moments in the diffusion terms which account for the non-isotropic effects. Table 1 compares three models discussed above.

TABLE 1. Diffusion terms for k and ε equations

	C_k	C_ε	C_μ	Agreement With Experiments
Reynolds-stress model				
Pope and Whitelaw	0.31	0.15	Not Used	Bad
Present Study	0.1	0.3	Not Used	Good
Boussinesq Model	Not Used	Not Used	0.09	Fair

The turbulence energy balance is examined by using both the presently determined Reynolds-stress model and the Boussinesq model (cases 2 and 3 in Table 1, respectively) and is shown in Figs. 7-11. The variation of the convection term (Fig. 7) shows that both models give equally reasonable levels at several different locations. For the distributions of the diffusion term, however, the computed results do not agree well with the experimental data in the recirculating region, as shown at x/H = 3.9 in Fig. 8. This is the reason

*The Boussinesq model has the diffusion term in the following form:

$$D_\phi = \frac{\partial}{\partial x_i}\left(0.09\,\frac{k^2}{\sigma\varepsilon}\,\frac{\partial \phi}{\partial x_i}\right)$$

where ϕ represents k or ε, and σ stands for Prandtl number for k or ε.

why the triple-velocity products that represent the diffusion of the Reynolds stresses are examined by using the transport equations for $\overline{u_i u_j u_k}$ in this project. Both the computed distributions of the production (Fig. 9) and the dissipation (Fig. 10) are relatively in accordance with the experimental data although both models always slightly overpredict these quantities.

The overall balance of these terms is compared in Fig. 11. Here the computations are made by using the Reynolds-stress model with the presently recommended diffusion coefficients. It is observed that both the production and dissipation rates predominate in the shear layer near the step, but these levels decay quickly toward downstream. On the contrary, the diffusion and the convection rates stay almost at constant levels in the streamwise direction while they vary rapidly in the transverse direction.

2.4 Summarizing Remarks

In this section, it has been shown that both C_k and C_ε are considerably influential in the results of turbulence quantities and also in the numerical convergence history of the iteration procedure. This indicates that the diffusion process of the turbulence energy in the reattaching shear layer is significant which is in contrast with the boundary layer flows. Thus, it is concluded that the determination of the diffusion coefficients should be done carefully. Probably, a more elaborate functional expression will suffice the requirement rather than employing the constants.

Secondly, it became clear that the third-moment closure should be introduced for better understanding of the diffusion process in the flow recirculation region. This is carried out in the next chapter.

3. THE THIRD-MOMENT CLOSURE MODEL

3.1 Preliminary Remarks

In closing the Reynolds-stress equation (1), the terms of the pressure-strain (ii) and the diffusion (iii) have been approximated by Eqs. (6) and (8), respectively. The question arises whether these approximations are universally accepted or not. With respect to the pressure-strain correlation, several models have been examined in the latest report,[10] and the tests for the best model revealed that three models by Naot et al.,[13] Naot et al.,[16] and Launder et al.[14] produced essentially the same results. In this chapter, attention is primarily focussed on the diffusion term (term (iii) in Eq. (1)).

3.2 Existing Models and the Transport Model for the Third-Moments

Term (iii) in Eq. (1) represents the diffusion of the Reynolds stresses due to molecular viscosity, pressure fluctuations, and turbulence velocity fluctuations. It has been shown that the diffusion due to molecular viscosity and pressure fluctuations is negligibly small at large turbulence Reynolds numbers.* Thus, the triple-velocity products are the most dominant diffusive agency for the Reynolds stresses.

It is known that the higher moments of turbulence fluctuating velocity vary rapidly in the reattaching shear layer towards a solid wall.[5] This affects the accuracy of the computation in the diffusive term of the Reynolds stresses because it contains the third-moment velocity fluctuations. It was discussed in the last report[10] that the triple-velocity products need to be

*These terms appear to be small in most circumstances since turbulence energy budgets balance, to within experimental error, even when these are neglected.

evaluated in a transport equation model rather than in an algebraic form because the convection and generation of the triple-velocity products have to be taken suitably into account according to the change in the mean strain rates. For this reason a full transport equation model of the triple-velocity products is developed and used for the prediction in the reattaching shear flows.

The complete equation is given as

$$U_\ell \frac{\partial}{\partial x_\ell}(\overline{u_i u_j u_k}) = -(\underbrace{\overline{u_i u_j u_\ell}\frac{\partial U_k}{\partial x_\ell} + \overline{u_j u_k u_\ell}\frac{\partial U_i}{\partial x_\ell} + \overline{u_k u_i u_\ell}\frac{\partial U_j}{\partial x_\ell}}_{(i)})$$

$$+(\underbrace{\overline{u_i u_j}\frac{\partial \overline{u_k u_\ell}}{\partial x_\ell} + \overline{u_j u_k}\frac{\partial \overline{u_i u_\ell}}{\partial x_\ell} + \overline{u_k u_i}\frac{\partial \overline{u_j u_\ell}}{\partial x_\ell}}_{(ii)}) \qquad (13)$$

$$-\underbrace{\frac{\partial}{\partial x_\ell}(\overline{u_i u_j u_k u_\ell})}_{(iii)} - \frac{1}{\rho}(\underbrace{\overline{u_i u_j \frac{\partial p}{\partial x_k}} + \overline{u_j u_k \frac{\partial p}{\partial x_i}} + \overline{u_k u_i \frac{\partial p}{\partial x_j}}}_{(iv)})$$

where terms (i) and (ii) represent the generation due to the mean strain rate and the generation due to turbulence stresses, respectively. Terms (iii) and (iv) in Eq. (13) both represent the diffusion rate of the triple-velocity products. Here term (iii) is correlated by assuming Gaussian form as follows:

$$(iii) = \frac{\partial}{\partial x_\ell}(\overline{u_i u_j}\cdot\overline{u_k u_\ell} + \overline{u_i u_k}\cdot\overline{u_j u_\ell} + \overline{u_k u_j}\cdot\overline{u_i u_\ell})$$

and term (iv) is given as:

$$(iv) = -C_p \frac{\varepsilon}{k}\overline{u_i u_j u_k} \qquad (14)$$

Then the final form of Eq. (13) becomes

$$U_\ell \frac{\partial}{\partial x_\ell}(\overline{u_i u_j u_k}) = -(\overline{u_i u_j u_\ell}\frac{\partial U_k}{\partial x_\ell} + \overline{u_j u_k u_\ell}\frac{\partial U_i}{\partial x_\ell} + \overline{u_k u_i u_\ell}\frac{\partial U_j}{\partial x_\ell})$$

$$+ \frac{\partial}{\partial x_\ell}(\nu \frac{\partial \overline{u_i u_j u_k}}{\partial x_\ell}) \qquad (15)$$

$$- (\overline{u_k u_\ell}\frac{\partial \overline{u_i u_j}}{\partial x_\ell} + \overline{u_j u_\ell}\frac{\partial \overline{u_i u_k}}{\partial x_\ell} + \overline{u_i u_\ell}\frac{\partial \overline{u_k u_j}}{\partial x_\ell}) - C_p \frac{\varepsilon}{k}\overline{u_i u_j u_k}$$

In the discussion section the results of the parametric tests are shown for optimum values for the coefficient C_p. The term with the laminar viscosity ν is added to account for the viscous effect.

The above mentioned model is also compared with four existing algebraic models. These are given as follows:

(i) The model of Daly and Harlow[17]

$$\overline{u_i u_j u_k} = -0.25 \frac{k}{\varepsilon}\overline{u_k u_\ell}\frac{\partial \overline{u_i u_j}}{\partial x_\ell} \qquad (16)$$

(ii) The model of Hanjalic and Launder[18]

$$\overline{u_i u_j u_k} = -0.11 \frac{k}{\varepsilon}[\overline{u_\ell u_j}\frac{\partial \overline{u_i u_k}}{\partial x_\ell} + \overline{u_\ell u_i}\frac{\partial \overline{u_j u_k}}{\partial x_\ell} + \overline{u_\ell u_k}\frac{\partial \overline{u_i u_j}}{\partial x_\ell}] \qquad (17)$$

(iii) The model of Shir[19]

$$\overline{u_i u_j u_k} = -0.04 \frac{k^2}{\varepsilon}\frac{\partial \overline{u_i u_j}}{\partial x_k} \qquad (18)$$

(iv) The model of Cormack et al.[20]

$$\overline{u_i u_j u_k} = 4\frac{k^2}{\varepsilon}\{2\alpha_1(\delta_{ij}\delta_{k\ell} + \delta_{ik}\delta_{j\ell} + \delta_{kj}\delta_{i\ell})\frac{\partial k}{\partial x_\ell}$$

$$+ \alpha_2 (a_{ik,j} + a_{ij,k} + a_{kj,i})\}$$

$$+ 2\frac{k}{\varepsilon}\{2\alpha_3(\delta_{ik}a_{j\ell} + \delta_{ij}a_{k\ell} + \delta_{jk}a_{i\ell})\frac{\partial k}{\partial x_\ell} \qquad (19)$$

$$+ \alpha_4 (a_{ik}a_{j\ell,\ell} + a_{ij}a_{k\ell,\ell} + a_{jk}a_{i\ell,\ell})\}$$

where

$$a_{ij} = \overline{u_i u_j} - \frac{2}{3}\delta_{ij}k$$

$$a_{ij,k} = \frac{\partial a_{ij}}{\partial x_k} \qquad (20)$$

The coefficients are given in Table 2.

TABLE 2. Coefficients for α_i

α_1	α_2	α_3	α_4
-8.14×10^{-3}	-1.72×10^{-2}	-4.80×10^{-2}	-1.02×10^{-1}

3.3 Computed Results and Discussion

In order to establish a reliable model for the prediction of the third-moments in the reattaching shear layer, the values of the mean velocities and the second-moments are predetermined to solve the transport equations for $\overline{u_i u_j u_k}$. That is the values of the mean velocities, $\overline{u_i u_j}$, k, and ε computed with the method described in the preceding chapter are stored, and

these values are retrieved when the transport equations for $\overline{u_i u_j u_k}$ are computed. In this way, the existing models for the triple-velocity products are also evaluated and compared with the present third-moment closure model.

Since Eq. (15) represents the transport equations of $\overline{uuu}$, $\overline{uuv}$, $\overline{uvv}$, and $\overline{vvv}$ in a two-dimensional coordinate system, and all four components are associated among themselves in their own equations, these four equations are solved iteratively. The iteration was terminated when the relative residual source of each equation dropped below 3×10^{-12}.

Figures 12-14 compare the triple-velocity product distributions for different values of the coefficient C_p: 5.0, 6.0, and 10.0. The results are also compared with the experimental data of Chandrsuda and Bradshaw.[5] As is observed in this figure, the results are relatively sensitive to the value of C_p. As C_p becomes larger the levels of the triple-velocity products decrease since this term (Eq. (14)) acts as a sink of $\overline{u_i u_j u_k}$. After a number of parametric tests it is found that the value of $C_p = 5.8$ gives the best agreement with both the experimental data of Driver and Seegmiller[23] and of Chandrsuda and Bradshaw.[5] This optimum value corresponds to an inverse coefficient $C_p' = 1/C_p = 0.17$ which is slightly larger than the value of $C_p' = 0.11$ recommended for the Hanjalic and Launder model (see Eq. (17)).

Figures 15 - 20 compare the present computations of the triple-velocity product profile with the experimental data of Chandrsuda and Bradshaw and of Driver and Seegmiller, along with the four algebraic models at several different locations downstream of the step. It is observed that two peaks appear across the shear layer: one along the core of the separated shear layer, the other near the bottom wall. Although all the computations exhibit a similar trend to the experimental data, the predicted levels of $\overline{u_i u_j u_k}$ are

fairly different. While the model of Shir gives the lowest levels for all three components, the model of Cormack et al. provides high levels for $\overline{uvv}$ and $\overline{vvv}$ but not for $\overline{uuv}$. Unlike the model of Cormack et al., the Daly-Harlow model gives high levels only for $\overline{uuv}$ and relatively low levels for both $\overline{uvv}$ and $\overline{vvv}$. Among the algebraic models the results with the Hanjalic-Launder model seem to be consistent showing nearly the same levels for all three components. This is because the Hanjalic-Launder model is the only one that has a symmetric property in all three directions among the algebraic correlations.

Agreement between the present computations with the transport equations and the experimental data is generally much better than that using the algebraic models for two reasons. First, the coefficient, C_p, can be suitably adjusted in the transport equations whereas the algebraic models have been tested only for relatively simple shear flows and not for the reattaching shear layer. Second, the transport equations of $\overline{u_i u_j u_k}$ have a symmetric property in all three directions; thus, the prediction with the transport model is better than the prediction with algebraic models for inhomogeneous flows as well as for homogeneous ones. However, the most important point we should note from these results is that the location of the peak along the separated shear layer is predicted more accurately by using the transport equations than by using algebraic models. This is primarily because the transport model takes both the convection and the generation due to mean strains into account; thus, the trail of energy propagation for the triple-velocity products accords with the experimental data.

The results in Figs. 15-20 also suggest that the transport model needs to be improved to give better profiles near the wall. It is shown in these figures that the computed levels are much higher than the experimental data

near the wall. In the wall adjacent region the model must incorporate a low-Reynolds number effect although the computations in the free shear flow region agree well with the data. The effect of the wall boundary condition on the profiles of $\overline{u_i u_j u_k}$ near the wall was tested by adopting several other models for the numerical nodes next to the wall. However, the influence of the wall boundary condition was negligibly small. Therefore, to improve the prediction of the triple-velocity products in the near-wall region, it is advisable to develop a low-Reynolds number model in order to take the viscous effect into account.

3.4 Summarizing Remarks

The development of the third-moment closure has been pursued through this project. It is observed that the behavior of the triple-velocity products is completely different from that in the boundary layer flows showing rapid decay toward the solid wall in the separated shear layer.

It is noted that the transport equation model dramatically improves the prediction of the triple-velocity products throughout the whole flow region when compared with the algebraic third-moment models. However, more extensive tests are required for improving the transport equation model since the closing of the diffusion and pressure-stress terms of the transport equation has not yet been justified. Moreover, it is recommended that a low-Reynolds number near-wall model be developed for the transport equation model.

4. THE ALGEBRAIC-STRESS MODEL

4.1 Preliminary Remarks

While it is important to improve the prediction of the Reynolds stresses in a wake region, it is equally important to develop a better expression for empirical coefficients for the diffusion rate of the momentum equation. This is because empirically determined coefficients would increase uncertainties and, thus the prediction becomes less accurate for more geometrically complex turbulent flows.

The preceding chapters have dealt with the Reynolds-stress model. However, the algebraic-stress and the $k - \varepsilon$ models, which are the simpler models of turbulence, are considered in this chapter in order to investigate the formulation of the coefficient C_μ by separating from many unknowns which exist in the Reynolds-stress model. If the Reynolds-stress model (RSM) were also used, it would be rather difficult to differentiate between the errors due to the RSM and the C_μ formulation. For futher simplification of the problem, the solid wall is completely eliminated in the wake region, thus considering only the flow behind a disk.

The development of C_μ is based on the algebraic-stress model (ASM) which was originated by Rodi.[8] Although the Reynolds-stress transport model as described in the preceeding chapters is one of the most advanced model, the algebraic-stress model (ASM) improves the prediction over the $k - \varepsilon$ model. Probably the most advantageous point of the algebraic-stress model (ASM) is its simplicity; the solution procedure of a transport equation is not required. The Reynolds stresses are determined by merely solving algebraic equations without using the line relaxation or tridiagonal matrix solvers, and

thus it is much more economical in comparison with the Reynolds-stress transport model.

The above mentioned algebraic-stress model (ASM) is used to formulate the diffusion coefficient of the momentum equations. The model is compared with the conventional empirical constant for the computations of wakes. Since the formulation has to be general, axisymmetric flows have been chosen so that three normal components of the stresses ($\overline{u^2}$, $\overline{v^2}$, and $\overline{w^2}$) and the shear stress ($\overline{uv}$) are solved in the region behind a disk.

4.2 Formulation

The ASM for the axisymmetric flow can be obtained by using the proposal of Rodi.[8] Rodi proposed that the convection-diffusion of the k-equation is proportional to that of the Reynolds-stress transport equation such as

$$\frac{\overline{u_i u_j}}{k}\left(\rho U_m \frac{\partial k}{\partial x_m} - D(k)\right) = \rho U_m \frac{\overline{\partial u_i u_j}}{\partial x_m} - D(\overline{u_i u_j}) \tag{21}$$

where D(k) is given as

$$D(k) = \frac{\partial}{\partial x_j}\left[\mu \frac{\partial k}{\partial x_j} + C_k \rho \frac{k}{\varepsilon} \overline{u_i u_j} \frac{\partial k}{\partial x_i}\right] \tag{22}$$

and where $D(\overline{u_i u_j})$ represents the diffusion rate of $\overline{u_i u_j}$. The final form obtained is given as follows:

$$\frac{\overline{u_i u_j}}{k} - \frac{2}{3}\delta_{ij} = \frac{(1-C_2)(G_{ij} - \frac{2}{3}\delta_{ij}G) + C_{w2}\frac{k^{3/2}}{\varepsilon y}(G_{ij} - D_{ij})}{\varepsilon\left(\frac{G}{\varepsilon} - C_1 - C_{w1}\frac{k^{3/2}}{\varepsilon y}\right)} \tag{23}$$

The ASM is comprised of four algebraic equations for the four Reynolds stresses for a two-dimensional axisymmetric flow. These are given as follows:

$$\overline{u^2} = k\left[\frac{(1-C_2)(G_{11}-\frac{2}{3}G) + C_{w2}\frac{k^{3/2}}{\varepsilon y}(G_{11}-D_{11})}{\varepsilon(\frac{G}{\varepsilon} + C_1 - C_{w1}\frac{k^{3/2}}{\varepsilon y})} + \frac{2}{3}\right] \tag{24}$$

$$\overline{v^2} = k\left[\frac{(1-C_2)(G_{22}-\frac{2}{3}G) + C_{w2}\frac{k^{3/2}}{\varepsilon y}(G_{22}-D_{22})}{\varepsilon(\frac{G}{\varepsilon} + C_1 - C_{w1}\frac{k^{3/2}}{\varepsilon y})} + \frac{2}{3}\right] \tag{25}$$

$$\overline{w^2} = k\left[\frac{(1-C_2)(G_{33}-\frac{2}{3}G) + C_{w2}\frac{k^{3/2}}{\varepsilon y}(G_{33}-D_{33})}{\varepsilon(\frac{G}{\varepsilon} + C_1 - C_{w1}\frac{k^{3/2}}{\varepsilon y})} + \frac{2}{3}\right] \tag{26}$$

$$\overline{uv} = k\left[\frac{(1-C_2)G_{12} + C_{w2}\frac{k^{3/2}}{\varepsilon y}(G_{12}-D_{12})}{\varepsilon(\frac{G}{\varepsilon} + C_1 - C_{w1}\frac{k^{3/2}}{\varepsilon y})}\right] \tag{27}$$

The generation rate of turbulence kinetic energy (Eq. (7)) is defined as

$$G = -[\overline{uv}(\frac{\partial U}{\partial r} + \frac{\partial V}{\partial x}) + \overline{u^2}\frac{\partial U}{\partial x} + \overline{v^2}\frac{\partial U}{\partial r} + \overline{w^2}\frac{V}{r}] \tag{28}$$

The components of the generation (Eq. (7)) for Reynolds stresses ($\overline{u^2}$, $\overline{v^2}$, $\overline{w^2}$ and $\overline{uv}$) are given as

$$G_{11} = -2(\overline{u^2}\frac{\partial U}{\partial x} + \overline{uv}\frac{\partial U}{\partial r}) \tag{29}$$

$$G_{22} = -2(\overline{v^2}\frac{\partial V}{\partial r} + \overline{uv}\frac{\partial V}{\partial x}) \tag{30}$$

$$G_{33} = -2\,\overline{w^2}\frac{V}{r} \tag{31}$$

$$G_{12} = -2(\overline{v^2}\,\frac{\partial U}{\partial r} + \overline{u^2}\,\frac{\partial V}{\partial x} - \overline{uv}\,\frac{V}{r}) \tag{32}$$

The pressure-strain correlation as given by Eq. (6) can be written as:

$$\phi_{11} = -C_1\,\frac{\varepsilon}{k}\,(\overline{u^2} - \frac{2}{3}\,k) - C_2(G_{11} - \frac{2}{3}\,G) + [C_{w1}\,\frac{\varepsilon}{k}\,(\overline{u^2} - \frac{2}{3}\,k) - C_{w2}(2\overline{uv}\,(\frac{\partial V}{\partial x} - \frac{\partial U}{\partial r}))]\,\frac{k^{3/2}}{cy} \tag{33}$$

$$\phi_{22} = -C_1\,\frac{\varepsilon}{k}\,(\overline{v^2} - \frac{2}{3}\,k) - C_2(G_{22} - \frac{2}{3}\,G) + [C_{w1}\,\frac{\varepsilon}{k}\,(\overline{v^2} - \frac{2}{3}\,k) - C_{w2}(2\overline{uv}\,(\frac{\partial U}{\partial r} - \frac{\partial V}{\partial x}))]\,\frac{k^{3/2}}{cy} \tag{34}$$

$$\phi_{33} = -C_1\,\frac{\varepsilon}{k}\,(\overline{w^2} - \frac{2}{3}\,k) - C_2(G_{33} - \frac{2}{3}\,G) + [C_{w1}\,\frac{\varepsilon}{k}\,(\overline{w^2} - \frac{2}{3}\,k)]\,\frac{k^{3/2}}{cy} \tag{35}$$

$$\phi_{12} = -C_1\,\frac{\varepsilon}{k}\,\overline{uv} - C_2\,G_{12} + [C_{w1}\,\frac{\varepsilon}{k}\,\overline{uv} - C_{w2}((\overline{u^2} - \overline{v^2})(\frac{\partial U}{\partial r} - \frac{\partial V}{\partial x}))]\,\frac{k^{3/2}}{cy} \tag{36}$$

The secondary generation rates (Eq. (7)) are given as:

$$H_{11} = -2(\overline{u^2}\,\frac{\partial U}{\partial x} + \overline{uv}\,\frac{\partial V}{\partial x}) \tag{37}$$

$$H_{22} = -2(\overline{v^2}\,\frac{\partial V}{\partial r} + \overline{uv}\,\frac{\partial U}{\partial r}) \tag{38}$$

$$H_{33} = -2\,\overline{w^2}\,\frac{V}{r} \tag{39}$$

$$H_{12} = -(\overline{u^2}\,\frac{\partial U}{\partial y} + \overline{v^2}\,\frac{\partial V}{\partial x} - \overline{uv}\,\frac{V}{r}) \tag{40}$$

The model described above is also compared with the k - ε model. In the k - ε model the Reynolds stresses are computed by using the Boussinesq viscosity concept. That is, all the Reynolds stresses are expressed as follows:

$$\rho\overline{u^2} = \frac{2}{3}\rho k - 2\mu_t \frac{\partial U}{\partial x} \tag{41}$$

$$\rho\overline{v^2} = \frac{2}{3}\rho k - 2\mu_t \frac{\partial V}{\partial r} \tag{42}$$

$$\rho\overline{w^2} = \frac{2}{3}\rho k - 2\mu_t \frac{V}{r} \tag{43}$$

$$\rho\overline{uv} = -\mu_t\left(\frac{\partial U}{\partial r} + \frac{\partial V}{\partial x}\right) \tag{44}$$

Here μ_t is evaluated by using the following equation:

$$\mu_t = C_\mu \rho k^2/\varepsilon \tag{45}$$

In this study four different models are used out of which two are the k - ε models and the other two are ASMs. The difference in the two k - ε models depends upon the value given to C_μ, whether it is a constant value or a functional value derived from the ASM formulation. The difference in the two ASMs is also the same. Hence, we can define the four models as follows:

ASM I —— stresses computed by ASM: $C_\mu = 0.09$

ASM II --- stresses computed by ASM: $C_\mu = f$

k-ε I (standard k - ε model) -- stresses computed by k - ε: $C_\mu = 0.09$

k-ε II (modified k - ε model) -- stresses computed by k - ε: $C_\mu = f$

The function f is derived upon taking the recirculating effects due to two-directional mean strains into account in the formulation. The final form is given as

$$f = \frac{2}{3}\left(\frac{1 - C_2}{G/\epsilon + C_1}\right)/\left[1 + \frac{2}{3}\frac{k^2}{\epsilon^2}\left(\frac{1 - C_2}{G/\epsilon + C_1}\right)^2 \left\{\left(\frac{\partial U}{\partial r}\right)^2 - 4\frac{\partial U}{\partial r}\frac{\partial V}{\partial x} + \left(\frac{\partial V}{\partial x}\right)^2\right\} + \frac{k}{\epsilon}\left(\frac{1 - C_2}{G/\epsilon + C_1}\right)\frac{V}{r}\right] \quad (46)$$

The details of the formulation are given in Appendix.

The constants used in the equations above are given in Table 3.

TABLE 3. Constants

C_k	C_{w1}	C_{w2}	C_1	C_2
0.1	0.125	0.015	1.5	0.4

4.3 Computed Results and Discussion

4.3.1 Computing Details

Exploratory tests were made for different mesh sizes to investigate an optimum grid independent state. Figure 22 gives mean velocity and the Reynolds-stress profiles for different grid sizes at x/D = 6 for the flow geometry in Fig. 21(a).

It is clear that the velocity and the Reynolds-stress profiles approach an equilibrium state for a grid density higher than 42x42. The percentage increase in the properties from one grid size to another is given in Table 4.

TABLE 4. Grid test at r/D = 0.5

Mesh Sizes	32x32 to 42x42	42x42 to 52x52	52x52 to 62x62
U	55.0%	40.0%	5.0%
$\overline{u^2}$	75.0%	25.0%	0.0%
$\overline{v^2}$	66.6%	33.4%	0.0%
$\overline{w^2}$	71.5%	28.5%	0.0%
$\overline{uv}$	62.5%	37.5%	0.0%

In Table 4 it is observed that there is no appreciable change in stresses from 52x52 to 62x62, and this is the reason why we opted for 62x62 as the optimum grid size for all the computations in this chapter.

The initial values for the Reynolds stresses are given by the solutions of the k - ϵ model to ensure stability in the course of the iteration process for the elliptic equations. The computation is terminated when the maximum residual source of the transport equation falls below 0.3 percent of the total source of its equation. Although iteration number depends on many factors such as grid size, flow geometry, boundary conditions, initial conditions, Reynolds number, etc., the typical number ranges from 500 - 800 for the grid size 62x62.

The computational domain for the external flow past a disk consists of 30 step height lengths in the x-direction and 5 step heights in the r-direction. A computation was also made by extending the length from 30 to 40 step heights. When the results obtained with two different geometries were compared with each other, no appreciable difference was observed in any properties. Thus, the geometry of 30 step height lengths is used in x-direction for

all the computations of the external flows. The expansion ratio of 1.05 in both x- and r-directions is found to be the best for this flow geometry. The computational domain of the second geometry shown in Fig. 21(b) consists of a length of 24 step heights in x-direction and two step heights in r-direction. The optimum expansion ratios for this case are found to be 1.05 in x and 1.00 in r-directions.

4.3.2 External Flows

Figure 23 represents the mean velocity profiles at several locations in the flow field beyond the body for the flow geometry which is shown in Fig. 21(a). These are computed by employing k-ε I, k-ε II, ASM I and ASM II. These results are also compared with the experimental data obtained by Carmody.[21] The velocity profiles obtained with the models mentioned above agree with the experimental data outside the separated shear flow region but some disagreement is observed in the recirculating region which might be attributed to the sharp edge of the disk used in the experimental setup causing a larger recirculation region than that predicted in the present study.

Figures 24-27 represent the Reynolds stresses obtained by the ASM and the k - ε model which are compared with the experimental data. The agreement of the stresses obtained by ASM I with the experimental data seems to be better than agreement obtained by the other models. The other models have a similar trend but do not agree with the experiment as closely as ASM I. The agreement of all the numerical models with the experimental data is better in the region outside the recirculation region. Since the k - ε models (k-ε I and k-ε II) cannot take the non-isotropic effect into account, the errors in the results obtained by the k - ε models are significant, particularly in the recirculating region. Despite the improvement with the use of the ASM models,

these models produce a second peak in the recirculating region (near the flow impingement point), which is caused by the streamwise acceleration of the flow near the flow impingement point. This is verified by a test in which the gradient of the mean velocity in x-direction ($\partial U/\partial x$) is omitted resulting in diminishing of this second peak.

From the results mentioned above it is concluded that the algebraic-stress models provide better results in the whole domain of the flow geometry than the k - ε model. This is evident if we observe the results around the flow impingement point (x/D = 3.0) as summarized in Table 5.

TABLE 5. Percentage error for Reynolds stress at r/D = 0.5 in comparison with experimental data

	$\overline{uv}$		$\overline{u^2}$		$\overline{v^2}$		$\overline{w^2}$	
	ASM I	k-ε I	ASM I	k-ε I	ASM I	k-ε I	ASM I	k-ε I
x/D=3	30%	65%	51%	66%	30%	36%	4%	33%
x/D=6	21%	71%	23%	61%	29%	50%	34%	53%
x/D=9	10%	13%	10%	40%	25%	54%	18%	41%

Figure 28 shows the turbulence kinetic energy profiles obtained by using the models considered in this study which are compared with the experimental data. These profiles also show that ASM I is better than the other models.

Figure 29 shows the C_μ distribution at different locations in the flow field and Fig. 30 shows the G/ε profiles at the same locations. It is noted that the C_μ profiles for ASM II and k-ε II are very close to each other and so are the results computed with them. It is also found that there is a strong dependence of stress levels on the G/ε distribution. If G/ε is

higher, then C_μ is lower improving the Reynolds-stress levels; thus ASM I, which has the smallest C_μ in most of the flow domain, is giving the best prediction of the Reynolds stresses among the models considered. The position of the peak of G/ε profiles shown in Fig. 30 computed by ASM I is higher than the peaks produced using the other models. This is because ASM I creates only a small spreading rate.

4.3.3 Internal Flows

For the computations of internal flows only ASM I and k-ε I are employed instead of using four models. Figure 31 represents the mean velocity profiles in the flow direction computed by using ASM I and k-ε I. These are compared with the experimental data of Taylor and Whitelaw[22] for D/D_T = 0.5 (Fig. 21(b)). The results obtained by using ASM I agree well with the experimental data and are better than those obtained using k-ε I. Figures 32-34 represent the three Reynolds-stress profiles ($\overline{u^2}$, $\overline{v^2}$ and $\overline{w^2}$) obtained by using k-ε I and ASM I which are compared with experimental data.[22] In these figures it is also shown that ASM I gives better results for the flows in this geometry.

Even in the internal flow geometry the second peak in the Reynolds-stress profiles appears in the recirculating region near the flow impingement point when using ASM I. This behavior can be explained in the same manner as done in the case of the external flow geometry.

The stresses shown in Figs. 32-34 are very small outside the mixing layer because of negligible generation rates. The stresses then grow slightly near the top wall where the mean velocity decreases rapidly due to the viscous effect from the wall. It is observed that the stresses $\overline{u^2}$ and $\overline{w^2}$ are

higher than $\overline{v^2}$; this feature is similar to that of the wall boundary layer flows.

Figure 35 shows the turbulence kinetic energy distribution obtained with both k-ε I and ASM I, and they are compared with the experimental data. The turbulence kinetic energy shows the highest value near the flow impingement point and it decays towards downstream. Here also it is shown that the results computed by using ASM I agree better with the experimental data. Figure 36 shows the G/ε distribution obtained by ASM I and k-ε I. The trend is similar to the G/ε distribution for the external flow (see Fig. 30).

4.4 Summarizing Remarks

The investigation in this chapter revealed that even the algebraic stress model improves the prediction of the Reynolds stresses considerably when compared with the k - ε model. However, it is also observed that the formulation of C_μ based on the algebraic stress model does not improve the prediction at all. This observation suggests that any model based on the Boussinesq viscosity concept never improves the computations of the Reynolds stresses. For this reason, we should discard the k - ε model type of turbulence model and should create second- or higher-moment closure models for the computation of recirculating flows.

5. APPLICATION TO HEAT TRANSFER PROBLEMS

5.1 Preliminary Remarks

The models developed in the course of this project can be applied to many industrial problems without making many modifications. One application we exercised recently was the computation of the flow and heat transfer rates in periodically corrugated wall channels which appear in a corrugated-wall-channel heat exchanger. The Reynolds-stress model was primarily employed for the computations of the hydrodynamic turbulence variations and the heat-momentum analogy was used to evaluate the heat transfer rates. The results were compared with the computations made by using the $k - \varepsilon$ model. The main concern regarding the differences produced by the two different closure models is whether the non-isotropic effect in the corrugated wall channel is predominant or not. If it is, a significant difference will occur in the results of the computations.

5.2 Computational Method

The computational domain of the flow field is the region ABCDEJIHGF (in Fig. 37). This region consists of two cycles (ABCDIHGF) and the additional region (DEJI). For computations of laminar flows, only one cycle of the corrugated wall channel may be used with a periodic inlet/outlet condition; however, a two-cycle system is needed for complex turbulent flow computations because of numerical instability. In turbulent flow equations more nonlinear transport coefficients appear which results in a very poor history of convergence performance in the course of the iteration process. In addition, a two-pass procedure is employed. That is, the computation was started out with a constant prescribed inlet condition at AF and an outflow condition at EJ. With a line relaxation method, computations were iterated until relative

residual sources of all the transport equations decreased below 2%. Then the periodic condition was activated by transferring the updated values at the section DI to the inlet section AF. Finally, the computation was terminated when all the relative residual sources became less than 0.1%.

At the wall boundaries, the momentum, energy and the turbulence kinetic energy were evaluated from the "law of the wall" while the energy dissipation rate was determined from the "local equilibrium condition," which gives linear variation of the turbulence length scale from the solid wall.

The average friction factor is computed as

$$f = -\frac{b}{\rho U_m^2}\frac{\Delta P}{L} \tag{47}$$

where L is the distance between corresponding planes and ΔP is the average pressure drop between these planes.

The local Nusselt number is obtained by the following equation

$$Nu = \frac{(\dot{q}_w/\Gamma)2b}{|T_w - T_b|} \tag{48}$$

where the constant heat flux condition is employed. The bulk temperature, T_b, is determined as

$$T_b = \frac{\int T|U|dy}{\int |U|dy} \tag{49}$$

where the integrals are to be carried over the cross-sectional area of the channel. The absolute value of the velocity is taken so that the regions with reverse flows are also properly represented. Accordingly, the averaged Nusselt number is defined as

$$\overline{Nu} = \frac{2b}{x\Gamma} \int h dx \qquad (50)$$

where x is the coordinate along the channel wall.

5.3 Computed Results and Discussion

5.3.1 Validation Test of the Reynolds Stresses

Due to lack of experimental data for corrugated wall channel flows, the present numerical model cannot be justified for all the variables obtained. In particular, turbulence quantities such as the Reynolds stresses need to be compared with some experimental data. For this reason, data for a backward facing step flow was chosen to perform a validation test of the Reynolds stresses since the wall region behind a step is similar to the flow field along the wall ABCDE in Fig. 37.

Figure 38 shows the computed results of the mean velocity and the Reynolds-stress distributions in the region behind the step. These results are compared with the experimental data of Driver and Seegmiller.[23] Here 52 x 52 grid points are used for the computational region of 50a x 5a. Both in recirculating and recovering regions, agreement between the present computations and the experimental data is reasonably good (within 30%).

5.3.2 Average Nusselt Number and Skin Friction Coefficients

Figure 39 shows $Nu/Pr^{0.3}$ as a function of Reynolds number. The experimental data of both Izumi et al.[24] and of O'Brien and Sparrow[25] are used for comparison with the present computations. Although the geometry considered by O'Brien and Sparrow has a bend of 120° and a/b = 1.6, the levels of the average Nusselt number seem to be almost the same as those given by Izumi et al. in which a channel with a 90° bend and a/b = 2 were used.

For a/b = 2, the computations by the k - ε model[26] and the present model (RSM) are also compared. It is noteworthy that the RSM improves the prediction by 30% compared with the k - ε model. This observation is consistent with the case of an infinitely long channel with two bends[27] in which it was also discerned that the prediction of the Nusselt number was improved by 20-30% by employing the RSM. This is because the turbulence levels in recirculating regions are correctly evaluated since the RSM accounts for non-isotropic behavior of the Reynolds stresses.

In Fig. 39 the computations for a/b = 1.5 and 1.25 are also shown. It is observed that the difference in the Nusselt number created by the change in corrugation period is minor showing only a 2-3% decrease from a/b = 1.5 to 2.0. This result is also consistent with the experiments of both Izumi et al. (a/b =2) and O'Brien and Sparrow (a/b = 1.6).

Figure 40 shows the skin friction coefficient as a function of Reynolds number. Unlike the case of the Nusselt number, the skin friction rate depends on the corrugation period, a/b. It is observed that the dependency of f on Re is constant for both a/b = 1.25 and 1.5, but for a/b = 2 it decreases slightly as the Reynolds number increases for Re > 3000. In Fig. 40 experimental data for a straight channel is compared with the computations. This figure shows that the computed curves approach the straight channel data as a/b decreases to zero.

5.3.3 Velocity and the Reynolds-Stress Profiles

Figure 41 demonstrates the velocity vectors in different channels. As is shown, recirculating flow is created at each concave corner of the channel. The flow impingement position and the recirculating region are dependent on the corrugation period, a/b.

Computed mean velocities and the Reynolds stresses in the channel where a/b = 2 and for Re = 3000 are shown in Fig. 42. At section B, the mean velocity becomes maximum near the wall AB, and it decreases sharply toward the wall AB. This high shear stress is causing high levels of the stresses $\overline{u^2}$ and $\overline{v^2}$ in that region. If we look at the region near the opposite side of the channel (FG wall), the mean velocity profile is rather smooth although the velocity becomes negative near the wall FG due to a recirculating flow; thus, the normal stresses are not as high as the shear stress $\overline{uv}$. The levels of $\overline{u^2}$ and $\overline{v^2}$ interchange in the next bend section (cross-section CH) showing a relatively high level of $\overline{v^2}$ and a low level of $\overline{u^2}$ because the y component of velocity is predominant over the x component mean velocity. At section H, the $\overline{u^2}$ level is higher near the wall HI, whereas the $\overline{v^2}$ level is high near the opposite side of the channel where the y component of the velocity is still large due to the flow deflection caused by the separation at the corner H. The maximum point of $\overline{u^2}$ moves to the wall DE as we move toward downstream.

5.3.4 Flow in a Channel with Fins

Computations were made for flows in channels which have fins inserted at each bend to cause more deflection of the flow. Local Nusselt number distributions are shown in Figs. 43 and 44 for a/b = 1.25 and 1.5, respectively. Although the general pattern of the distribution is similar for both a/b = 1.25 and 1.5, the distribution depends on the length of the fin. When fins are inserted, the position of the peak of the Nusselt number moves toward the corner C along the wall BC. This is mainly due to the expansion of the recirculating region downstream of the corner B with the insertion of the fins. A similar trend also appears near the wall D. It is commonly observed

that the heat transfer rates increase as the length of the fin increases up to $L_{fin}/b = 0.5$. However, the case of $L_{fin}/b = 0.75$ does not display proportional increases in the heat transfer rates.

The dependence on the length of fins is also shown in Fig. 45 for the average Nusselt number. Here the average Nusselt number increases as L_{fin} increases from 0 to 0.5b, but it stays at constant values for longer fins. The rate of increase in the Nusselt number is larger for higher Reynolds numbers.

5.4 Summarizing Remarks

In this chapter, we saw an application of the Reynolds-stress model to a heat exchanger problem. One of the most impressive features shown here is that the Reynolds-stress model improves the computation of the heat transfer rates by 20-30%. This is mainly because the heat transfer rates are almost proportional to the hydrodynamic variables, thus if the turbulence levels are evaluated correctly so are the heat transfer rates.

6. FINAL REMARKS AND FUTURE WORK

In this project both the second- and third-moment closures have been investigated. The models developed revealed significant improvement in the prediction of complex turbulent shear flows that are accompanied by reattachment, recirculation, and flow deflection. However, the tests were made only for each component of each model--that is, the third-moment transport equations were solved without coupling to the second-moment equations. Although each modeling seems to be successfully carried out, there is no guarantee that these models perform equally well when all the transport equations are solved simultaneously. At that stage it is anticipated that a huge amount of computational time and storage will be required since numbers of transport equations have to be solved by employing sufficiently high density of mesh size. Probably the problem, if any, will be numerical instability rather than a difficulty due to mathematical complexity. For this reason we believe it is extremely important to complete the component study prior to consolidating all the models in one package of the computer code.

It should also be noted that there is plenty of room for improvement of the presently developed second- and third-moment models. For example, a low Reynolds number model coupled with a near-wall correction must be incorporated for the third-moment closure equations. Secondly, the development of the equivalent models for turbulence scalar quantities (heat or chemical species) will undoubtedly advance the state-of-the-art technology in turbulence modeling for applications of many industrial problems.

APPENDIX

FORMULATION OF ASM (Algebraic Stress Model)

The transport equation for the kinetic energy can be written as

$$\frac{Dk}{Dt} = D(k) + G - \varepsilon \tag{A.1}$$

The transport equation for the Reynolds stresses is given by

$$\frac{D\overline{u_i u_j}}{Dt} = D(\overline{u_i u_j}) + G_{ij} - \varepsilon_{ij} + \phi_{ij} \tag{A.2}$$

where $D(\overline{u_i u_j})$ is the diffusion rate of the Reynolds stresses. Rodi[8] proposed that the convection-diffusion string of the k-equation is assumed to be proportional to that of the Reynolds-stress transport equation, as given in the equation below.

$$\frac{\overline{u_i u_j}}{k}\left(\frac{Dk}{Dt} - D(k)\right) = \frac{D\overline{u_i u_j}}{Dt} - D(\overline{u_i u_j}) \tag{A.3}$$

From (A.2) and (A.3) we have

$$\frac{\overline{u_i u_j}}{k}\left(\frac{Dk}{Dt} - D(k)\right) = G_{ij} - \varepsilon_{ij} + \phi_{ij} \tag{A.4}$$

Now, substituting Eq. (A.1) in (A.4) we have

$$\frac{\overline{u_i u_j}}{k}(G - \varepsilon) = G_{ij} - \varepsilon_{ij} + \phi_{ij} \tag{A.5}$$

where ϕ_{ij} is defined in Eqs. (33)-(36). From the proposal of Daly-Harlow,[17] we have.

$$\epsilon_{ij} = \frac{\overline{u_i u_j}}{k}\,\epsilon$$

Using the above result in (A.5) we have

$$\frac{\overline{u_i u_j}}{k}\,G = G_{ij} + \phi_{ij} \qquad \text{(A.6)}$$

or

$$\frac{\overline{u_i u_j}}{k}\,G = G_{ij} + [-C_1\epsilon(\frac{\overline{u_i u_j}}{k} - \frac{2}{3}\,\delta_{ij}) - C_2(G_{ij} - \frac{2}{3}\,\delta_{ij}G)]$$

$$+ [C_{w1}\,\frac{\epsilon}{k}\,(\overline{u_i u_j} - \frac{2}{3}\,\delta_{ij}k)$$

$$+ C_{w2}(G_{ij} - H_{ij})]\,\frac{k^{3/2}}{\epsilon y} \qquad \text{(A.7)}$$

After rearranging, we have

$$(\frac{\overline{u_i u_j}}{k} - \frac{2}{3}\,\delta_{ij})[G + C_1\epsilon - \frac{k^{3/2}}{y}\,C_{w1}]$$

$$= G_{ij} - C_2G_{ij} + C_2\,\frac{2}{3}\,\delta_{ij} - \frac{2}{3}\,\delta_{ij}G + [C_{w2}(G_{ij} - H_{ij})]\,\frac{k^{3/2}}{\epsilon y}$$

Regrouping the terms we have

$$\epsilon(\frac{\overline{u_i u_j}}{k} - \frac{2}{3}\,\delta_{ij})(\frac{G}{\epsilon} + C_1 - \frac{k^{3/2}}{\epsilon y}\,C_{w1})$$

$$= (1-C_2)(G_{ij} - \frac{2}{3}\,\delta_{ij}G) + C_{w2}\,\frac{k^{3/2}}{\epsilon y}\,(G_{ij} - H_{ij})$$

Finally, the equation for Reynolds stresses is given as follows:

$$\frac{\overline{u_1 u_1}}{k} - \frac{2}{3}\delta_{ij} = \frac{(1-C_2)(G_{11} - \frac{2}{3}\delta_{11}G) + C_{w2}\frac{k^{3/2}}{\varepsilon y}(G_{11} - H_{11})}{\varepsilon(\frac{G}{\varepsilon} + C_1 - \frac{k^{3/2}}{\varepsilon y}C_{w1})} \tag{A.8}$$

By neglecting wall effects and the secondary mean strains, $\overline{u^2}$, $\overline{v^2}$ and $\overline{uv}$ are given as follows

$$\overline{u^2} = \frac{2}{3}\frac{k}{\varepsilon}\frac{(1-C_2)}{(\frac{G}{\varepsilon} + C_1)}\overline{uv}\left[\frac{\partial V}{\partial x} - 2\frac{\partial U}{\partial r}\right] + \frac{2}{3}k \tag{A.9}$$

$$\overline{v^2} = \frac{2}{3}\frac{k}{\varepsilon}\frac{(1-C_2)}{(\frac{G}{\varepsilon} + C_1)}\overline{uv}\left[\frac{\partial U}{\partial r} - 2\frac{\partial V}{\partial x}\right] + \frac{2}{3}k \tag{A.10}$$

$$-\overline{uv} = \frac{k}{\varepsilon}\frac{(1-C_2)}{(\frac{G}{\varepsilon} + C_1)}\left[\overline{v^2}\frac{\partial U}{\partial r} + \overline{u^2}\frac{\partial V}{\partial x} - \overline{uv}\frac{V}{r}\right] \tag{A.11}$$

Substituting Eqs. (A.9) and (A.10) into (A.11) and simplifying, we get

$$-\overline{uv} - \frac{2}{3}\frac{k^2}{\varepsilon^2}\left(\frac{1-C_2}{\frac{G}{\varepsilon} + C_1}\right)^2\overline{uv}\left(\left(\frac{\partial U}{\partial r}\right)^2 - 4\frac{\partial U}{\partial r}\frac{\partial V}{\partial x} + \left(\frac{\partial V}{\partial x}\right)^2\right) - \overline{uv}\frac{k}{\varepsilon}\left(\frac{1-C_2}{\frac{G}{\varepsilon} + C_1}\right)\frac{V}{r}$$

$$= \frac{2}{3}k^2\frac{(1-C_2)}{\varepsilon(\frac{G}{\varepsilon} + C_1)}\left[\frac{\partial U}{\partial r} + \frac{\partial V}{\partial x}\right] \tag{A.12}$$

After multiplying both sides by ρ and rearranging, we have

$$\frac{-\rho\overline{uv}}{[\frac{\partial U}{\partial r} + \frac{\partial V}{\partial x}]} = \frac{2}{3}\rho k^2 \frac{(1-C_2)}{\epsilon(\frac{G}{\epsilon} + C_1)} / [1 + (\frac{k^2}{\epsilon^2} \frac{1-C_2}{\frac{G}{\epsilon} + C_1})^2 \cdot$$

$$\cdot\left((\frac{\partial U}{\partial r})^2 - 4 \frac{\partial U}{\partial r} \frac{\partial V}{\partial x} + (\frac{\partial V}{\partial x})^2\right) + \frac{k}{\epsilon}(\frac{1-C_2}{\frac{G}{\epsilon} + C_1}) \frac{V}{r}] \qquad \text{(A.13)}$$

Since $\mu_t = -\rho\overline{uv}/(\frac{\partial U}{\partial r} + \frac{\partial V}{\partial x})$ and $C_\mu = \mu_t \epsilon/\rho k^2$, we have

$$C_\mu = \frac{2}{3}(\frac{1-C_2}{\frac{G}{\epsilon} + C_1}) / [1 + \frac{2}{3}\frac{k^2}{\epsilon^2}(\frac{1-C_2}{\frac{G}{\epsilon} + C_1})^2 \left((\frac{\partial U}{\partial r})^2 - 4 \frac{\partial U}{\partial r} \frac{\partial V}{\partial x} + (\frac{\partial V}{\partial x})^2\right)$$

$$+ \frac{k}{\epsilon}(\frac{1-C_2}{\frac{G}{\epsilon} + C_1}) \frac{V}{r}] \qquad \text{(A.14)}$$

REFERENCES

1. Etheridge, D. W. and Kemp, P. H., "Measurements of Turbulent Flow Downstream of a Rearward-Facing Step," Journal of Fluid Mechanics, Vol. 86, 1978, pp. 545-566.

2. Kim, J., Kline, S. J. and Johnston, J. P., "Investigation of a Reattaching Turbulent Shear Layer: Flow Over a Backward-Facing Step," Journal of Fluids Engineering, Vol. 102, 1980, pp. 302-308.

3. Smyth, R., "Turbulent Flow Over a Plane Symmetric Sudden Expansion," Journal of Fluids Engineering, Vol. 101, 1979, pp. 348-353.

4. Eaton, J. K. and Johnston, J. P., "An Evaluation of Data for the Backward-Facing Step Flow," Stanford Conferences on Complex Turbulent Flows, 1980.

5. Chandrsuda, C. and Bradshaw, P., "Turbulence Structure of a Reattaching Mixing Layer," Journal of Fluid Mechanics, Vol. 110, 1980, pp. 171-194.

6. Driver, D. M. and Seegmiller, H. L., "Features of a Reattaching Turbulent Shear Layer in Divergent Channel Flow," AIAA Journal, Vol. 23, No. 2, 1985, pp. 163-171.

7. Amano, R. S. and Goel, P., "Computations of Turbulent Flow Beyond Backward-Facing Steps by Using Reynolds-Stress Closure," AIAA Journal, Vol. 23, No. 9, 1985, pp. 1356-1361.

8. Rodi, W., "The Prediction of Free Boundary Layers by Use of a Two Equation Model of Turbulence," Ph.D. Thesis, University of London, December 1972.

9. Amano, R. S. and Goel, P., "A Study of Reynolds-Stress Closure Model," NASA-CR-174342, 1985.

10. Amano, R. S., "A Study of the Second and Third Order Closure Models of Turbulence for Prediction of Separated Shear Flows," NASA-CR-176127, 1985.

11. Irwin, H. P. A. H., "Measurements in a Self-Preserving Plane Wall Jet in a Positive Pressure Gradient," Journal of Fluid Mechanics, Vol. 61, 1973, pp. 33-63.

12. Rotta, J. C., "Statistische Theorie Nichthomogener Turbulenz," Zeitschrift fur Physik, Vol. 129, 1951, pp. 547-572.

13. Naot, D., Shavit, A., and Wolfshtein, M., "Interaction Between Components of the Turbulent Velocity Correlation Tensor Due to Pressure Fluctuations," Israel Journal of Technology, Vol. 8, No. 3, 1970, pp. 259-269.

14. Launder, B. E., Reece, G. J. and Rodi, W., "Progress in the Development of a Reynolds-Stress Turbulence Closure," Journal of Fluid Mechanics, Vol. 68, 1975, pp. 537-566.

15. Pope, S. B. and Whitelaw, J. H., "The Calculation of Near-Wake Flows," Journal of Fluid Mechanics, Vol. 73, 1976, pp. 9-32.

16. Naot, D., Shavit, A. and Wolfshtein, M., "Two-Point Correlation Model and the Redistribution of Reynolds Stresses," The Physics of Fluids, Vol. 16, No. 6, 1973, pp. 738-743.

17. Daly, B. J. and Harlow, F. H., "Transport Equations in Turbulence," The Physics of Fluids, Vol. 13, No. 11, 1970, pp. 2634-2649.

18. Hanjalic, K. and Launder, B. E., "A Reynolds Stress Model of Turbulence and Its Application to Thin Shear Flows," Journal of Fluid Mechanics, Vol. 52, Part 4, 1972, pp. 609-638.

19. Shir, C. C., "A Preliminary Numerical Study of Atmospheric Turbulent Flows in the Idealized Planetary Boundary Layer," Journal of Atmospheric Science, Vol. 30, 1973, pp. 1327-1339.

20. Cormack, D. E., Leal, L. G., and Seinfeld, J. H., "An Evaluation of Mean Reynolds Stress Turbulence Models: The Triple-Velocity Correlation," ASME Journal of Fluids Engineering, Vol. 100, 1978, pp. 47-54.

21. Carmody, T., "Establishment of the Wake Behind a Disk," ASME Journal of Basic Engineering, Vol. 86, 1964, pp. 869-882.

22. Taylor, A.M.K.P. and Whitelaw, J. H., "Velocity Characteristics in the Turbulent Near Wakes of Confined Axisymmetric Bluff Bodies," Journal of Fluid Mechanics, Vol. 139, 1984, pp. 391-416.

23. Driver, D. M. and Seegmiller, H. L., Private Communications, 1985.

24. Izumi, R. Yamashita, H., Kaga, S. and Miyajima, N., "Fluid Flow and Heat Transfer in Corrugated Wall Channels--Experimental Study for Many Bends," Proceedings of the 19th JSME Symposium on Heat Transfer, Paper No. A101, 1982.

25. O'Brien, J. E. and Sparrow, E. M., "Corrugated-Duct Heat Transfer, Pressure Drop, and Flow Visualization," ASME Journal of Heat Transfer, Vol. 104, No. 3, 1982, pp. 410-416.

26. Amano, R. S., "A Numerical Study of Laminar and Turbulent Heat Transfer in a Periodically Corrugated Wall Channel," ASME Journal of Heat Transfer, Vol. 107, No. 3, 1985, pp. 564-569.

27. Amano, R. S., "A Numerical Study of Turbulent Heat Transfer in a Channel with Bends," ASME Paper No. 85-HT-20, 23rd National Heat Transfer Conference, Denver, August 1985.

FIGURES

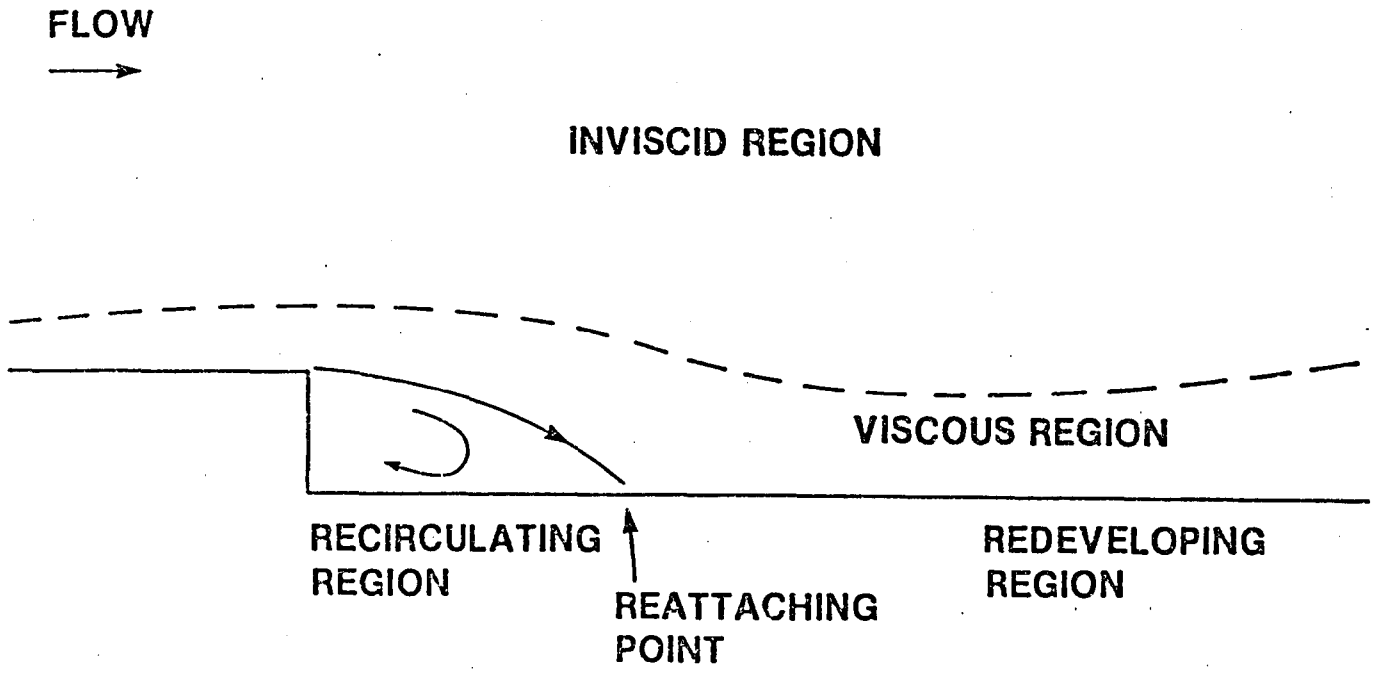

Figure 1 Flow domain

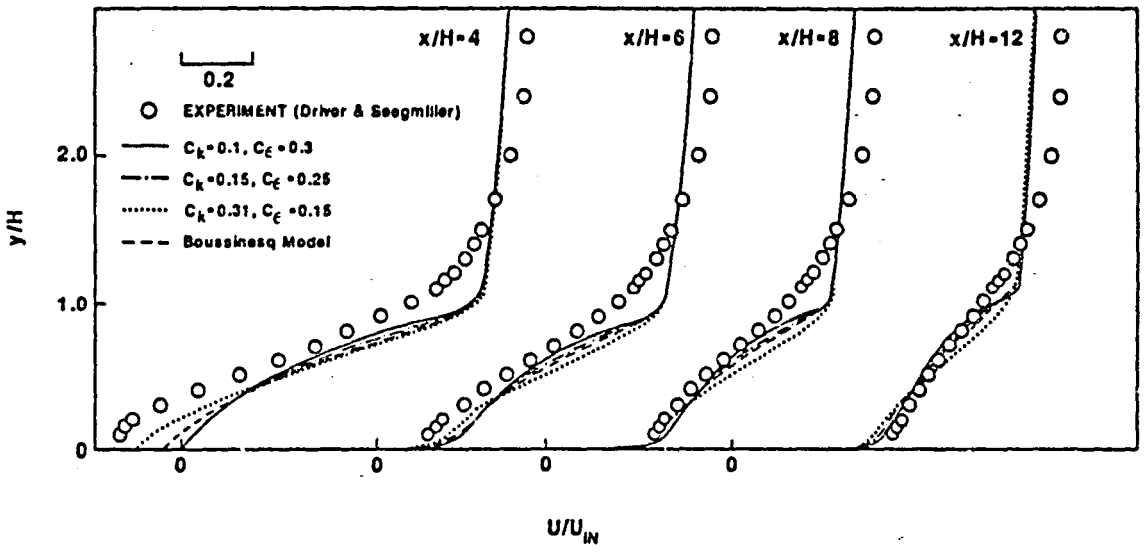

Figure 2 Mean velocity profiles behind the step

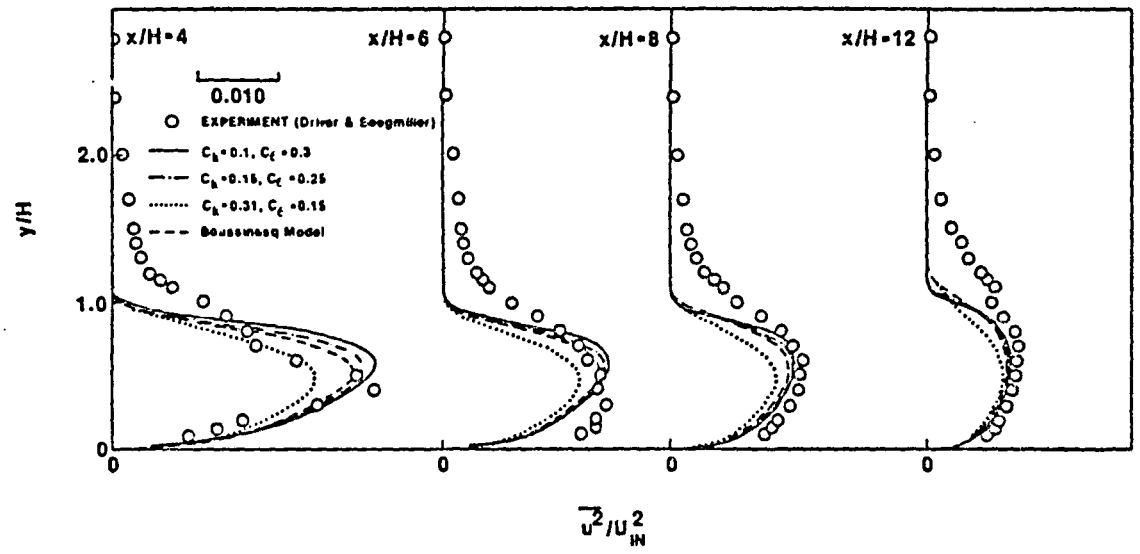

Figure 3 $\overline{u^2}$ profiles behind the step

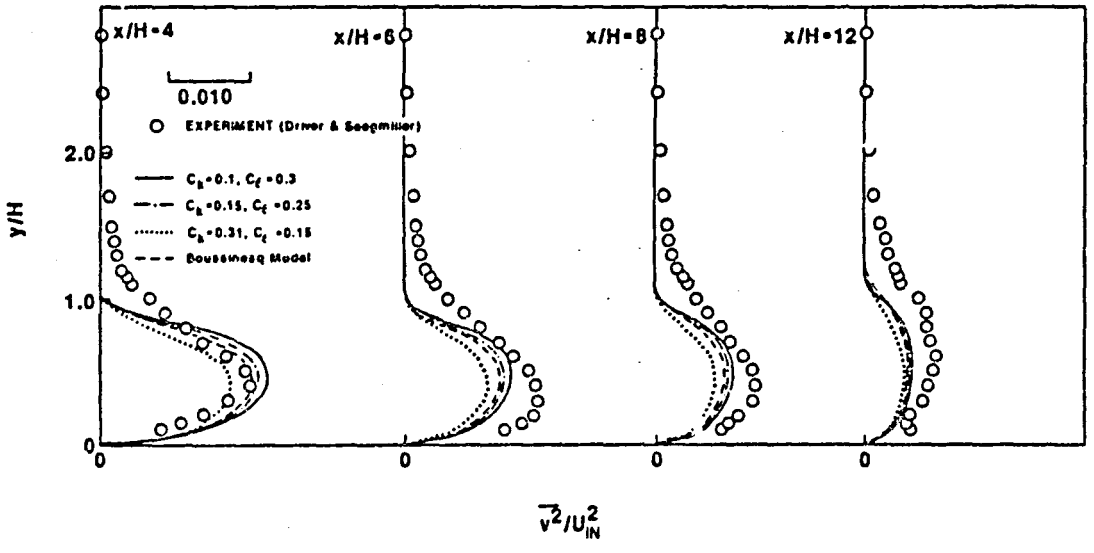

Figure 4 $\overline{v^2}$ profiles behind the step

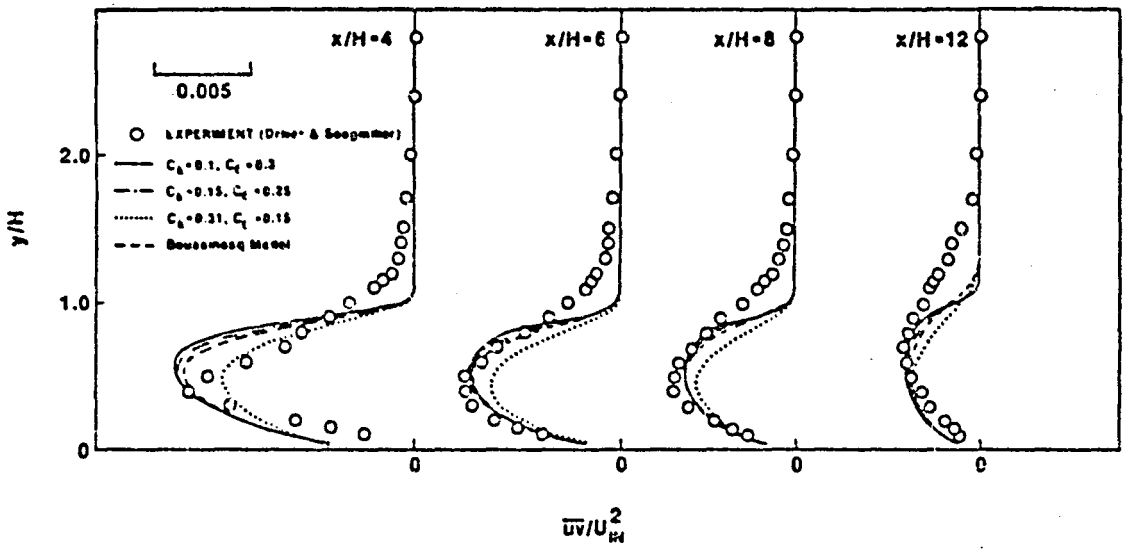

Figure 5 $\overline{uv}$ profiles behind the step

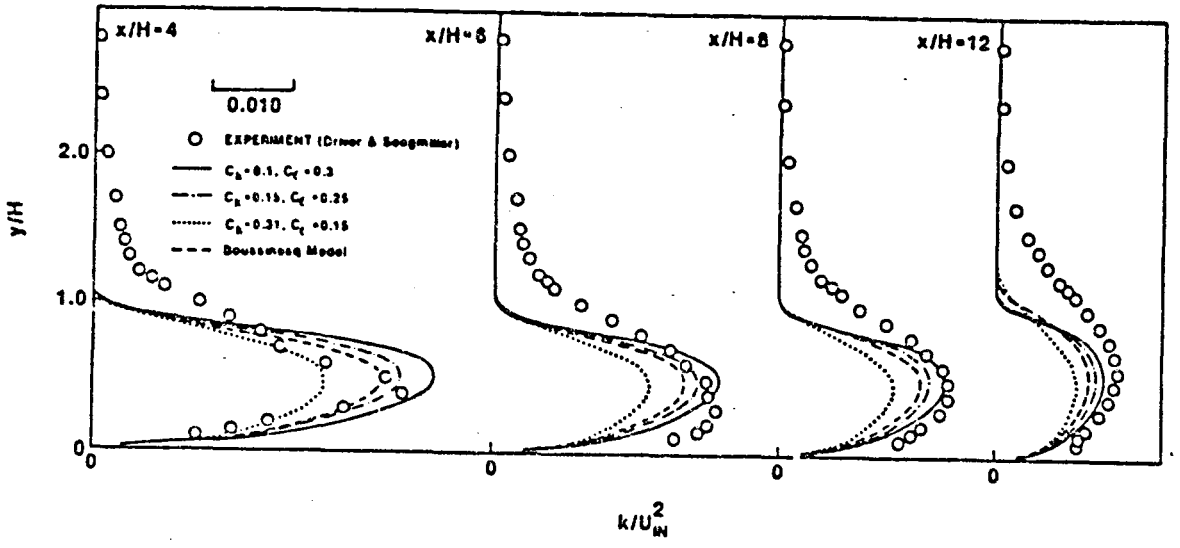

Figure 6 k profiles behind the step

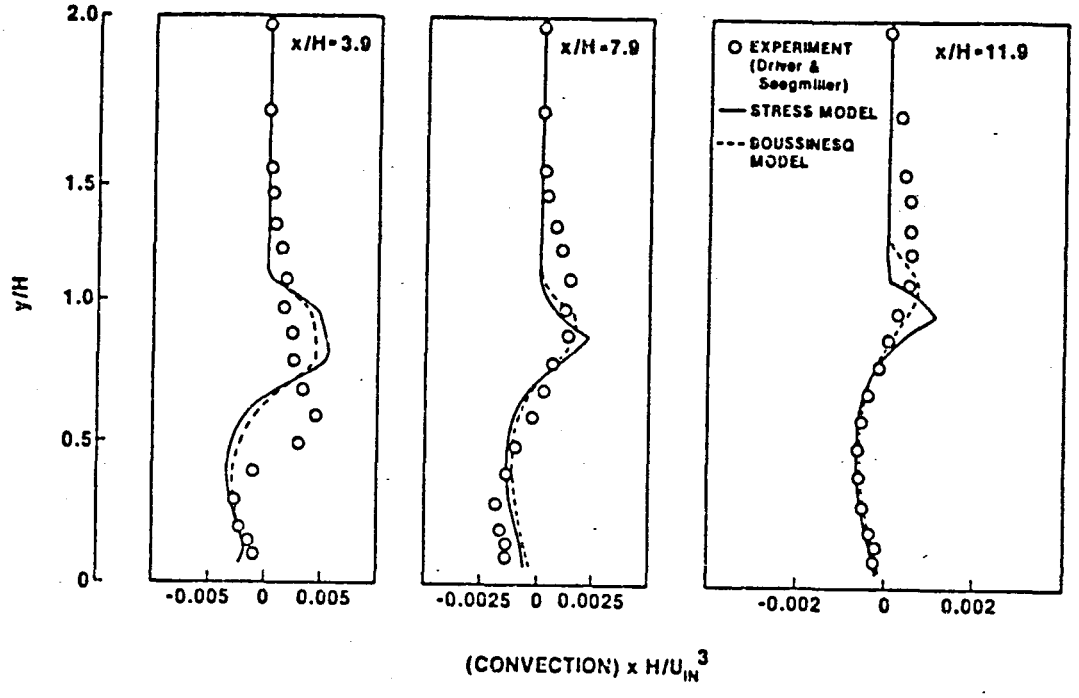

Figure 7 Convection of turbulence energy

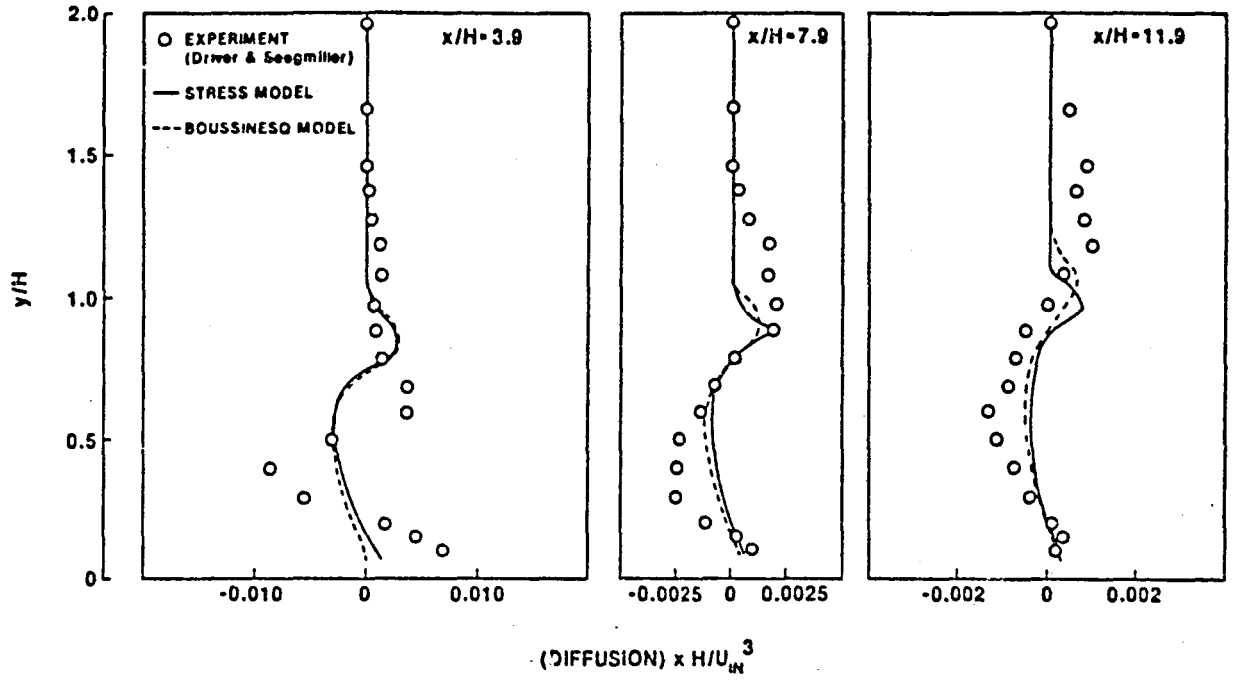

Figure 8 Diffusion of turbulence energy

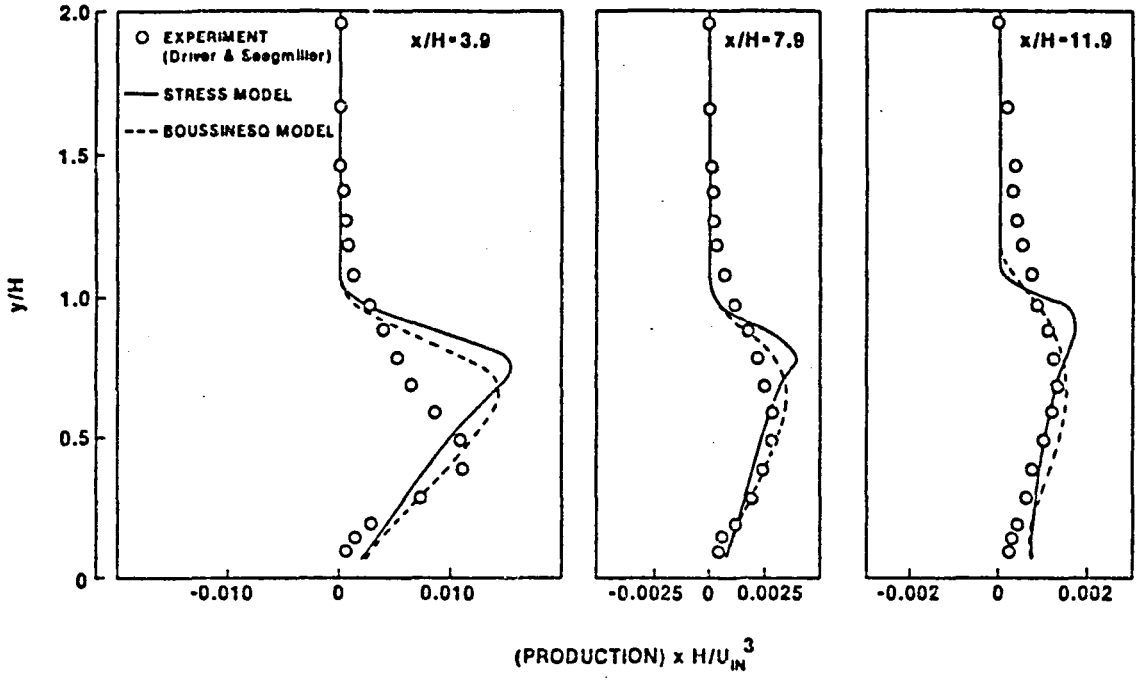

Figure 9 Production of turbulence energy

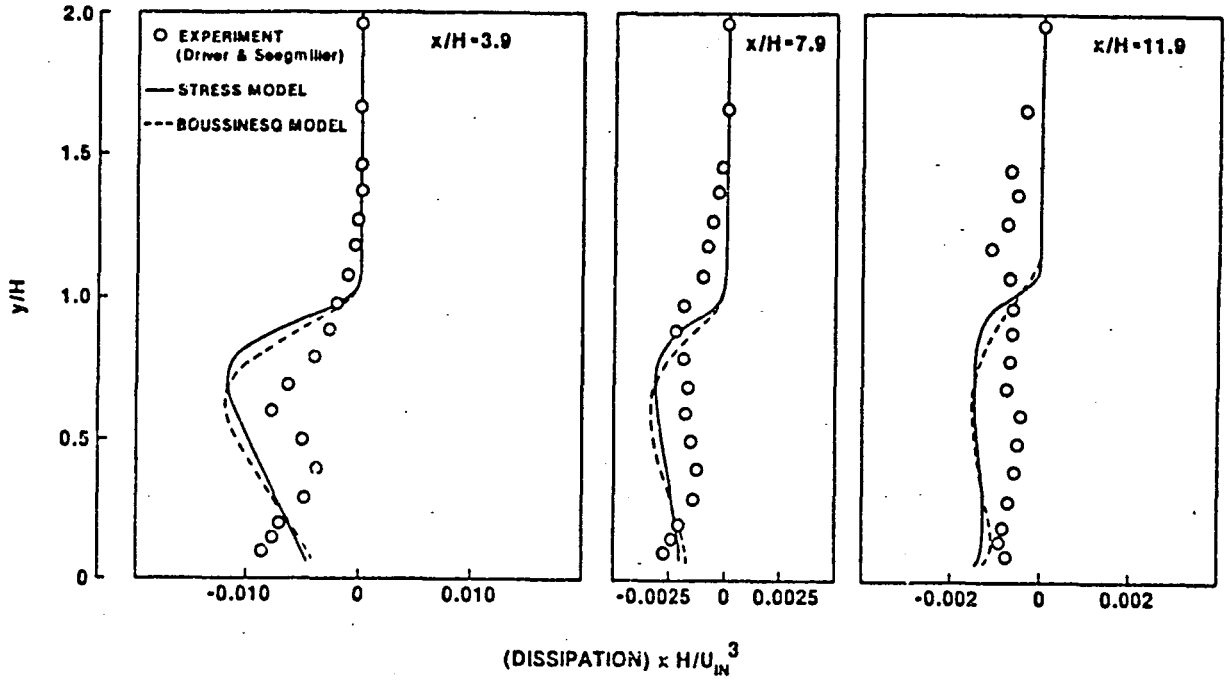

Figure 10 Dissipation of turbulence energy

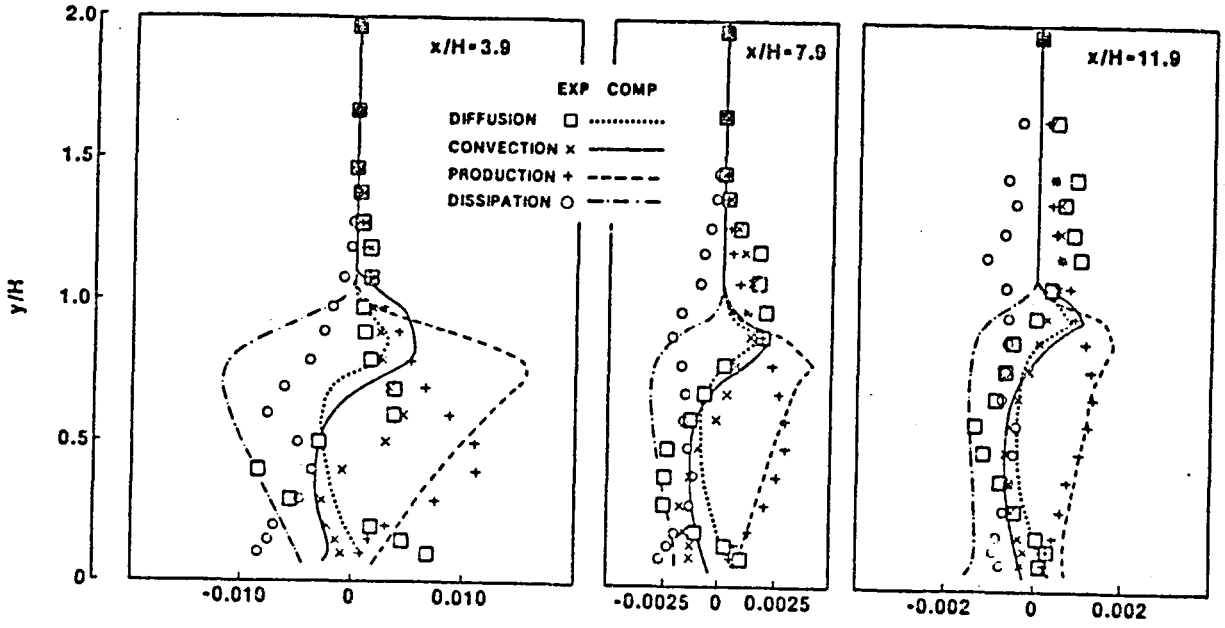

Figure 11 Turbulence energy balance

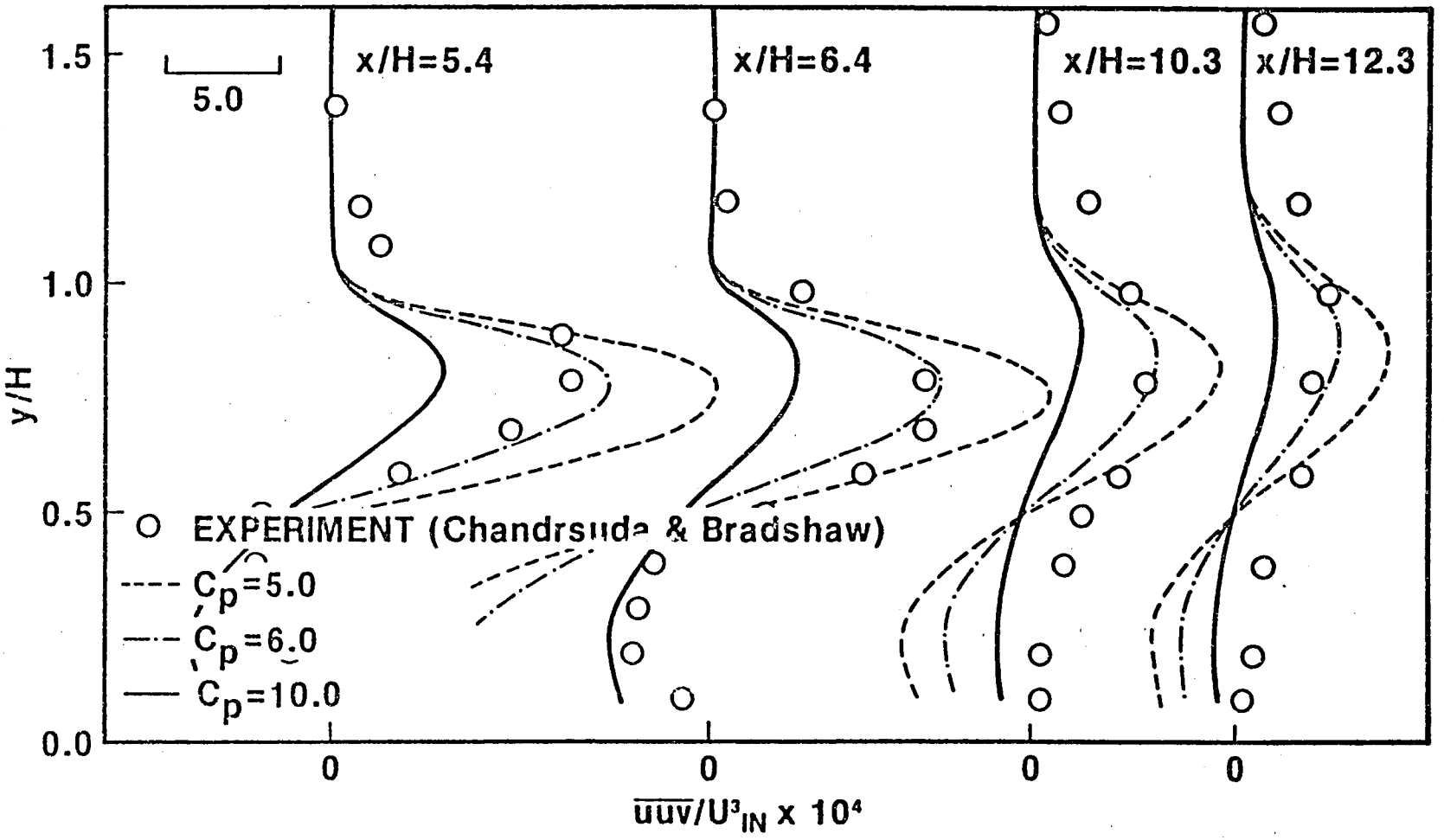

Figure 12 Triple-velocity products for different values of C_p

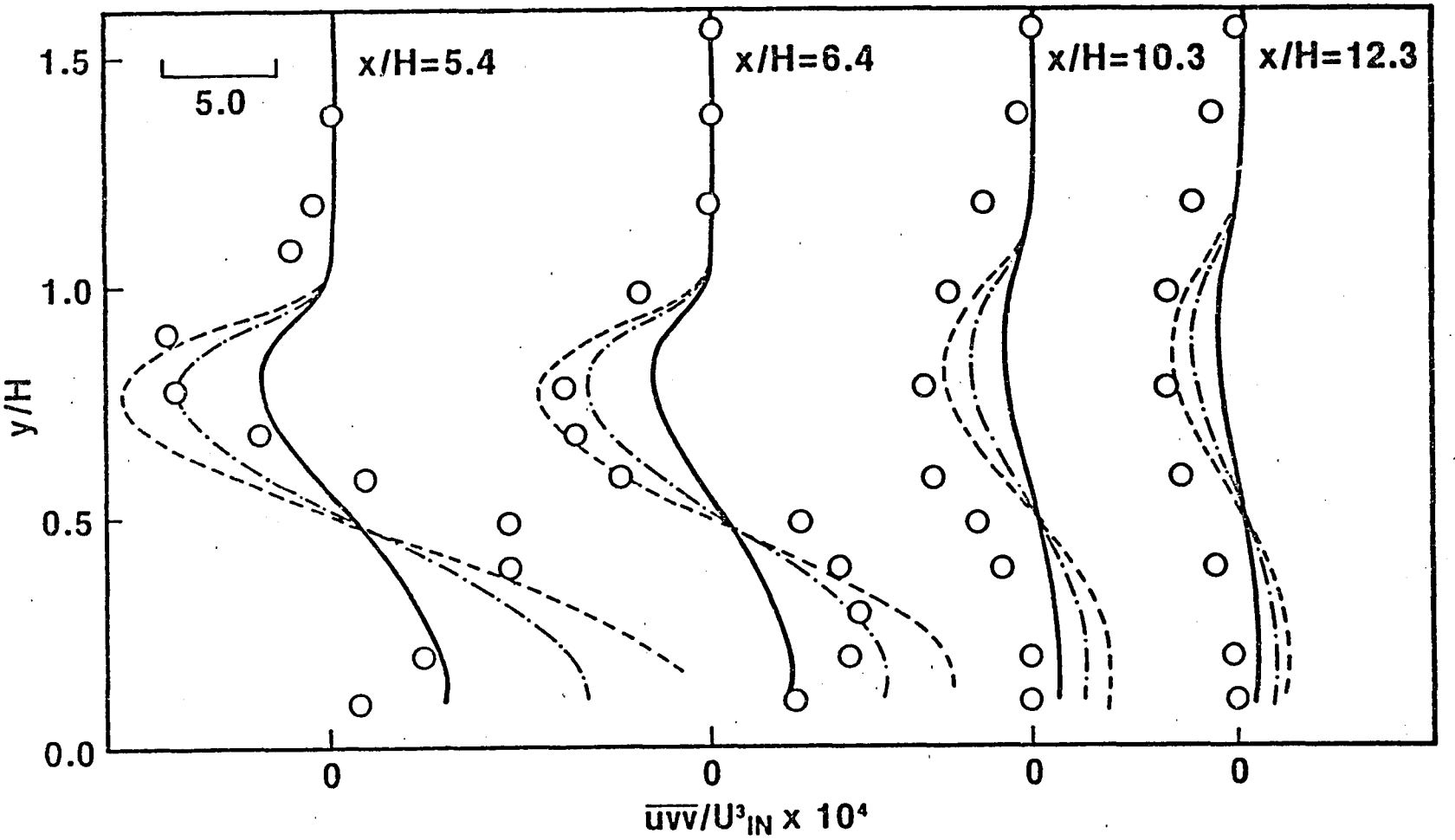

Figure 13 Triple-velocity products for the different values of C_p

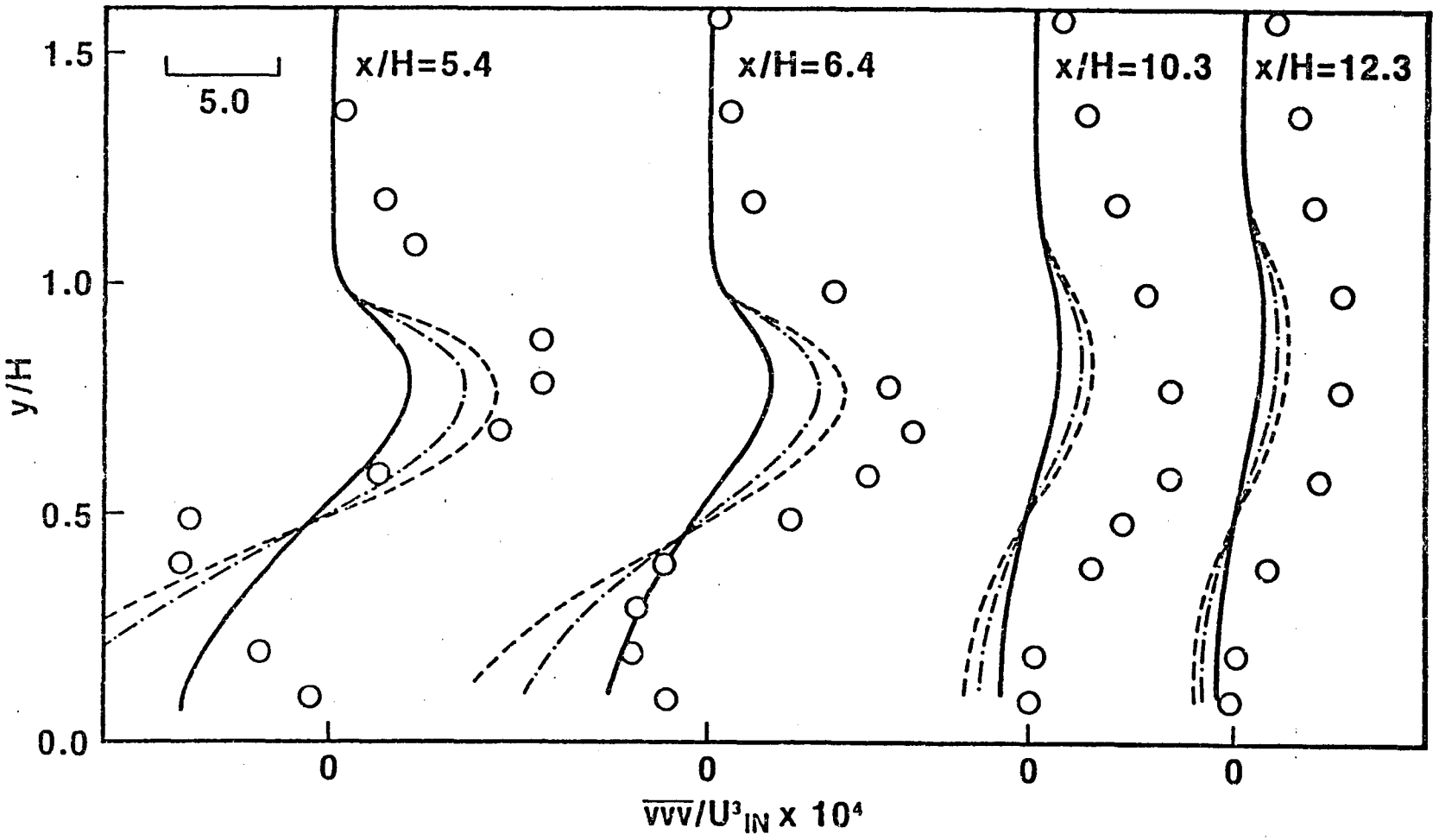

Figure 14 Triple-velocity products for different values of C_p

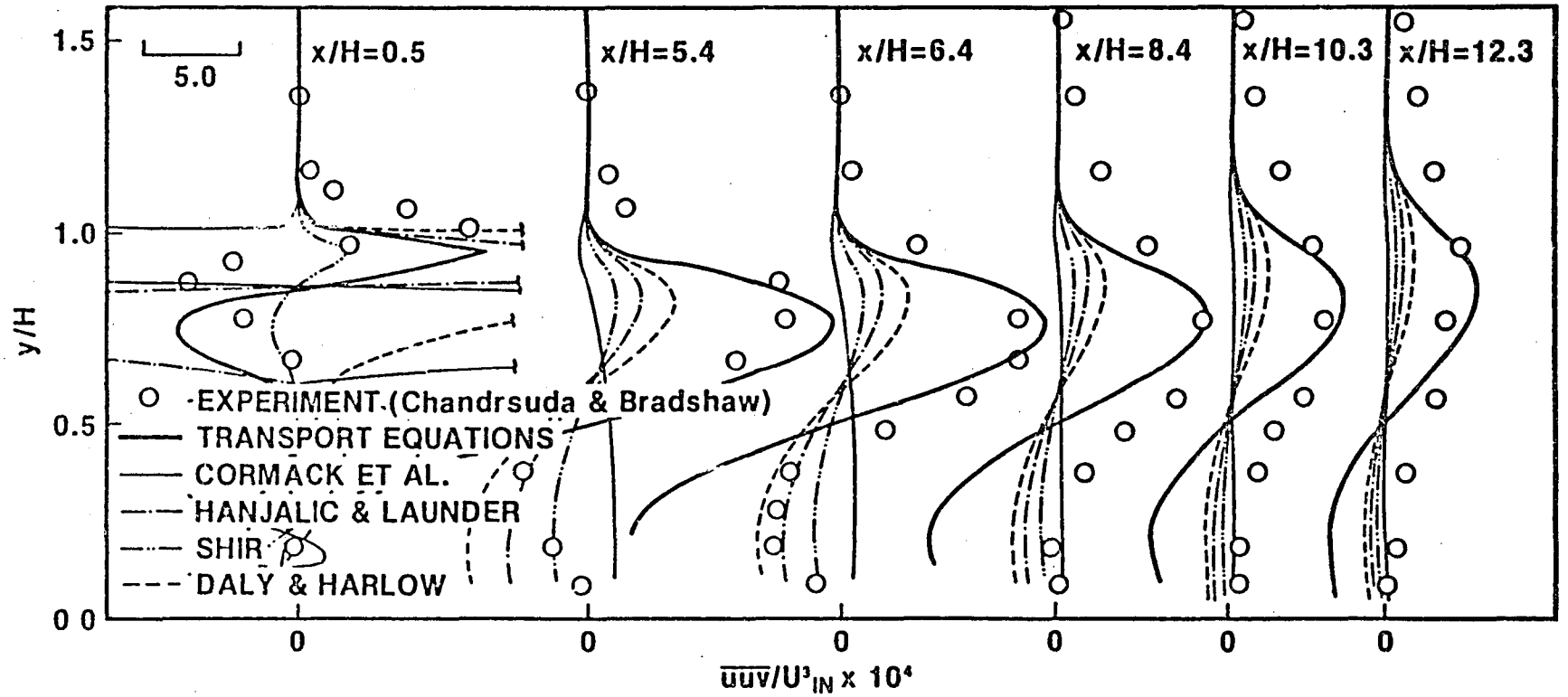

Figure 15 Triple-velocity products

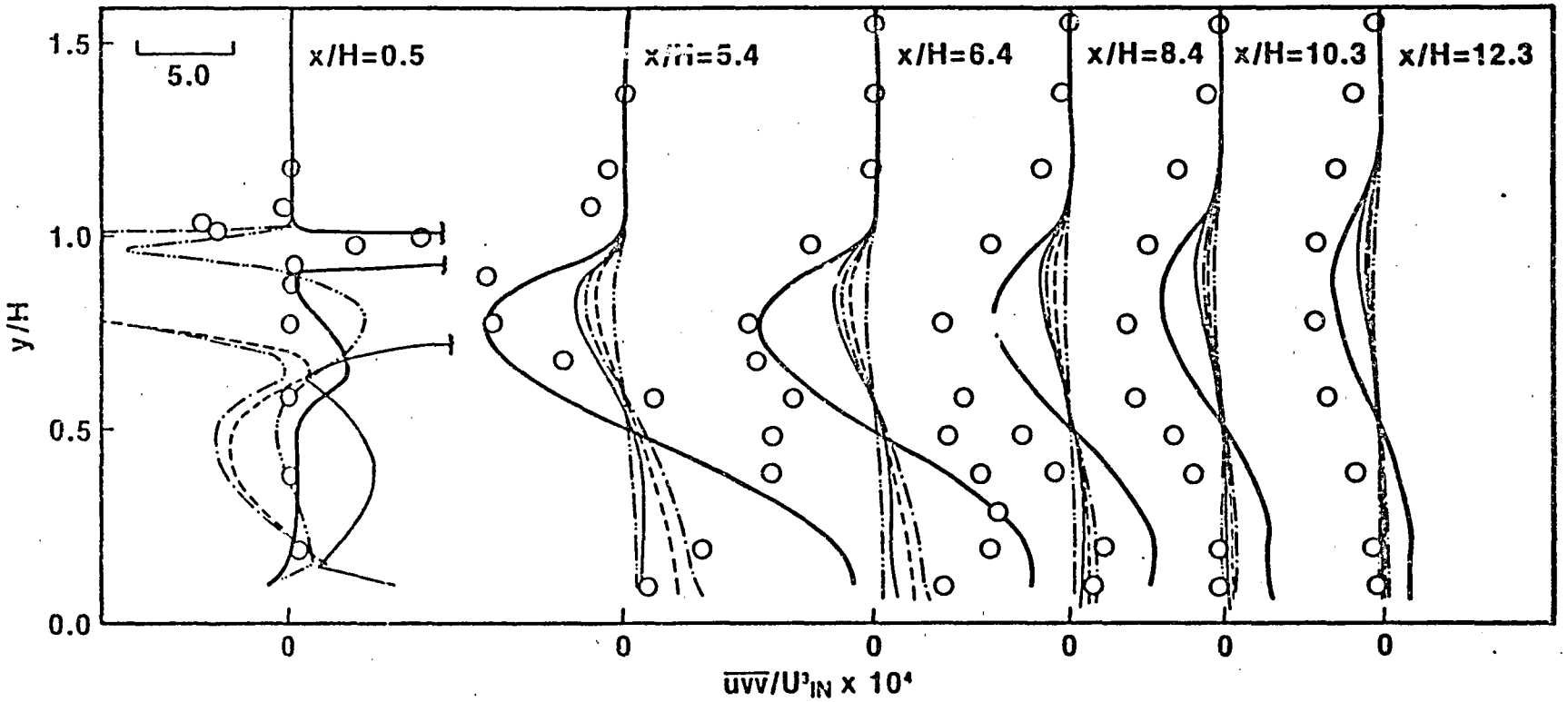

Figure 16 Triple-velocity products

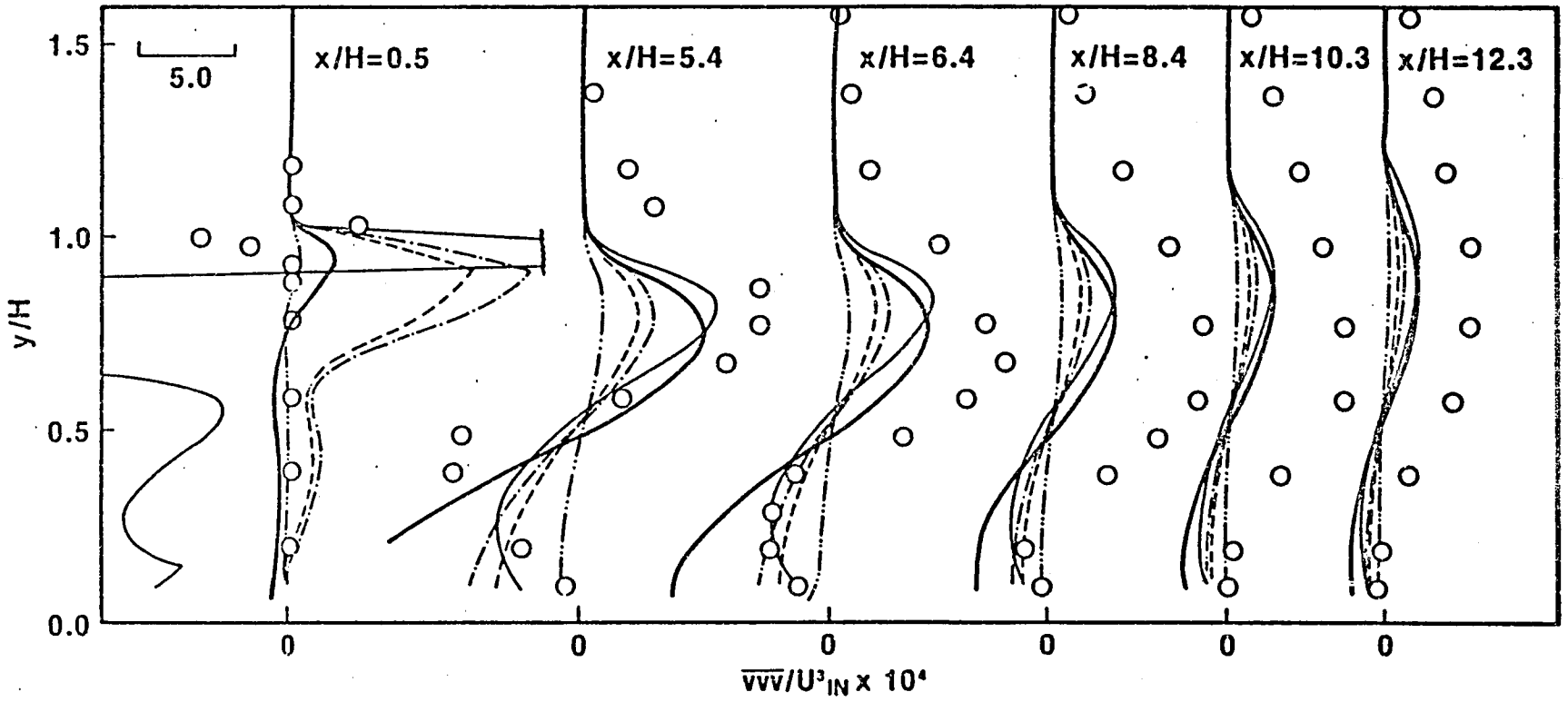

Figure 17 Triple-velocity products

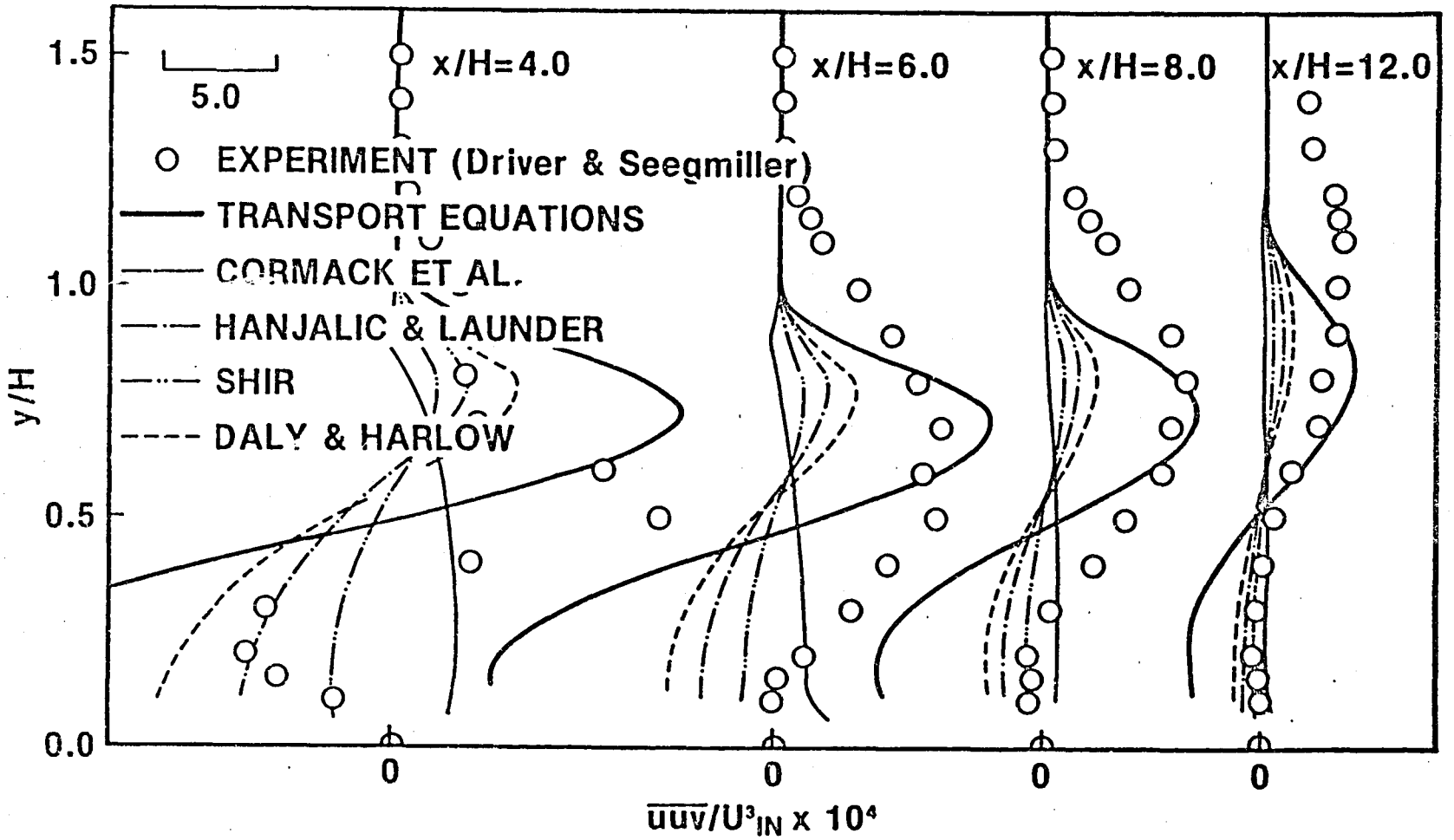

Figure 18 Triple-velocity products

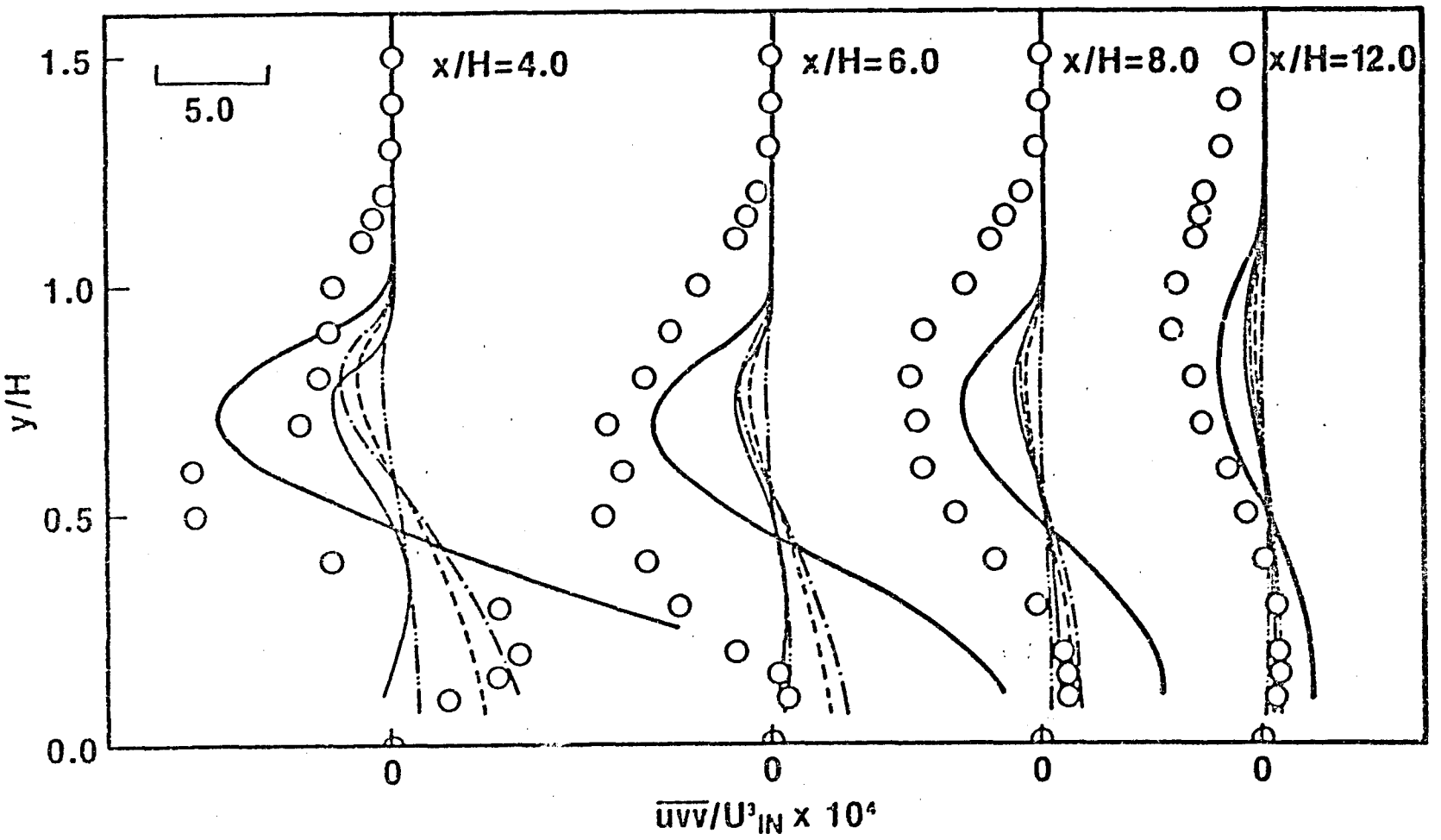

Figure 19 Triple-velocity products

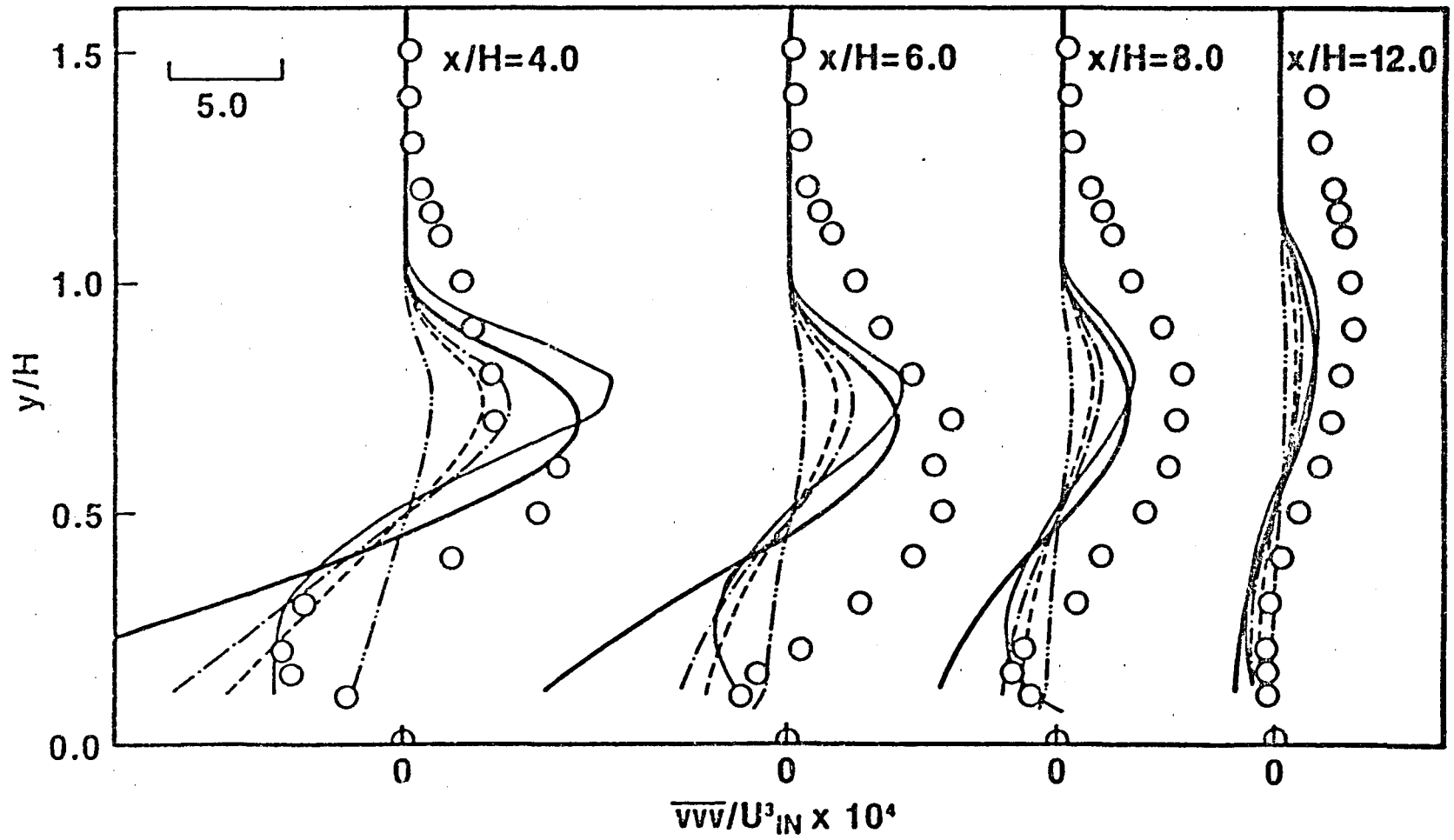

Figure 20 Triple-velocity products

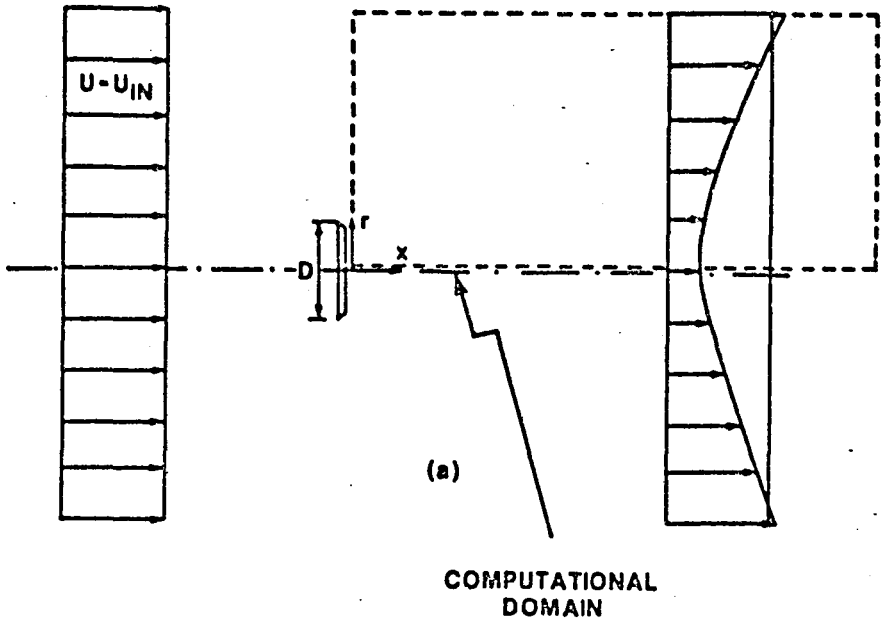

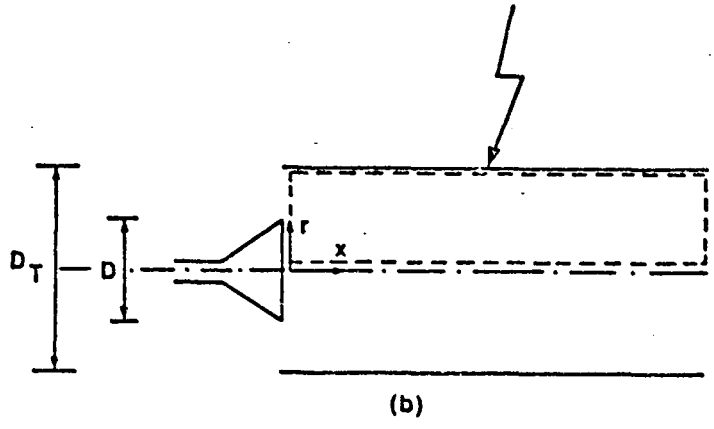

Figure 21 Flow geometries

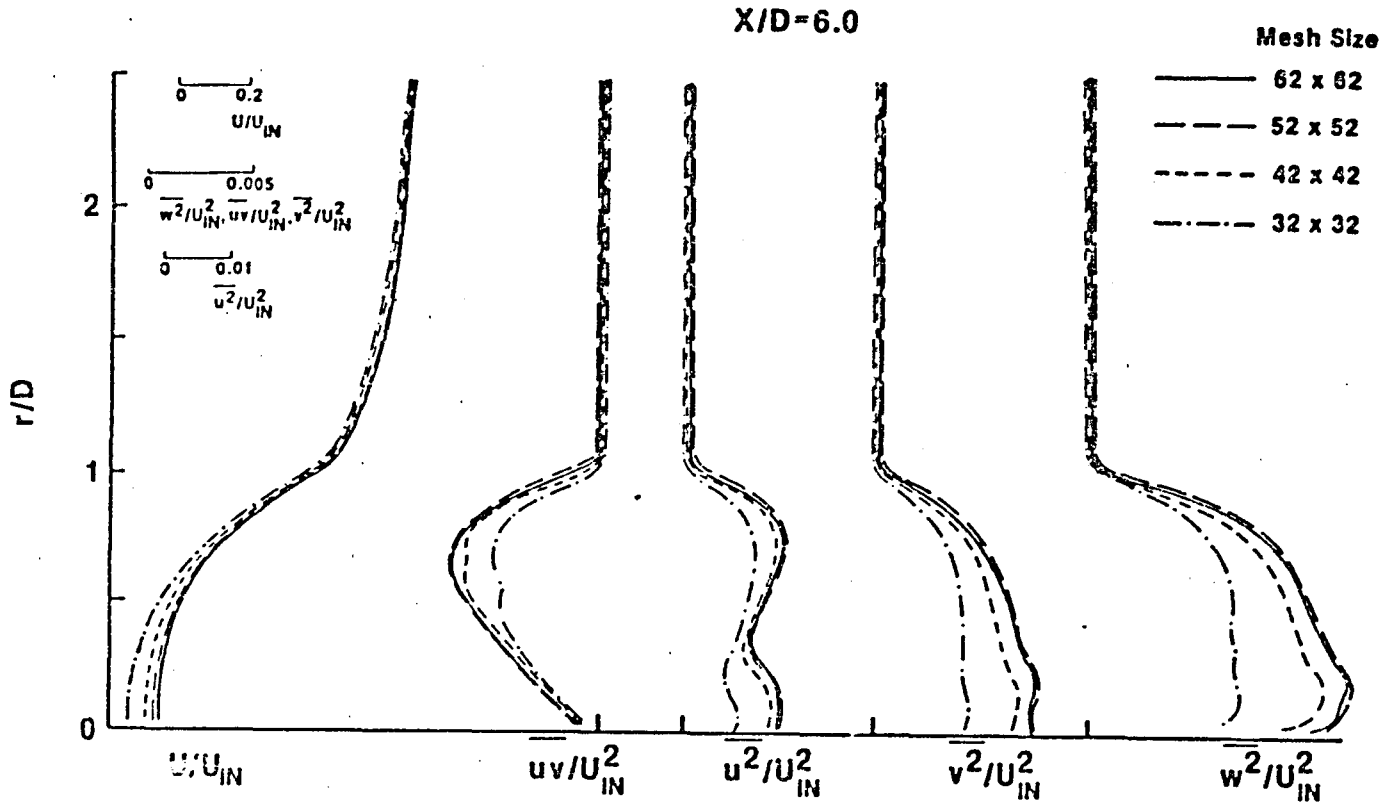

Figure 22 Grid test

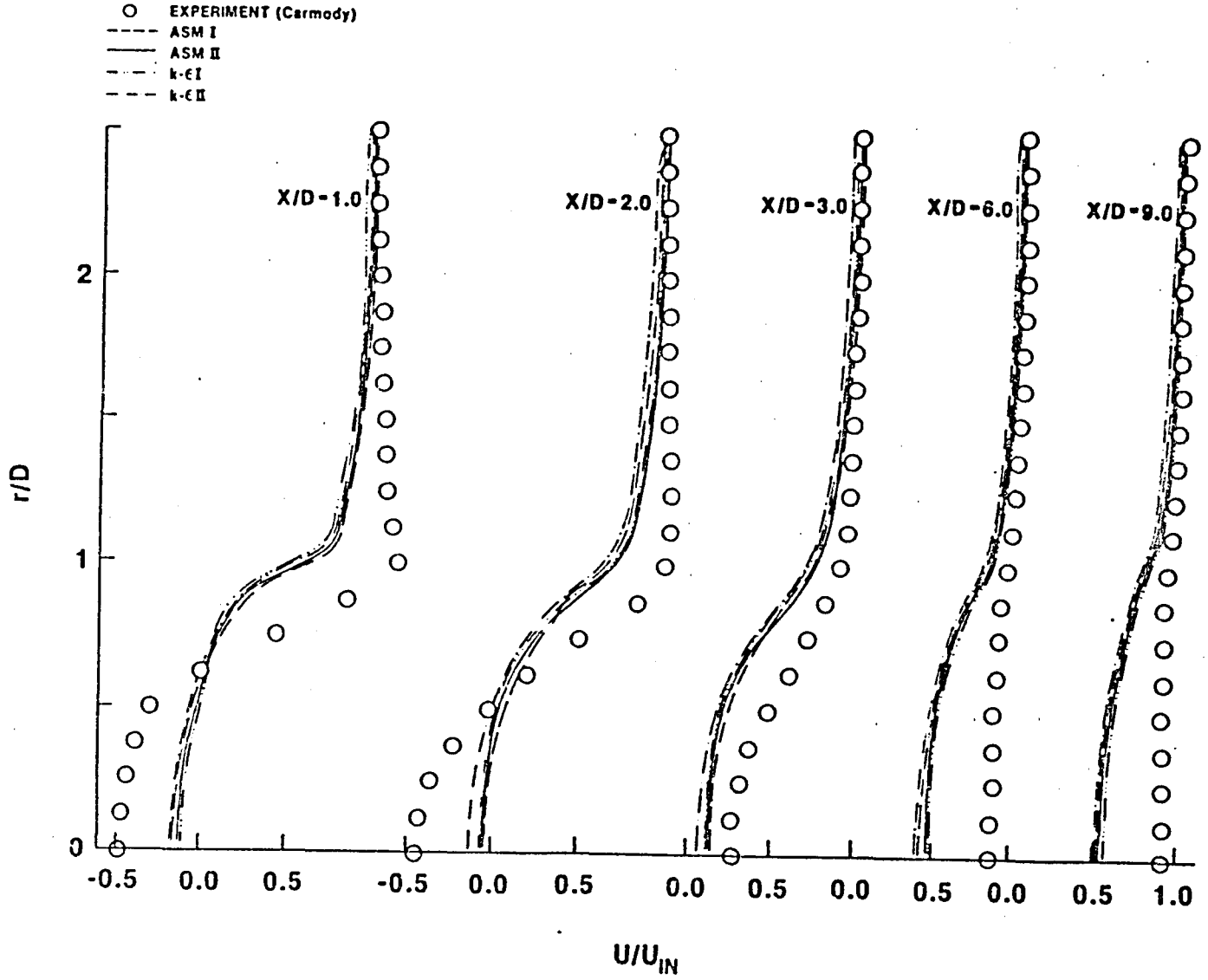

Figure 23 Mean velocity profiles in the flow passage for the external flow over a disk

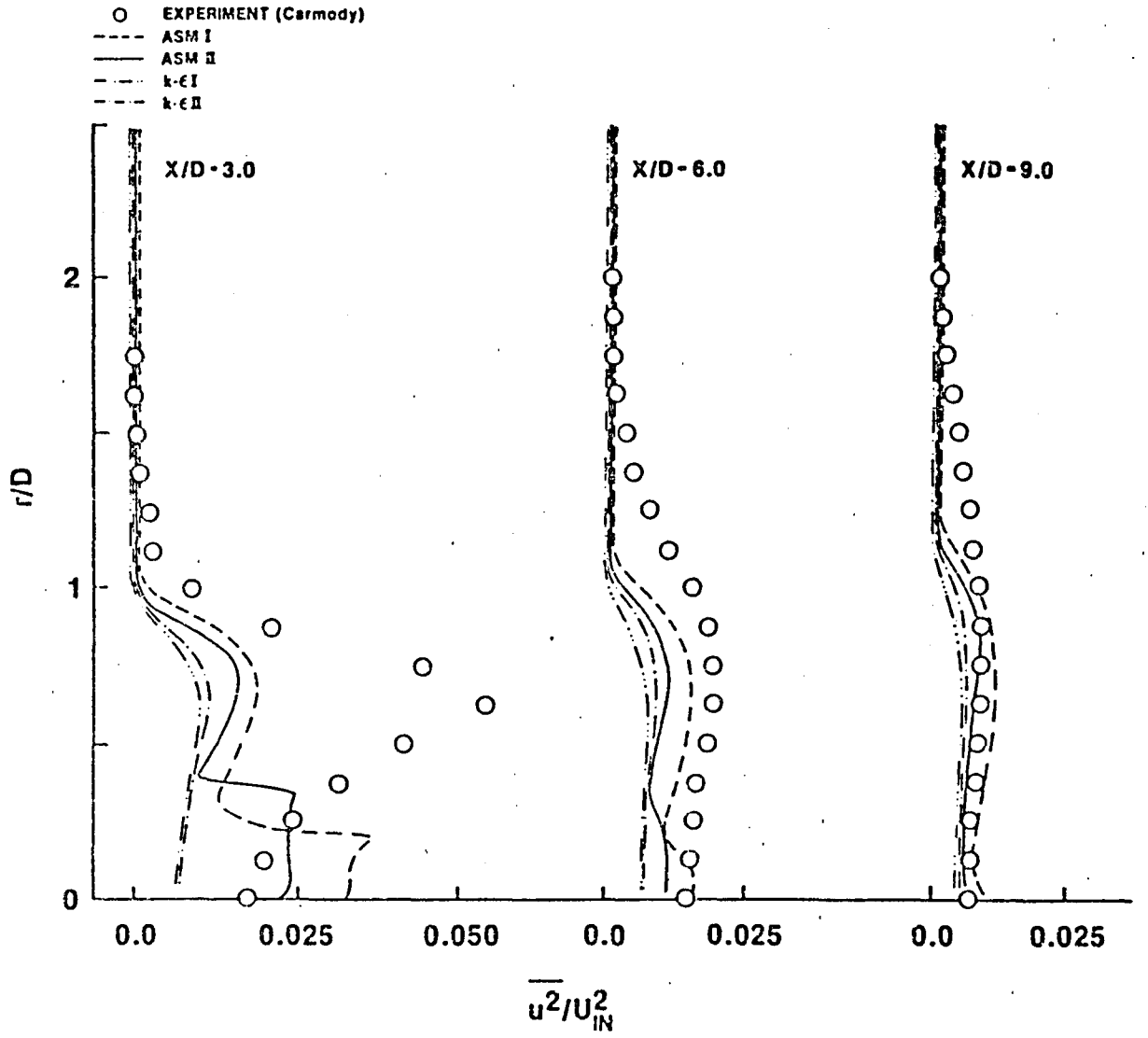

Figure 24 Streamwise component of Reynolds-stress distributions for the external flow over a disk

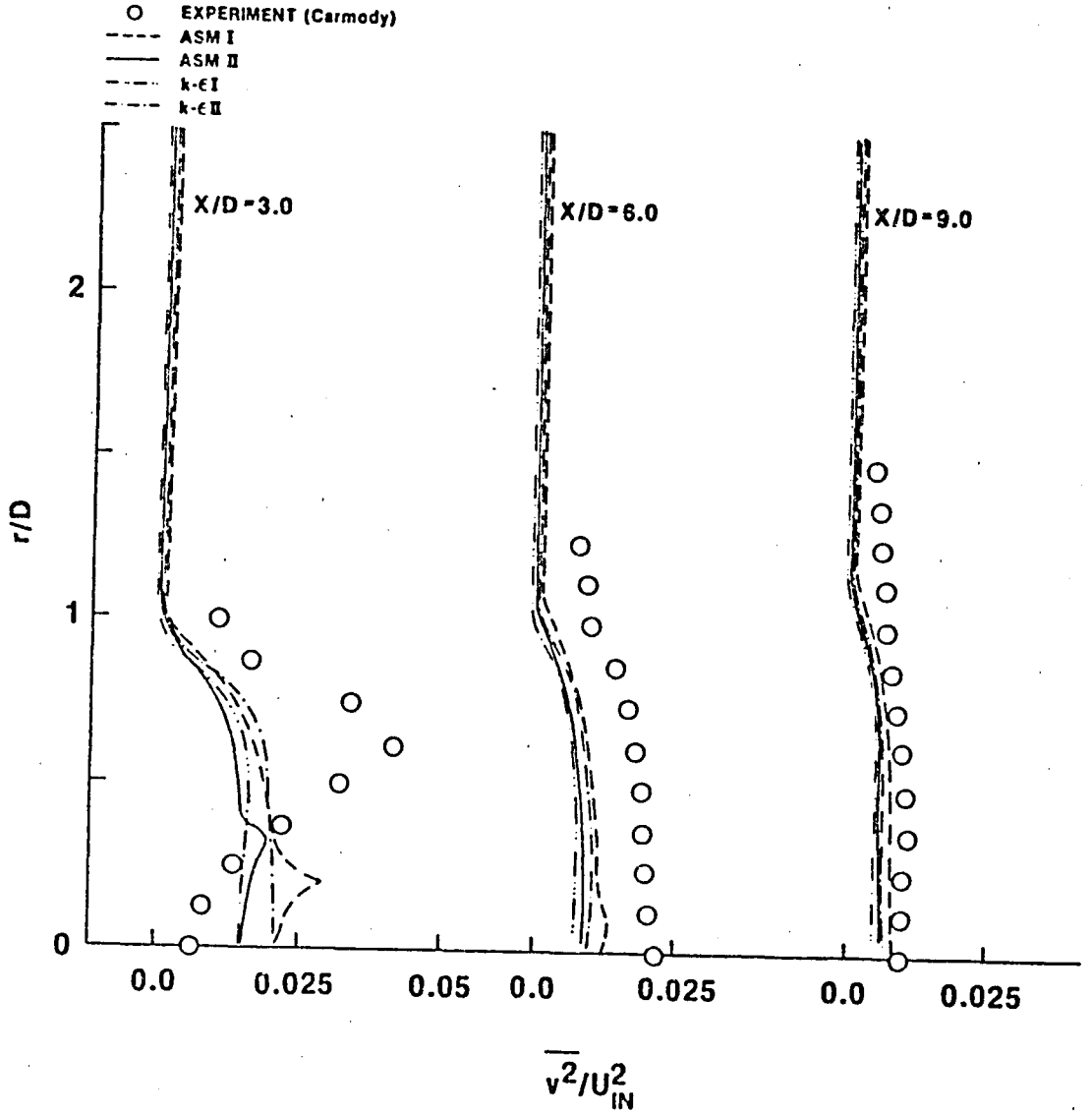

Figure 25 Radial component of Reynolds-stress distributions for the external flow over a disk

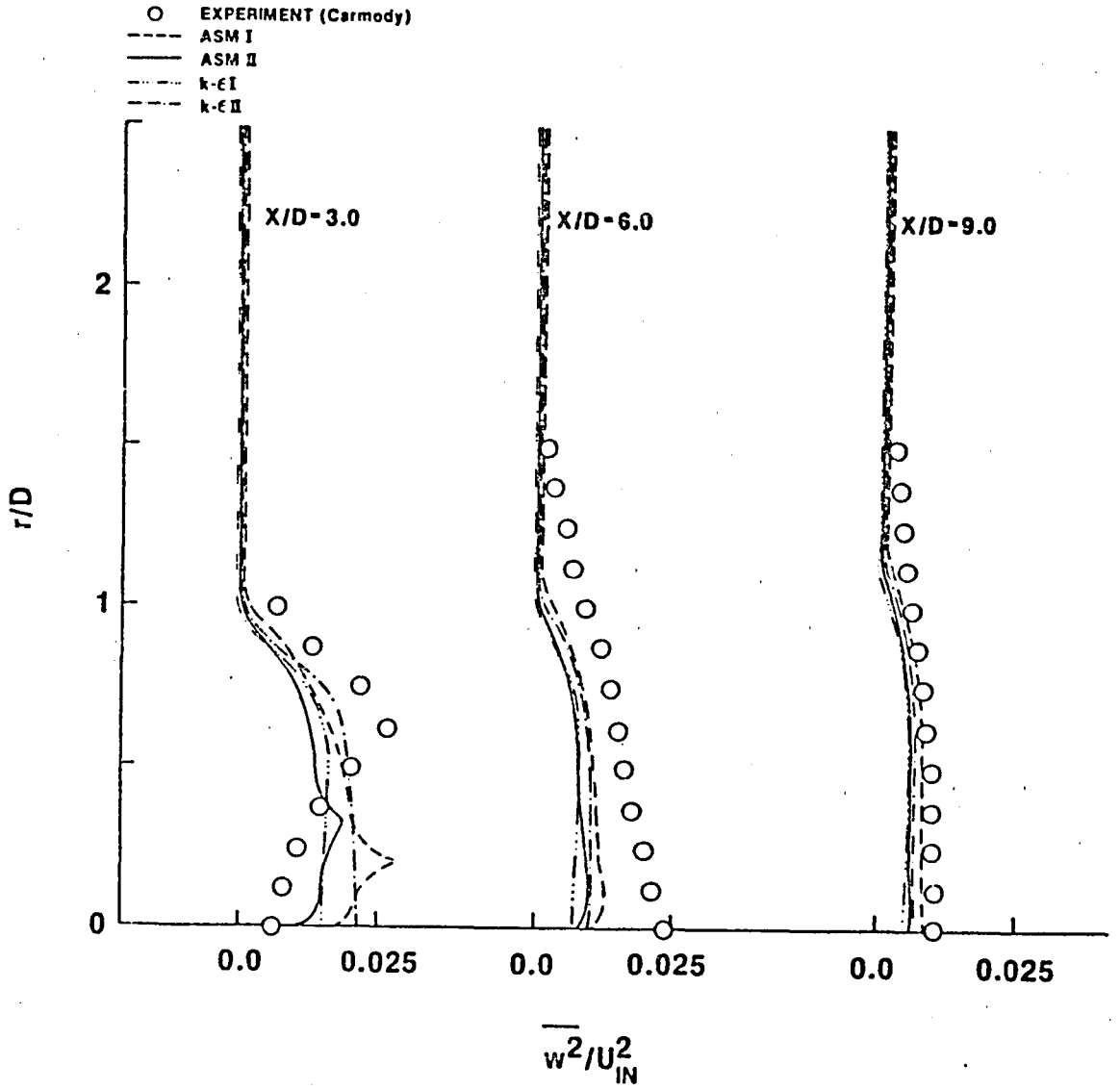

Figure 26 Azimuth component of Reynolds-stress distributions for the external flow over a disk

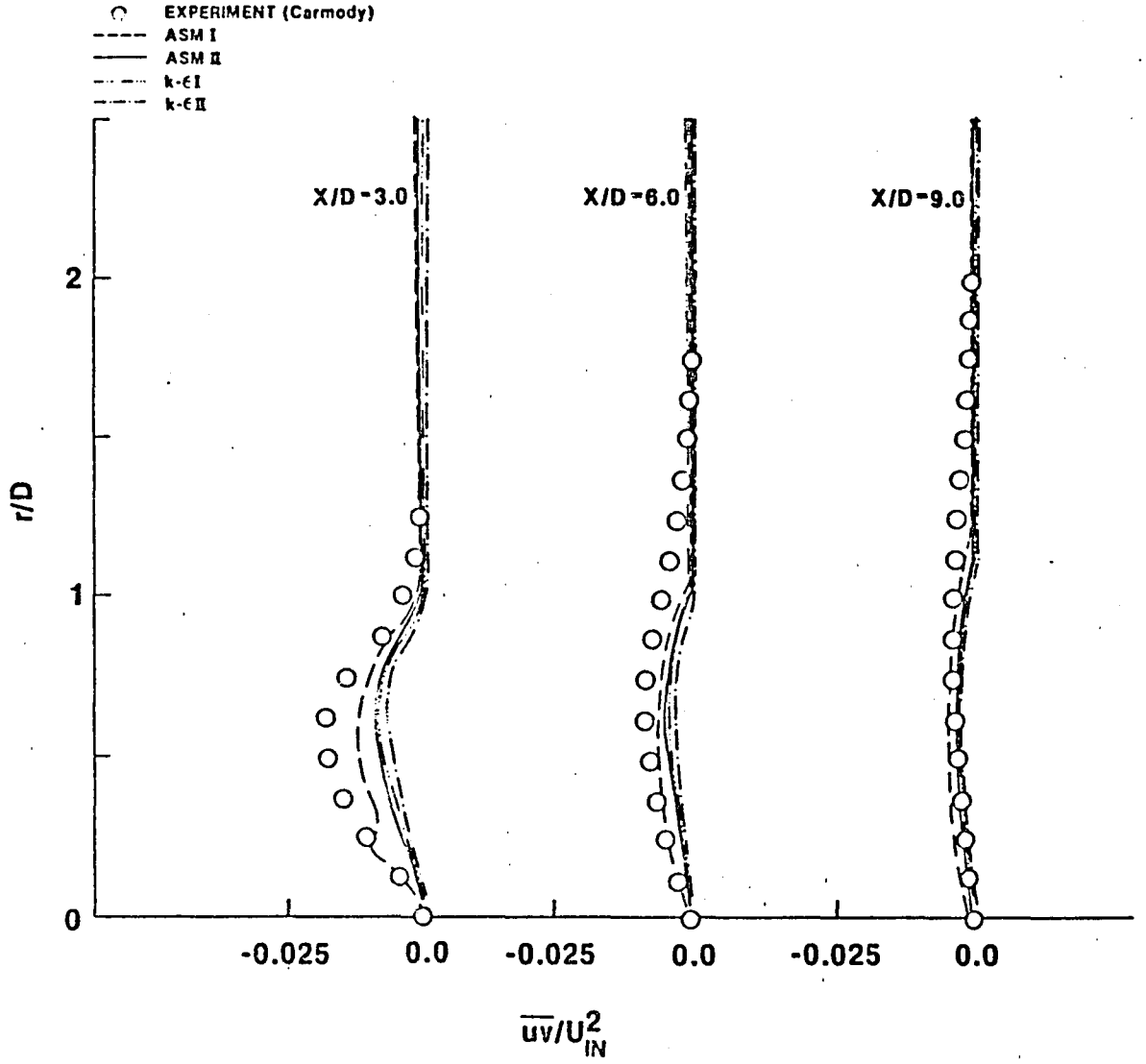

Figure 27 Shear stress distributions for the external flow over a disk

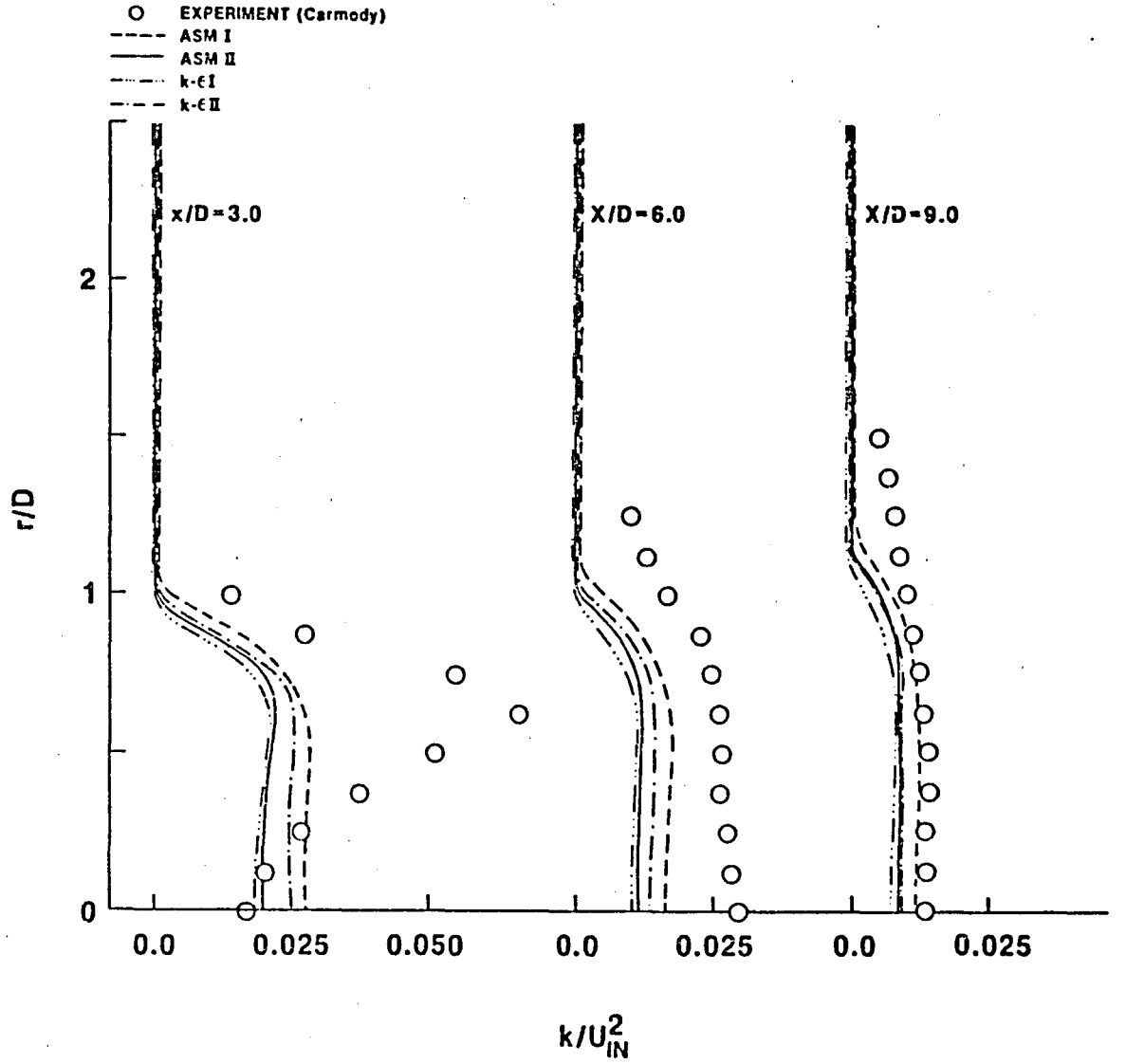

Figure 28 Turbulence kinetic energy profiles for the external flow over a disk

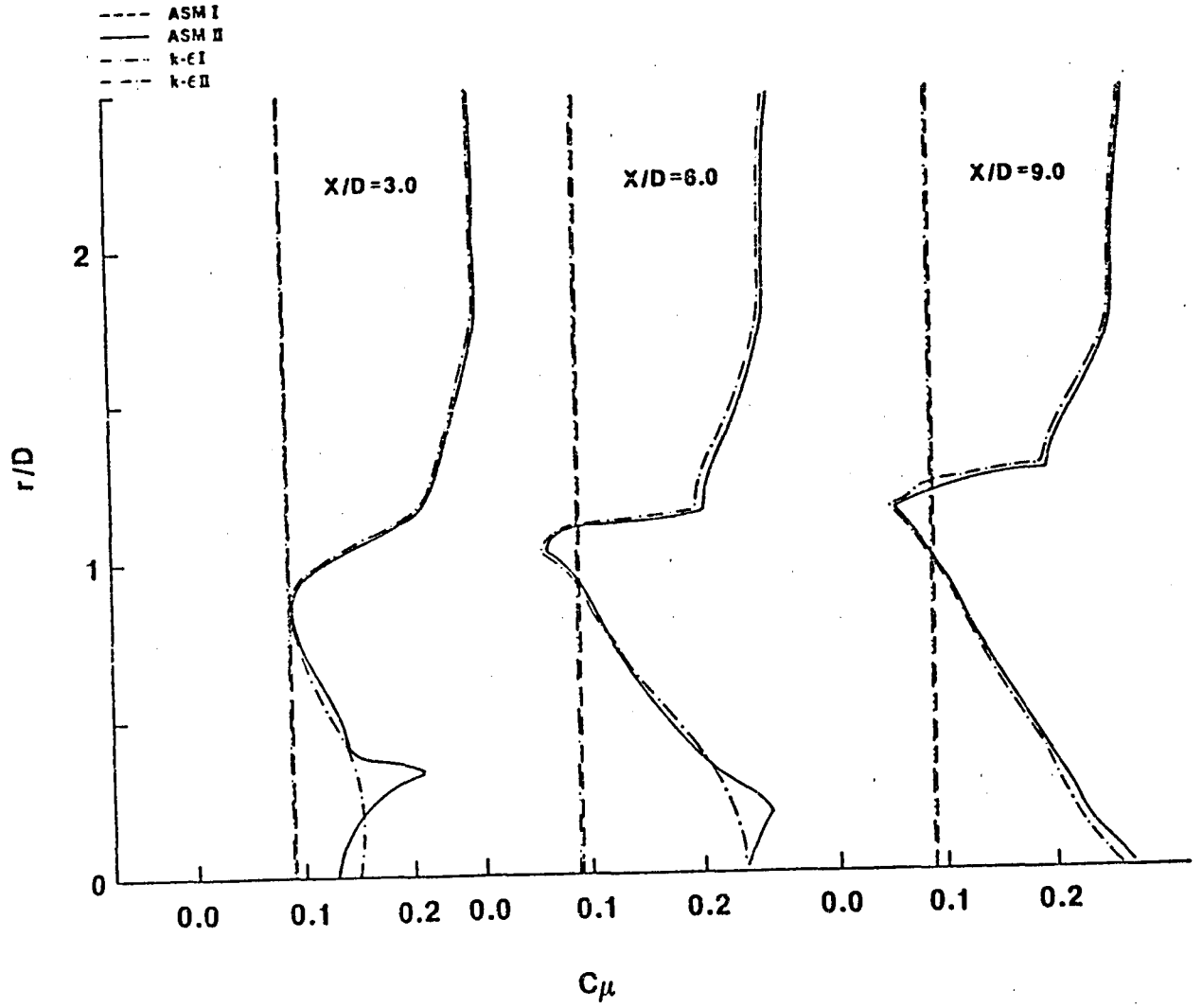

Figure 29 C_μ profiles for the external flow over a disk

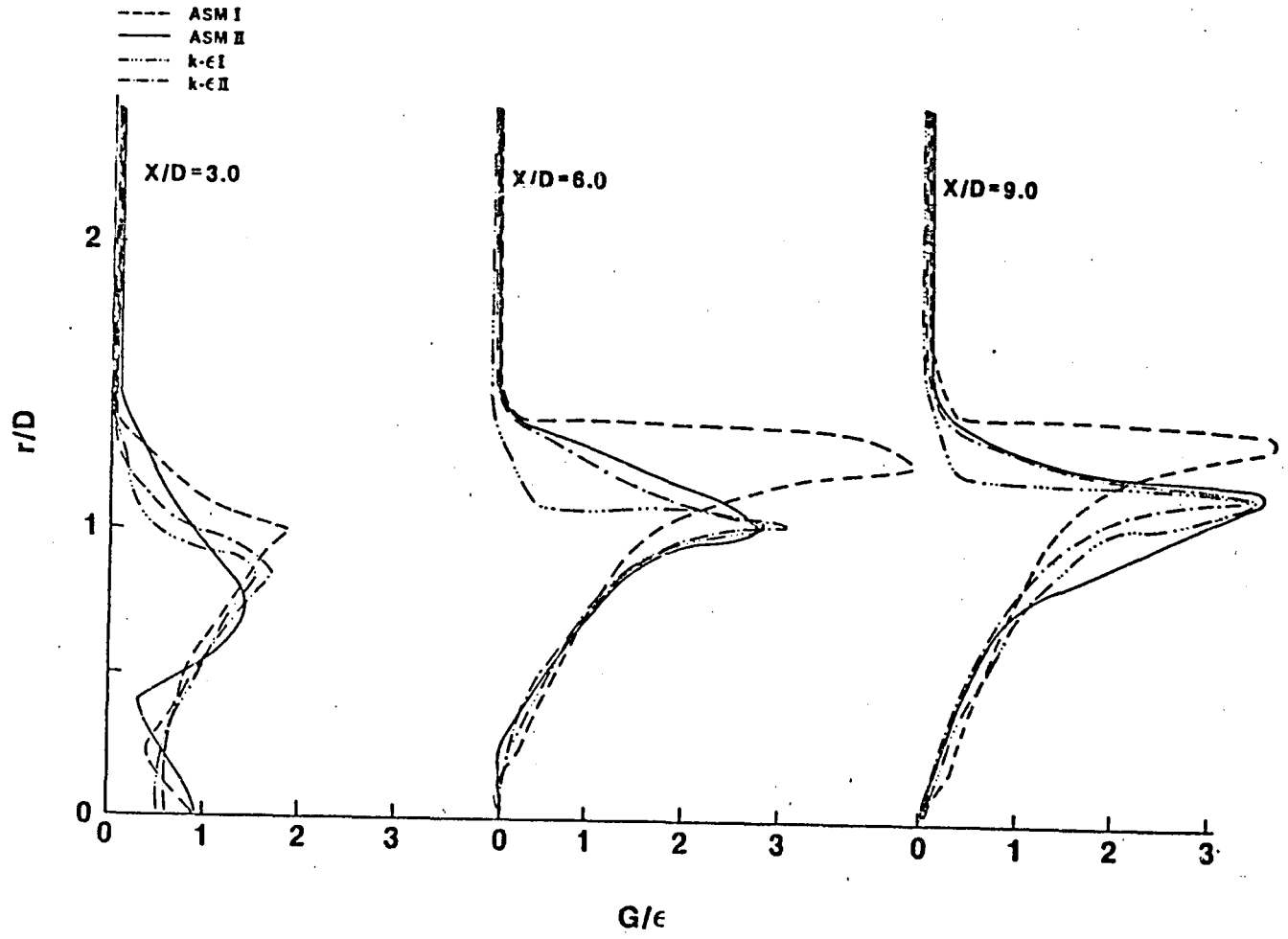

Figure 30 G/c distributions for the external flow over a disk

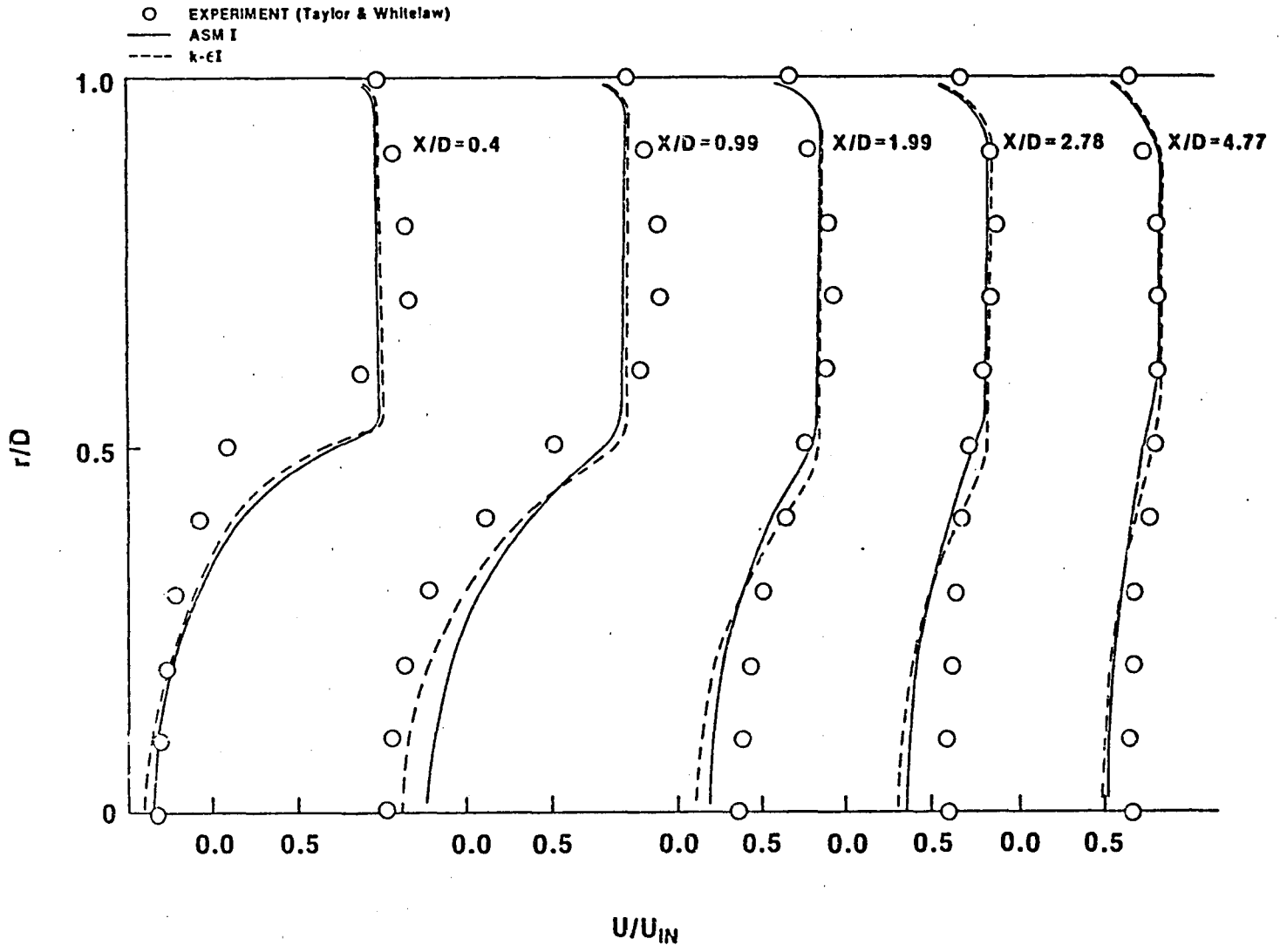

Figure 31 Velocity profiles in the flow passage for the internal flow over a cone

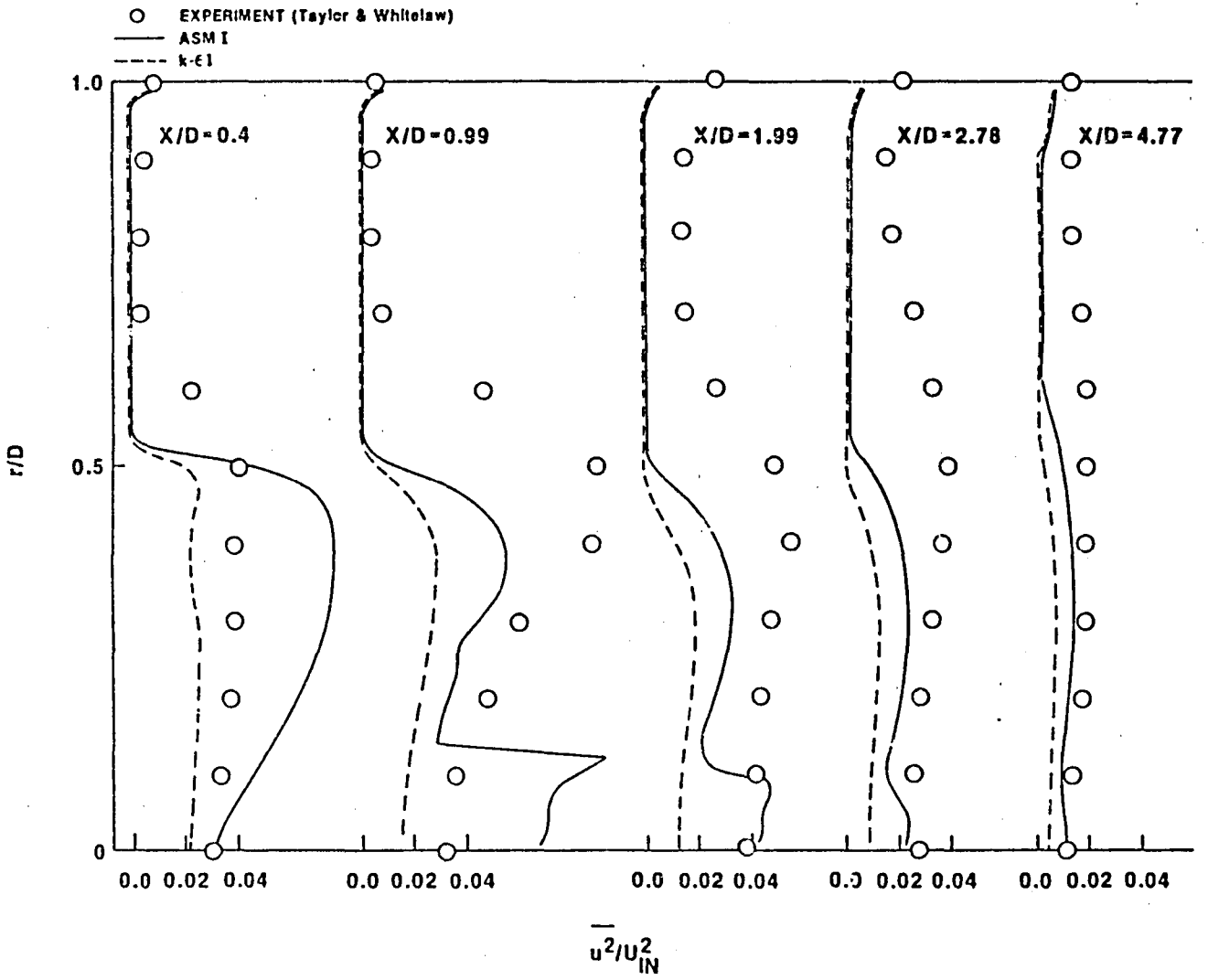

Figure 32 Streamwise component of Reynolds-stress distribution for the external flow over a cone

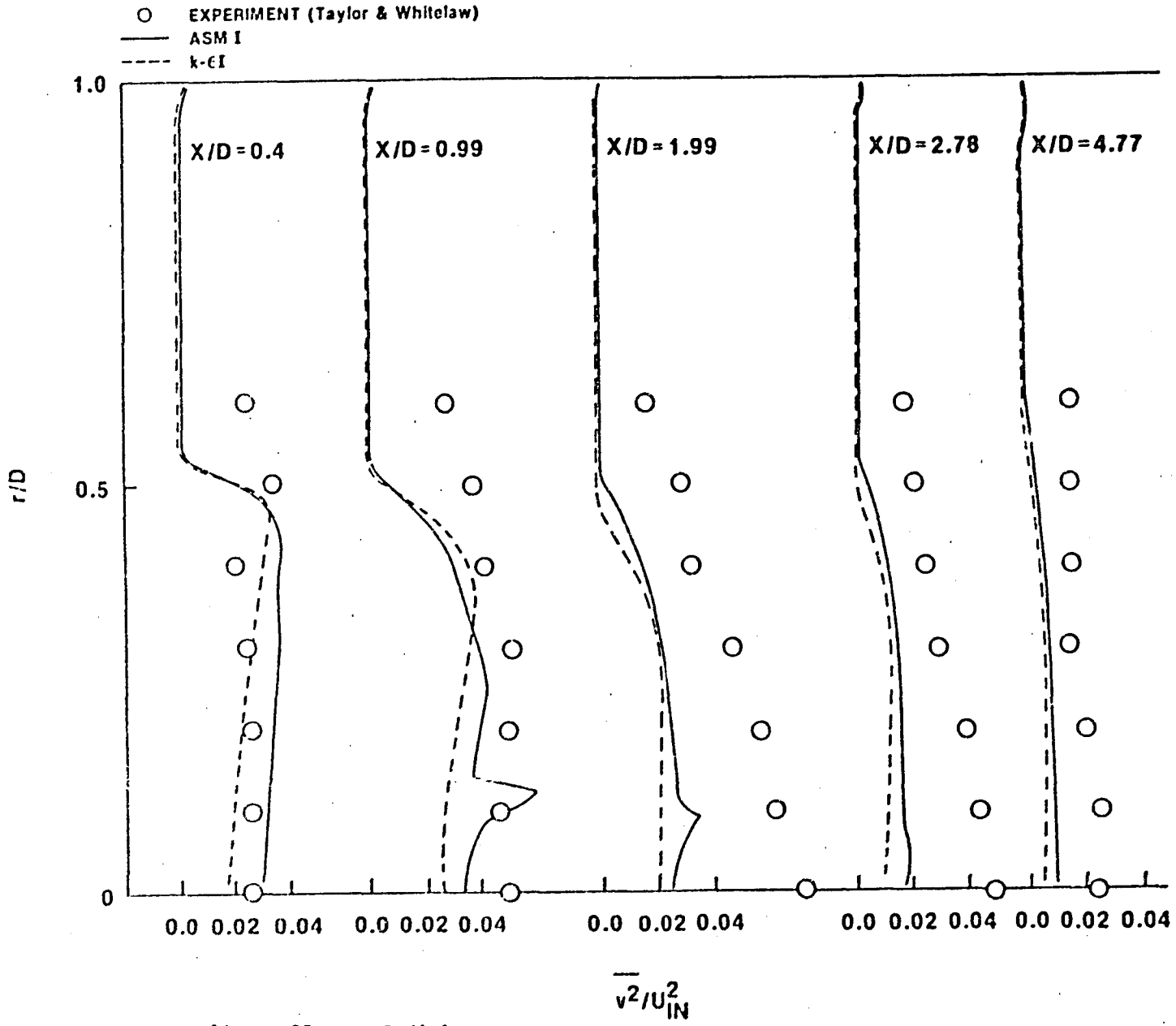

Figure 33 Radial component of Reynolds-stress distribution for the internal flow over a cone

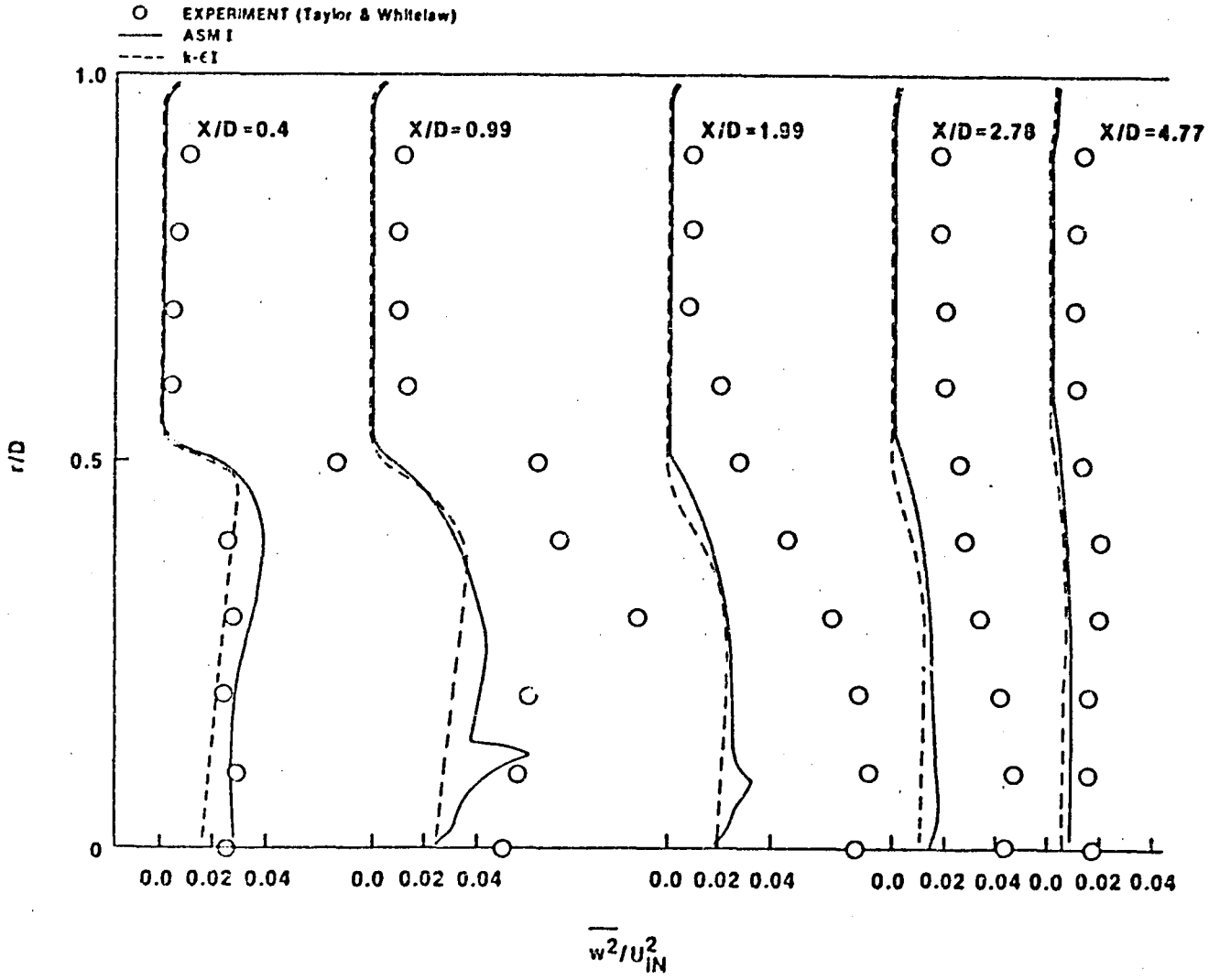

Figure 34 Azimuth component of Reynolds-stress distribution for the internal flow over a cone

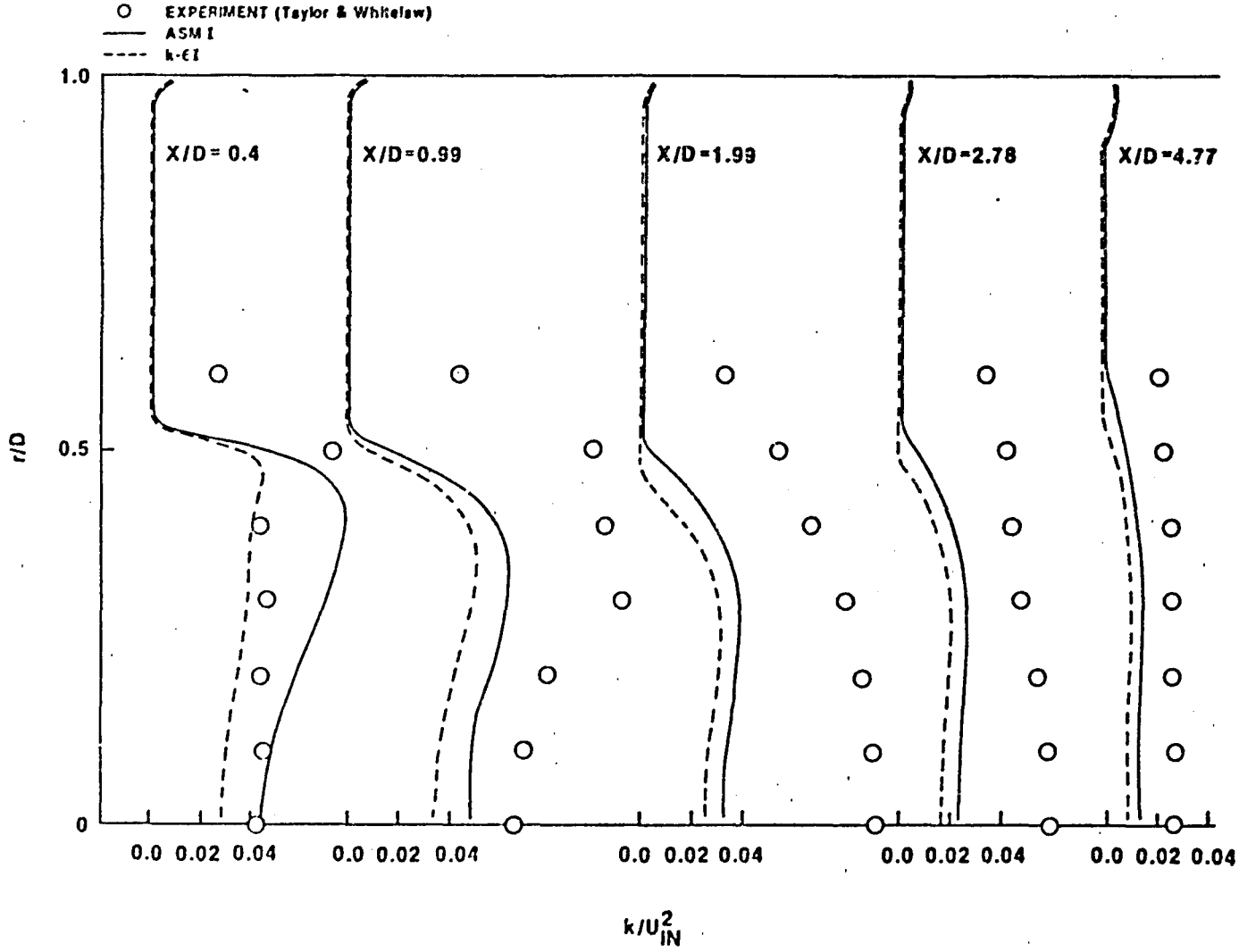

Figure 35 Turbulence kinetic energy distributions for the internal flow over a cone.

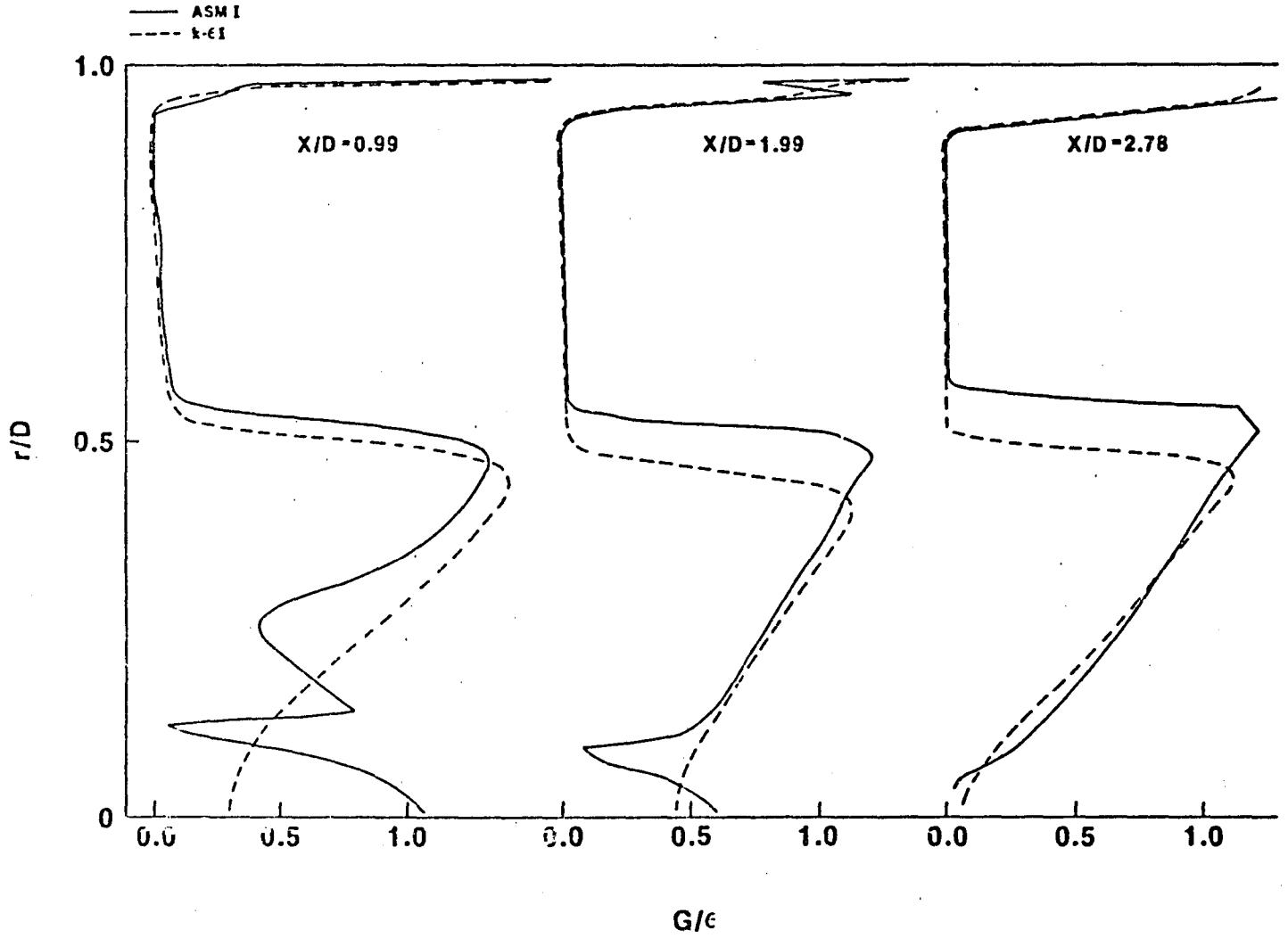

Figure 36 G/ε distributions for the internal flow over a cone

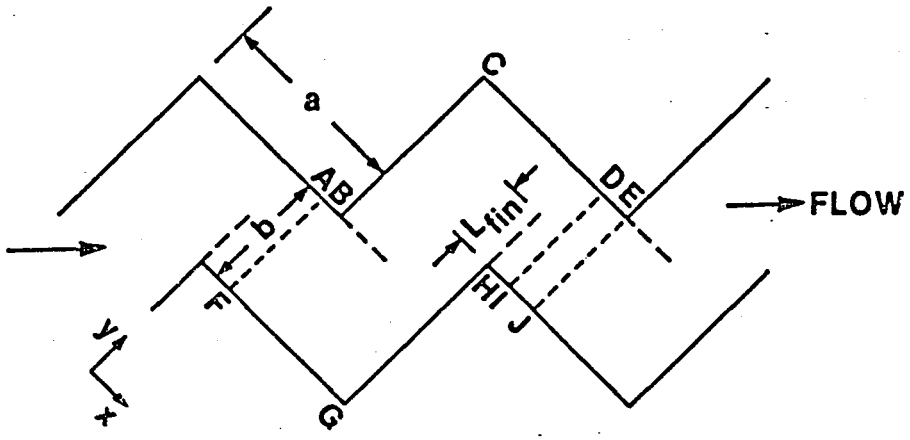

Figure 37 Corrugated wall channels

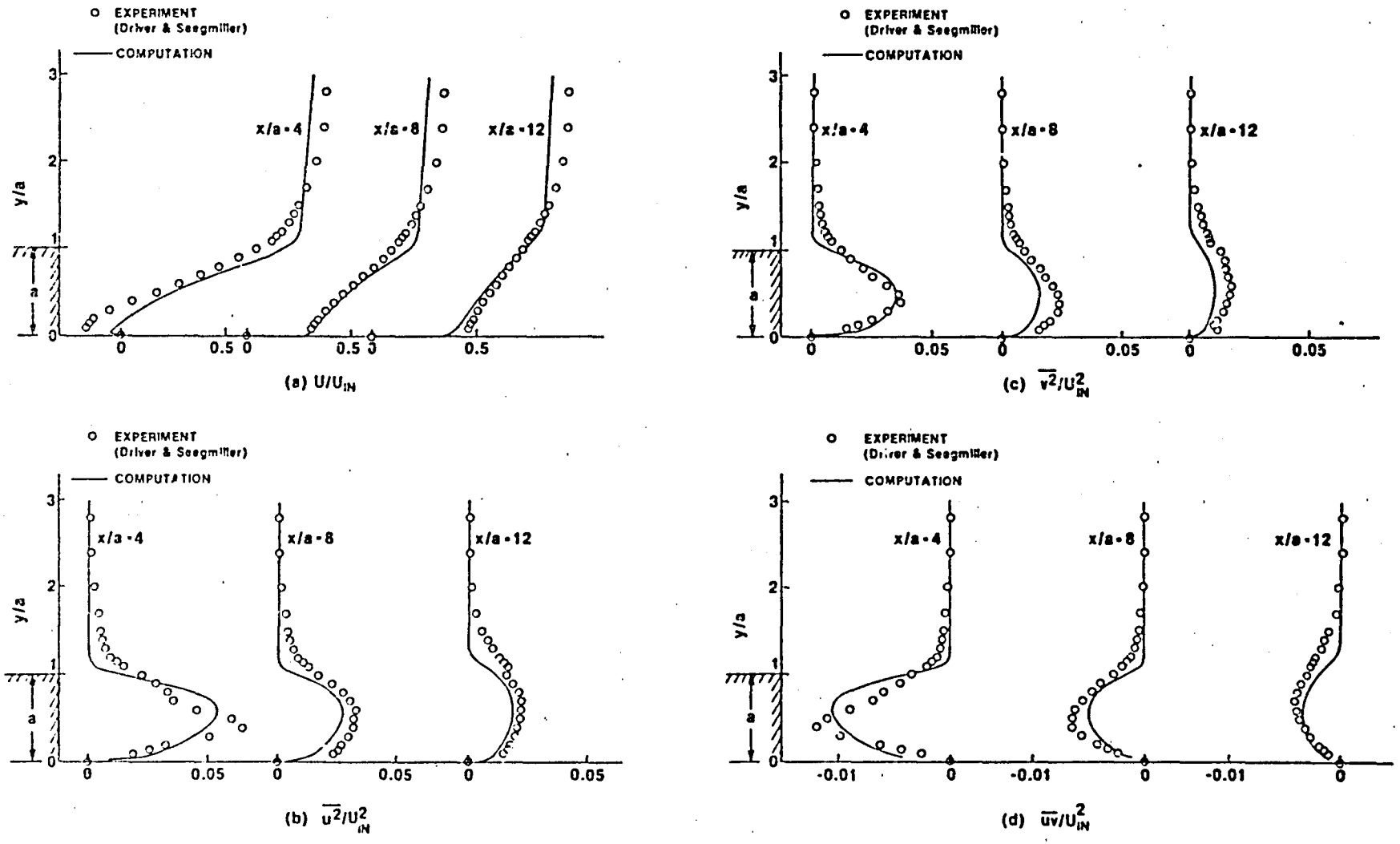

Figure 38 Velocity and the Reynolds-stress profiles in a backward facing step flow

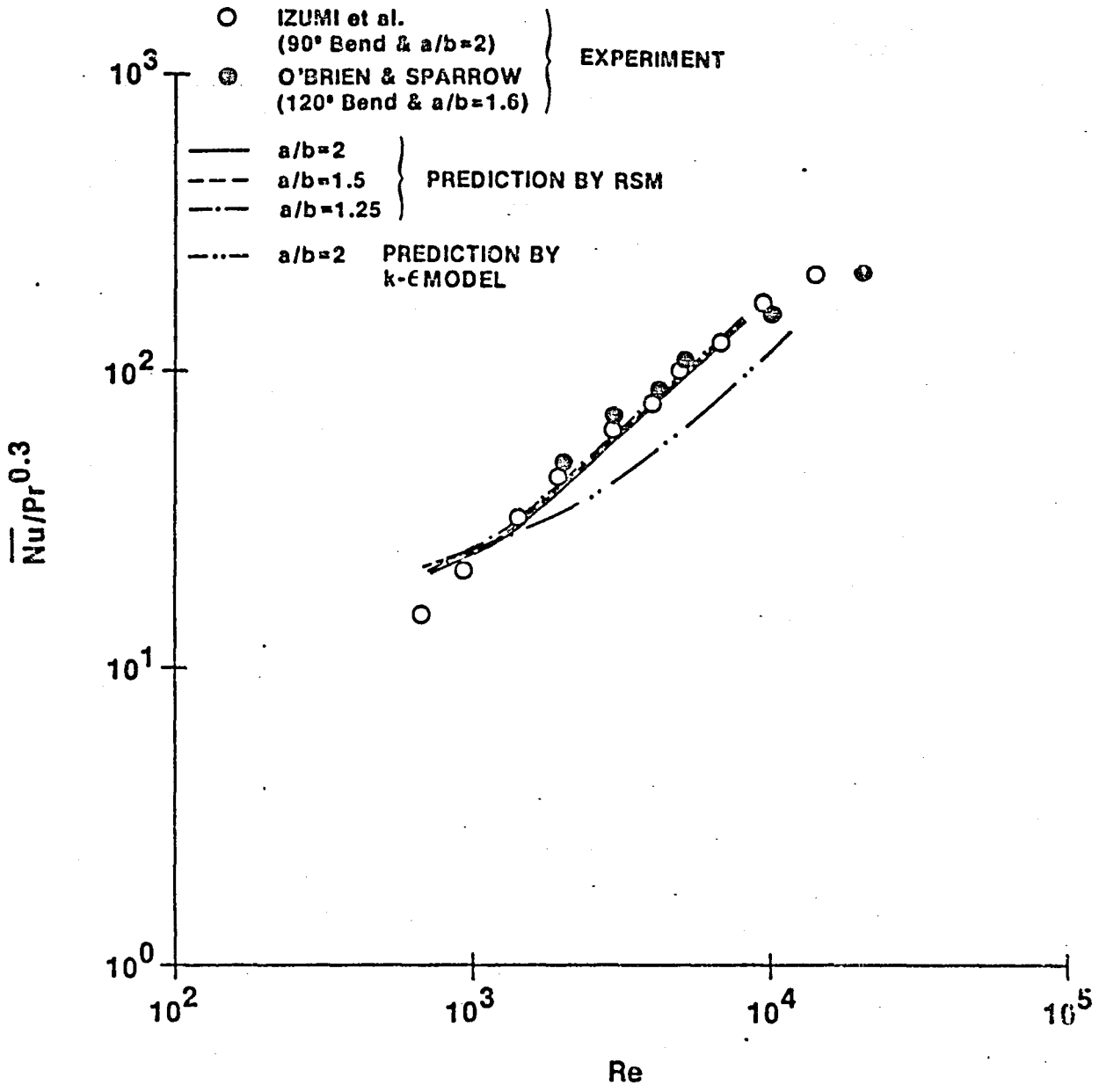

Figure 39 . Average Nusselt number as a function of Reynolds number

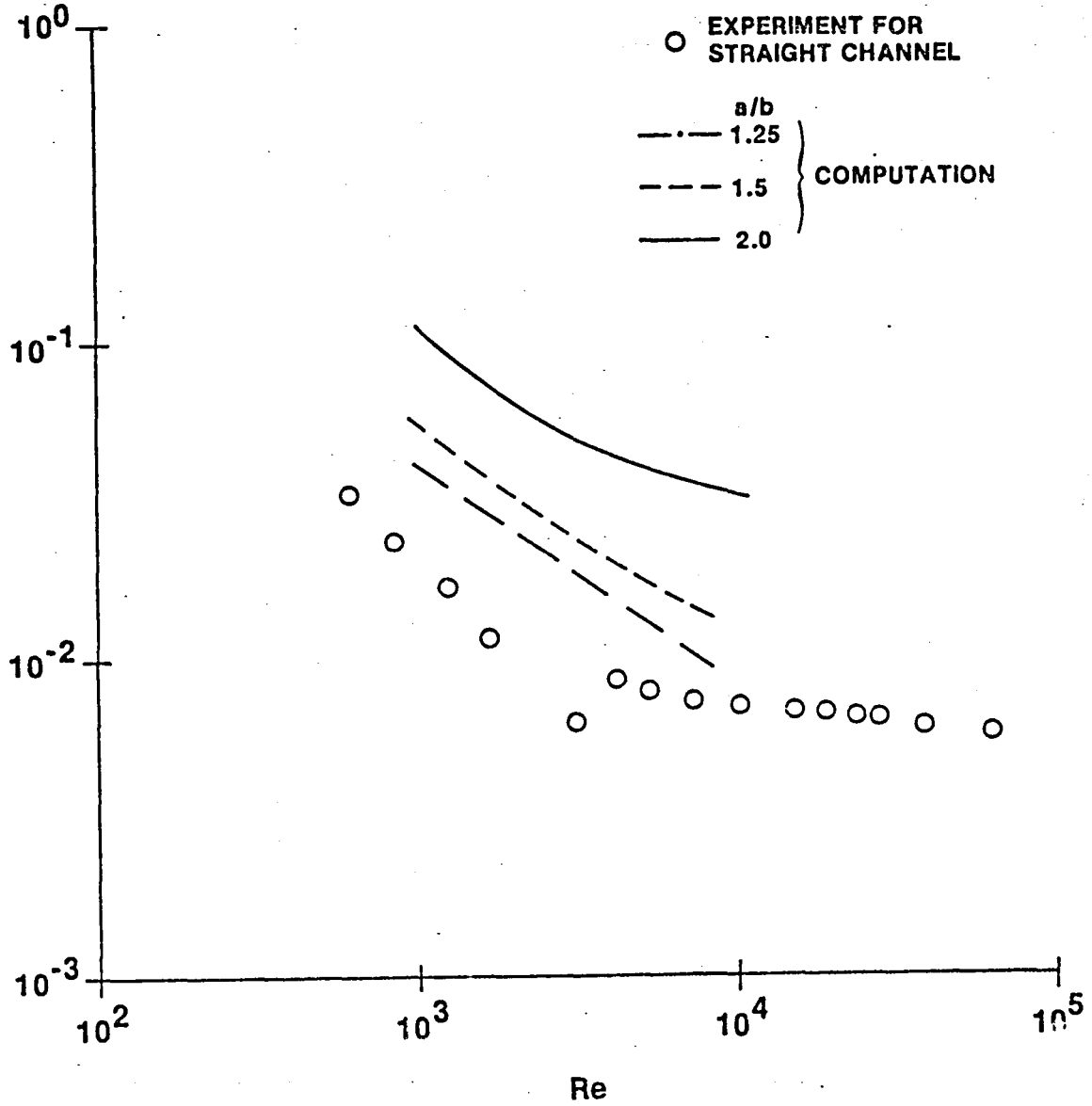

Figure 40 Average skin friction coefficient as a function of Reynolds number

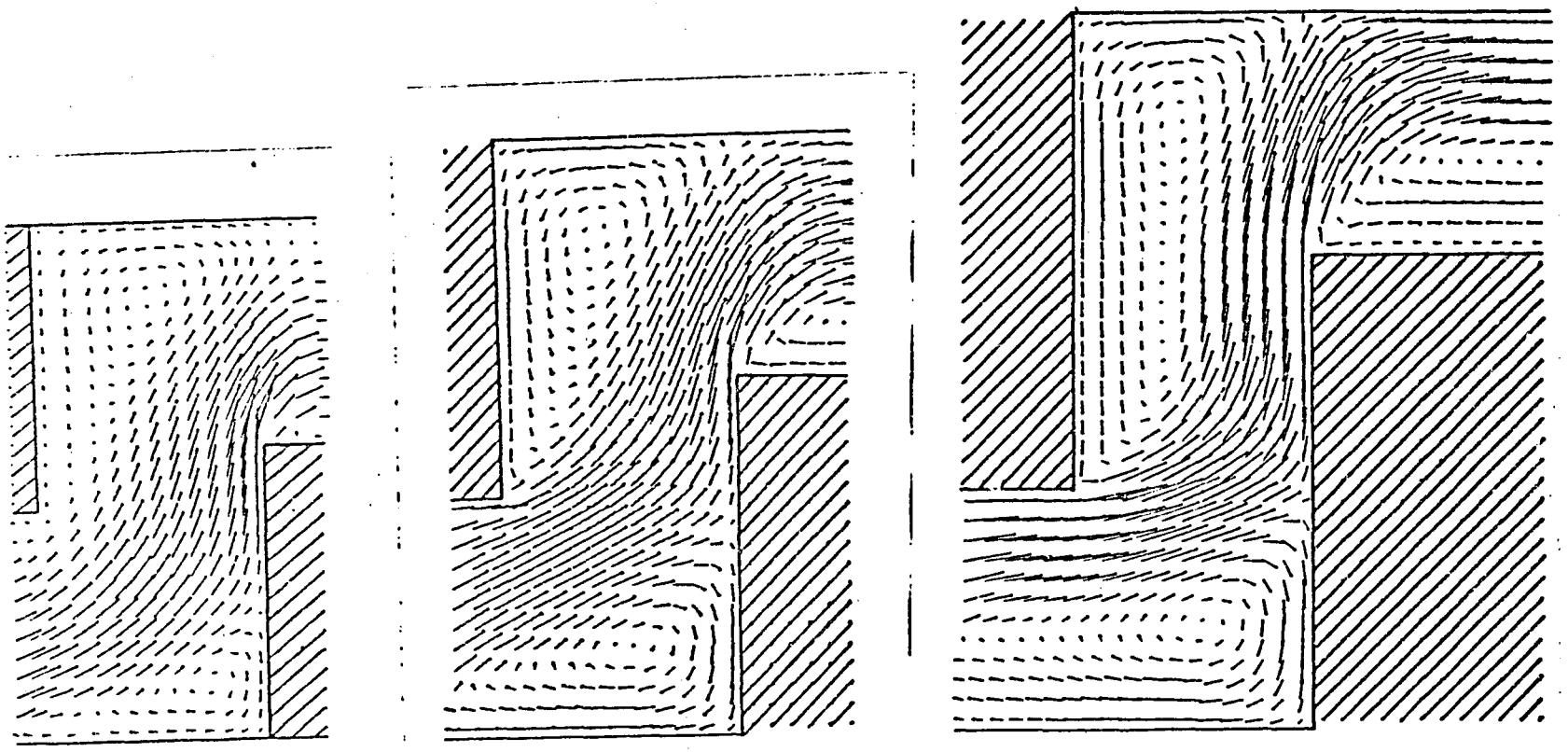

a/b = 1.25

a/b = 1.5

a/b = 2

Figure 41 Velocity vectors in channels

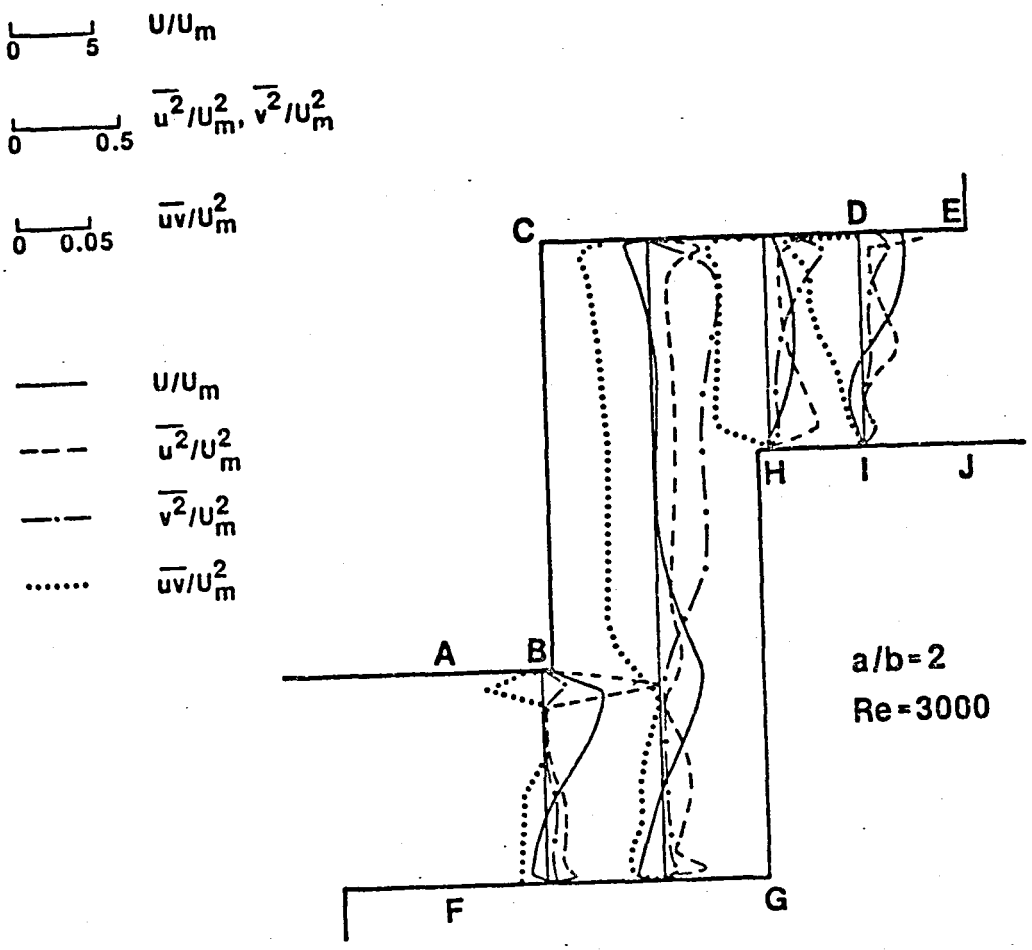

Figure 42 Velocity and the Reynolds-stress profiles in a corrugated wall channel (a/b = 2, Re = 3000)

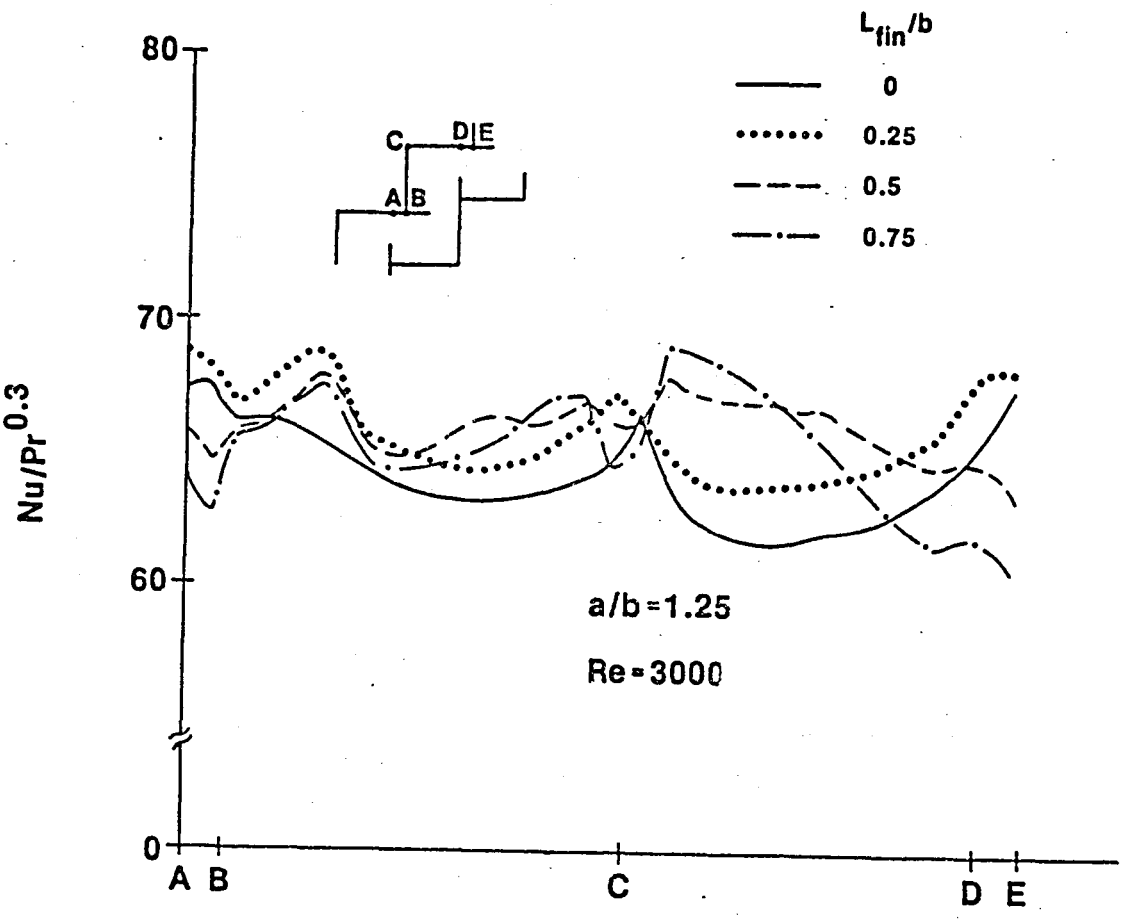

Figure 43 Local Nusselt number along the channel wall (a/b = 1.25, Re = 3000)

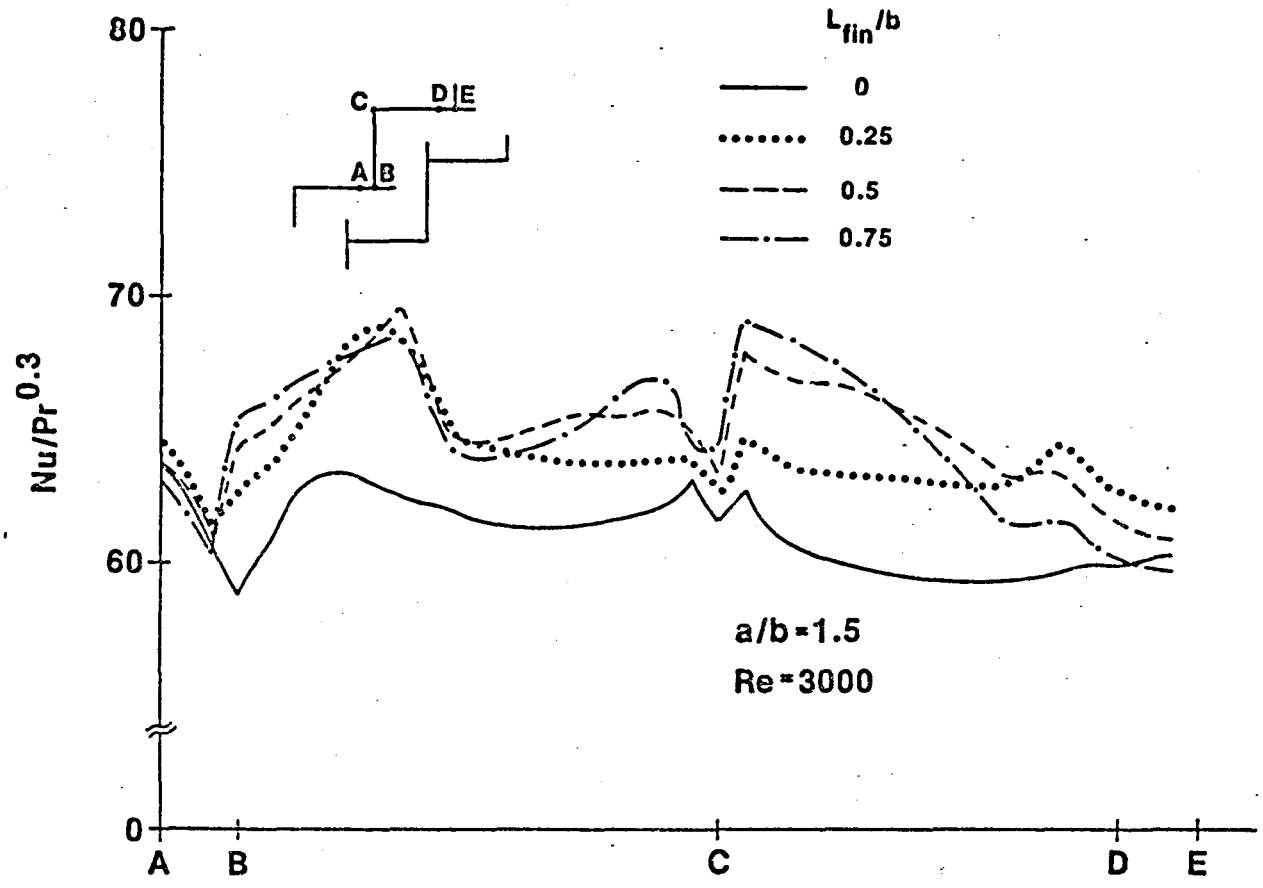

Figure 44 Local Nusselt number along the channel wall (a/b = 1.5, Re = 3000)

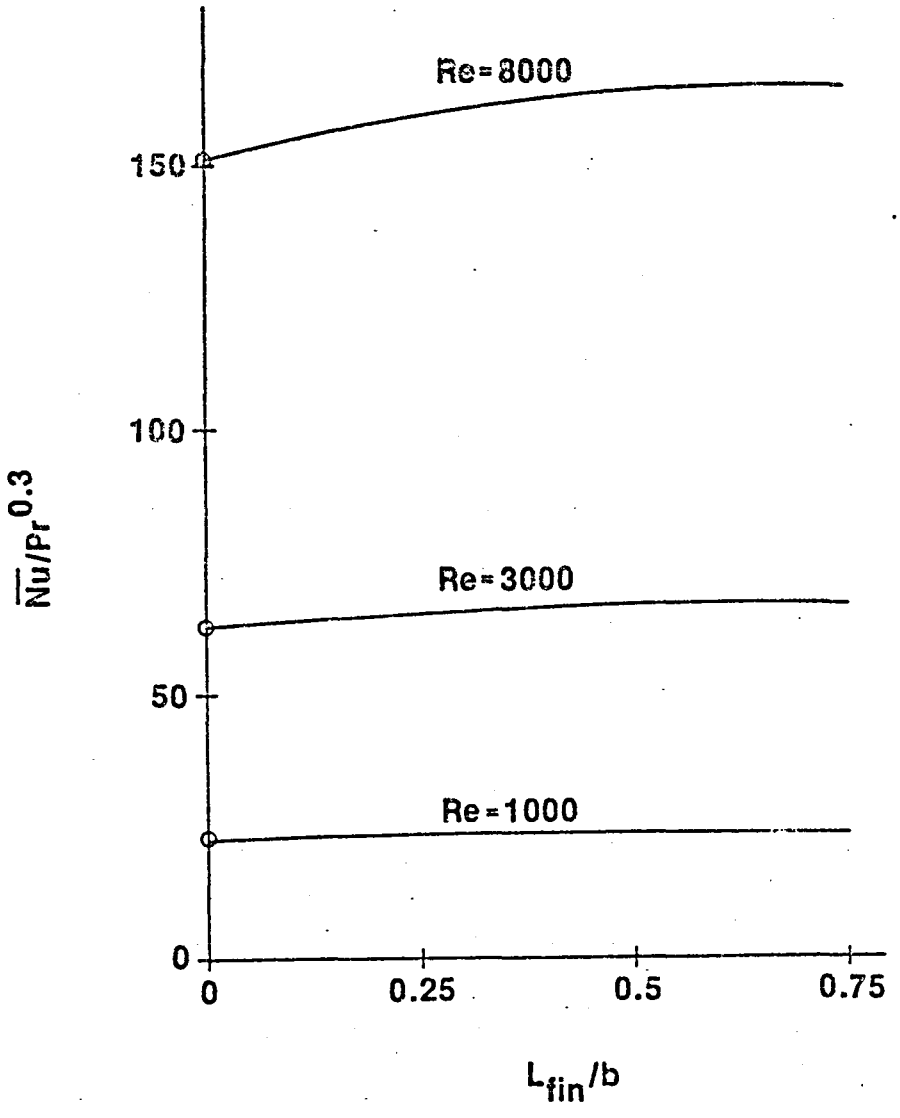

Figure 45 Average Nusselt number as a function of the length of fin

END

DATE

FILMED

MAR 13 1986

End of Document